Formation and feedback processes of massive stars in clusters

Ahmad Ali

Submitted by Ahmad Ali to the University of Exeter as a thesis for the degree of Doctor of Philosophy in Physics, June, 2018.

I certify that all material in this thesis which is not my own work has been identified and that no material has previously been submitted and approved for the award of a degree by this or any other University.

Signed: . . . . . .

Ahmad Ali

Date: . . . . . .

Abstract

Many uncertainties remain as to how the most massive stars are formed and how they interact with their environment via radiative and mechanical processes. This feedback may affect future generations of star formation – triggering it by compressing gas, or hindering it by dispersing reservoirs. These scenarios can be simulated by solving the equations of hydrodynamics and radiative transfer. However, the latter is usually simplified due to its computational expense, despite its importance in determining the dynamics.

In this thesis, I describe how I increased the efficiency of the radiation hydrodynamics code, TORUS, which uses a Monte Carlo approach to solving the radiative transfer. Tens of millions of energy packets are propagated through a domain split over hundreds of processors running in parallel with Message Passing Interface (MPI). By re-examining and improving communication algorithms, I lowered the radiation run time by about a factor of ten, making it tractable to run three-dimensional simulations of massive star feedback in clusters. This includes both the stellar and diffuse radiation fields, with multiple atomic species and silicate dust grains. The full ionization states and temperatures can then be fed in to produce self-consistent synthetic observations.

I applied this to clouds of 10^3 and $10^4\,\mathrm{M}_\odot$ with surface density $0.01\,\mathrm{g\,cm^{-2}}$, containing a $34\,\mathrm{M}_\odot$ star, with photoionization and radiation pressure feedback. Photoionization is efficient at shaping and dispersing clouds. The expanding ionization front forms dense, spherical knots with pillars pointing away from the emitting star. These resemble the Pillars of Creation in the Eagle Nebula, and the proplyds observed in the Orion Nebula. In the lower-mass model, almost all material is removed from the $(15.5\,\mathrm{pc})^3$ grid within 1.6 Myr; the higher mass cloud is somewhat more resistant, with 25 per cent remaining inside $(32.3\,\mathrm{pc})^3$ after 4.3 Myr. Radiation pressure has a negligible effect, but will be more important for denser clouds or higher luminosities.

Contents

List of Figures 7

List of Tables 9

1 Introduction 12

1.1 Star and cluster formation . . . 13

1.1.1 Giant molecular clouds . . . 13

1.1.2 Collapse and accretion scenarios . . . 14

1.1.3 Initial mass function . . . 17

1.2 Massive star feedback . . . 18

1.2.1 Computational radiation hydrodynamics . . . 19

1.2.2 Protostellar heating . . . 21

1.2.3 Photoionization . . . 22

1.2.4 Stellar winds . . . 25

1.2.5 Radiation pressure . . . 27

1.2.6 Far-ultraviolet radiation . . . 28

1.2.7 Supernovae . . . 29

1.3 Aims of this thesis . . . 30

2 Radiation hydrodynamics 31

2.1 Definitions for radiation . . . 31

2.2 Radiative transfer . . . 33

2.3 Emission and absorption by gas . . . 35

2.3.1 Heating and cooling processes 36
2.3.2 Photoionization 36
2.3.3 Recombination 37
2.3.4 Free-free continuum 38
2.3.5 Collisionally excited forbidden lines 39
2.4 Dust processes 41
2.5 Radiation force 42
2.6 Hydrodynamics 43

3 Numerical methods: RHD in TORUS 44
3.1 Numerical hydrodynamics 44
3.1.1 Fluxes 46
3.1.2 Artificial viscosity 47
3.1.3 Higher dimensions 48
3.1.4 Summary 48
3.2 Monte Carlo radiative transfer 49
3.2.1 Gas photoionization and thermal balance 53
3.2.2 Dust thermal balance 53
3.2.3 Radiation pressure 54
3.2.4 FUV interstellar radiation field 55
3.3 Parallelisation 56
3.3.1 Context 56
3.3.2 Message Passing Interface 57
3.3.3 Domain decomposition 58
3.3.4 MCRT load-balancing 59
3.3.5 Parallelisation of photon propagation 60
3.3.6 Random source selection 61
3.3.7 Flushing mode 62

3.3.8 Storing stacks of photons . . . 63
3.3.9 Idling threads . . . 64
3.3.10 End results . . . 64
3.4 Comparison with other codes . . . 65

4 Feedback in a 1000 solar mass cloud **70**
4.1 Abstract . . . 70
4.2 Introduction . . . 71
4.3 Numerical methods . . . 74
4.3.1 MC estimator smoothing . . . 75
4.3.2 Stars . . . 76
4.4 Initial conditions . . . 76
4.5 Results . . . 78
4.5.1 Bulk grid properties . . . 83
4.5.2 Morphology . . . 86
4.5.3 Electron temperature and density . . . 89
4.5.4 FUV interstellar radiation field . . . 90
4.6 Discussion of the RHD model . . . 95
4.6.1 Dynamics . . . 95
4.6.2 Temperature . . . 97
4.6.3 FUV interstellar radiation field . . . 98
4.7 Synthetic observations . . . 99
4.7.1 Recombination and forbidden lines . . . 99
4.7.2 Free–free radio observations and Lyman flux . . . 103
4.7.3 Dust emission . . . 106
4.8 Summary and conclusions . . . 109

5 Feedback in a 10,000 solar mass cloud **111**
5.1 Abstract . . . 111

5.2 Introduction . . . 112
5.3 Initial conditions . . . 113
5.4 Results and discussion . . . 113
5.4.1 Bulk grid properties . . . 116
5.4.2 Dispersal . . . 117
5.4.3 Temperature and electron density . . . 122
5.4.4 FUV interstellar radiation field . . . 122
5.4.5 Implications . . . 129
5.5 Summary and conclusions . . . 129

6 Conclusions **132**
6.1 Summary and main findings . . . 132
6.2 Proposed future work . . . 134
6.2.1 Cloud parameter space and sink particles . . . 134
6.2.2 Modelling stellar winds and supernovae . . . 136
6.2.3 Photodissociation of molecules . . . 136
6.2.4 Disk photoevaporation . . . 137

Bibliography **138**

List of Figures

1.1 Mass–luminosity relation for main sequence stars 19

3.1 Flowchart of a radiation hydrodynamics loop 49

3.2 Load-balancing illustration 59

4.1 Positions of stars at the onset of feedback (10^3 $M_\odot$ cloud) 79

4.2 Dust opacity per unit mass as a function of wavelength showing scattering, absorption, and total opacities. 80

4.3 Bulk grid properties (10^3 $M_\odot$ cloud) 81

4.4 Column density snapshots (10^3 $M_\odot$ cloud) 82

4.5 2D slice of mass density with velocity vectors and ionization contour . . . 85

4.6 2D slice showing ionization fractions 87

4.7 Column density histograms (10^3 $M_\odot$ cloud) 88

4.8 Average ionized gas temperature (10^3 $M_\odot$ cloud) 90

4.9 Average electron density (10^3 $M_\odot$ cloud) 91

4.10 2D slice of the FUV flux around the most massive star 92

4.11 FUV flux vs time at the most massive star 93

4.12 FUV flux vs time at a 0.88 $M_\odot$ star 94

4.13 Three-colour images using synthetic observations of S II 6731 Å, Hα, and O III 5007 Å 100

4.14 Hα luminosities and extinctions as a function of time 102

4.15 Total production rate of Lyman continuum photons as a function of time . 104

4.16 Dust temperature extraction and comparison for synthetic observations at 450 and 850 µm 107

5.1 Positions of stars at the onset of feedback (10^4 $M_\odot$ cloud) 114

5.2 Parameter space of observed and simulated clouds 115

5.3 Bulk grid properties (10^4 $M_\odot$ cloud) 118

5.4 Column density snapshots (10^4 $M_\odot$ cloud) 119

5.5 Column density histograms (10^4 $M_\odot$ cloud) 121

5.6 Average ionized gas temperature (10^4 $M_\odot$ cloud) 122

5.7 Average electron density (10^4 $M_\odot$ cloud) 123

5.8 FUV flux at the positions of all stars in 10^4 $M_\odot$ cloud (part 1) 124

5.8 FUV fluxes at the positions of all stars in 10^4 $M_\odot$ cloud (part 2) 125

5.8 FUV fluxes at the positions of all stars in 10^4 $M_\odot$ cloud (part 3) 126

5.9 Column density snapshot with positions of massive star and star 5 with G_0 128

List of Tables

3.1 Overview of codes used to model photoionization feedback, as used in the cited papers (see section 3.4) 69

4.1 Total abundance of each element and the ionized states included in the simulation. 78

4.2 Initial parameters of the massive star. 78

Declaration

This thesis includes a paper, first-authored by me, which has been published in the Monthly Notices of the Royal Astronomical Society (Ali A., Harries T. J., Douglas T. A., 2018, MNRAS, volume 477, pp 5422–5436) – this is presented in chapter 4. The work in chapters 3 to 5 use the radiation hydrodynamics code, TORUS, which was developed by others including myself. I have provided specific attribution in the relevant places (particularly chapter 3).

Acknowledgements

Firstly, my thanks go to Tim Harries for his supervision, encouragement, and sense of humour. In the process of writing this thesis, I've come to realise just how steep a learning curve I ascended, with Tim's help and oversight. I'm also grateful for Matthew Bate for his secondary supervision, and Tom Haworth and Dave Acreman for their expertise in all things TORUS.

My acknowledgement and thanks also go to: my academic siblings, Tom H (again), Freddy, and Laura, for their time and their help, in all their manifestations. To Lis, Sally, and Tom W for being excellent office-mates, for silly chats, help with Python, help with pies, origami cranes, and for just being decent colleagues. To Tom G, Liv, Lis, Tom C, and Louis, for being good people, and for understanding understatement. To Ant and his puppy-like encouragement, and Olly and his complete disdain for academia, both of which only increased my determination to see this through all the way.

My funding was provided by STFC. The calculations for this thesis were performed on the DiRAC Complexity system at the University of Leicester and the DiRAC Data Centric system at Durham University. These form part of the STFC DiRAC HPC Facility. I also used the University of Exeter Supercomputer, Zen, a DiRAC Facility jointly funded by STFC, the Large Facilities Capital fund of BIS, and the University of Exeter.

Chapter 1

Introduction

Star formation takes place in giant molecular clouds (GMCs). In the big picture of star formation (reviewed in detail by Zinnecker & Yorke 2007), gravitational and turbulent motions create clumps and cores, and these collapse to form stars. As protostars contract, and later start fusing hydrogen on the main sequence, they emit radiation and expel material in the form of winds – this feedback clears material away from the natal environment, exposing the stars to the larger GMC environment. After a few Myr, the most massive stars will explode as supernovae (SNe), feeding back to the rest of the GMC where different stages of the star formation cycle may be occurring concurrently. After material is dispersed by the stellar feedback, the end product is observed as a stellar cluster or a more loosely bound stellar association (Lada & Lada 2003).

This general overview contains many unanswered questions. It is not clear, for example, how the most massive stars accrete their material. Do they form in cores in complete isolation or is their material drawn from further out, in competition with other stars? How does a star's radiation affect its formation, and once it is formed, how does it feed back into the wider environment? The star formation efficiency (SFE) – the proportion of a cloud's mass that is converted into stars – is observed to be only a few per cent in the Galaxy (Lada & Lada 2003); can feedback from massive stars stop further star formation by heating gas and displacing reservoirs, or do these mechanisms trigger the formation

of new stars by driving gas together? Which feedback processes dominate, and in which regimes?

These questions span several megayears in time, spatial scales from hundreds of AU to kiloparsecs, ten orders of magnitude in density, and temperatures across six orders of magnitude. Clearly, the problems are not simple. However, in the last few decades, there has been much work carried out to build up our understanding of star formation and feedback. In this chapter, I present an overview of the physical processes and the literature in this field, focusing on the most massive stars. The term *massive star* is usually given to those which are more than 8 $M_\odot$ and of spectral type O or B, as these will undergo a type II supernova at the end of their lifetime. A second definition puts this lower boundary at 20 $M_\odot$, as this is when stars begin to emit a significant amount of ionizing radiation (Reynolds 1984). I use the second definition in this thesis.

1.1 Star and cluster formation

1.1.1 Giant molecular clouds

GMCs have masses of the order 10^4 to 10^6 $M_\odot$, and sizes of a few to 100 pc (Solomon et al. 1987; Heyer et al. 2009). They contain dense clumps of 1000 $M_\odot$ ranging in sizes between 0.5 and a few pc. These clumps contain cores of 100 $M_\odot$ about 0.1 pc in radius. Clumps are made up of molecular hydrogen at temperatures between 10 to 20 K (Zinnecker & Yorke 2007).

Larson (1981) identified three scaling relations in an observed ensemble of clumps in GMCs. The first is the size-linewidth relation, $\sigma \propto R^{0.5}$, for radius R and 1D velocity dispersion σ. The second observation was that clouds are gravitationally bound objects in virial equilibrium. In a uniform density sphere, the total kinetic energy E_K and

gravitational potential energy E_G are given by

$$E_K = \frac{3}{2} M \sigma^2 \tag{1.1}$$

$$E_G = \frac{3}{5} \frac{GM^2}{R} \tag{1.2}$$

respectively, where M is the cloud mass, and G is the gravitational constant. The virial parameter can be defined as

$$\alpha_{\rm vir} = \frac{2E_K}{E_G} = \frac{5\sigma^2 R}{GM} \tag{1.3}$$

(e.g. Tan et al. 2014). In virial equilibrium, $E_K = E_G/2$, such that $\alpha_{\rm vir} = 1$ – this is the second Larson relation. The third relates particle number density and cloud radius, according to $n \propto R^{-1.1}$, which gives a nearly uniform mass surface density following $\Sigma \propto R^{-0.1}$.

Although early observations supported these relations (Solomon et al. 1987), more recently the observational techniques and selection criteria have been brought into question, with other studies producing different results, even within the same regions (e.g. Heyer et al. 2009; Traficante et al. 2018).

1.1.2 Collapse and accretion scenarios

As summarised in the review of Tan et al. (2014), there are two main models describing the process of star formation: core accretion and competitive accretion.

1.1.2.1 Core accretion

If a cloud's inward gravitational force can sufficiently overcome the outward thermal pressure force, the cloud becomes unstable and collapses (assuming the absence of magnetic fields, turbulence, and rotation, for simplicity). This occurs for $\alpha_{\rm vir} < 1$, giving a mass

limit beyond which a cloud collapses:

$$M > \left(\frac{kT}{G\mu m_H}\right)^{3/2} \rho^{-1/2} \tag{1.4}$$

where k is the Boltzmann constant, T is temperature, μ is the mean molecular weight in units of the hydrogen mass m_H, and ρ is the average density. The right hand side of equation (1.4) is the Jeans (1902) mass. A uniform density sphere collapsing under gravity will do so on the free-fall time scale,

$$t_{\rm ff} = \sqrt{\frac{3\pi}{32G\rho}} \tag{1.5}$$

As density increases during the collapse phase, the Jeans mass and free-fall time decrease, aiding fragmentation.

In *core accretion* (or *monolothic collapse*), a cloud collapses under its own gravity, fragmenting into multiple cores which are isolated from each other. These cores continue to contract to form stars. Each core may form one or a few stars, and there may be intra-core interactions and competition (Krumholz et al. 2009), but the final products do not depend on the evolution of any other cores, only the host core itself.

Core accretion is the typical scenario observed and modelled in the case of low-mass stars (Shu et al. 1987). Extending it to high-mass star formation has some complications. A massive protostar can reach the main sequence while still accreting material from the core. The timescale at which a protostar radiates away its gravitational potential energy as it contracts is the Kelvin–Helmholtz timescale,

$$t_{\rm KH} = \frac{GM_*^2}{R_* L_*} \tag{1.6}$$

for a stellar luminosity L_*. The gravitational collapse of the core occurs on the free-fall timescale (equation 1.5). For sufficiently massive protostars, $t_{\rm KH} < t_{\rm ff}$, meaning accretion continues while the star evolves along the main sequence (Shu et al. 1987; McKee & Tan

2003; Tan et al. 2014) and the resulting luminosity is such that radiation pressure onto dust grains can overpower the infall of material, setting an upper limit on the final stellar mass (Larson & Starrfield 1971; Wolfire & Cassinelli 1987). This problem can be overcome by removing the constraint of spherical symmetry, as shown by Yorke & Sonnhalter (2002) who carried out 2D numerical simulations with detailed radiative transfer for the dust grains – if the core has some initial rotation, it collapses into a disk in order to conserve angular momentum; the optically thick disk resists being blown away such that material can still accrete onto the star, with the stellar luminosity being directed along the disk rotation axis. This is the so-called *flashlight effect*. The core accretion scenario has also been modelled in 3D, with radiation hydrodynamical simulations being carried out by e.g. Krumholz et al. (2009), Kuiper et al. (2011), Klassen et al. (2016), Rosen et al. (2016), Harries et al. (2017), and Meyer et al. (2018) – these models show that different spatial resolutions and radiative transfer schemes may significantly affect results (for example, whether shells around cavities produced by radiation pressure become Rayleigh-Taylor unstable and funnel material down onto the protostar). This highlights the role of numerical algorithms and simulation setup in current star formation theory.

1.1.2.2 Competitive accretion

The second model is *competitive accretion*. Unlike core accretion, this occurs on a larger scale and occurs side by side with the formation of other stars. As the name suggests, stars compete for material – more massive stars can attract more mass, and hence grow even more massive, depleting the amount available for other stars. Accretion rates are higher where the gas density is higher, and thus the gravitational potential well is deeper, so the position of a star in a cluster is also crucial (Bonnell et al. 1997, 2001). The final stellar mass does not necessarily depend on the initial mass of the cloud or core (Bate et al. 2003; Bonnell et al. 2004; Smith et al. 2009), unlike in core accretion where it is effectively some fraction of the core mass. Furthermore, there will be a spectrum of masses since different stars will accrete at different rates (Zinnecker 1982).

Hydrodynamical models of competitive accretion display mass segregation, in which the most massive stars are located in the centre of clusters where the potential well is deepest (Bonnell et al. 2004). This is supported by observations of stellar distributions in many regions (Hillenbrand & Hartmann 1998; de Grijs et al. 2002; Pang et al. 2013). Dynamical interactions between stars after they have been formed can also cause or enhance segregation, even in clusters that are still young (McMillan et al. 2007; Moeckel & Bonnell 2009; Allison et al. 2009; Parker & Dale 2017), providing an alternative (or complementary) explanation. The inclusion of stellar feedback may hinder segregation, as expanding H II regions and winds can disrupt accretion flows, preventing the potential wells from getting deeper and producing smoother spatial distributions of stars (Parker & Dale 2017). Thus, even where competitive accretion occurs, there may not necessarily be mass segregation, and the presence of segregation is not sufficient to say that competitive accretion is the dominant star formation mechanism. The role of stellar feedback in clusters is discussed further in section 1.2.

1.1.3 Initial mass function

The distribution of masses of stars in a region can be described by the initial mass function (IMF),

$$\frac{\mathrm{d}N}{\mathrm{d}\log m} \propto m^{\Gamma} \tag{1.7}$$

giving a number of stars N in a stellar mass range between $\log m$ and $(\log m + \mathrm{d}\log m)$. The seminal works by Salpeter (1955), Kroupa et al. (1993) and Chabrier (2003) derived values for the power-law index Γ at different mass regimes. For $m \gtrsim 1\,\mathrm{M}_\odot$ stars follow the declining Salpeter IMF with $\Gamma = -1.35$. At lower masses, the scatter is greater, but results are still broadly consistent – between $0.1 \lesssim m \lesssim 1\,\mathrm{M}_\odot$ the slope flattens out, with Γ between -0.25 and 0, and below $0.1\,\mathrm{M}_\odot$, the IMF turns over with $\Gamma > 0.5$. Observations of both young and old clusters and field stars show little variation in the form of the IMF, particularly in the Salpeter regime, implying a universal relationship between stellar mass

and number (Bastian et al. 2010; Offner et al. 2014). This could be a result of a competitive accretion process, as the spectrum of stellar masses combined with dynamical interactions between stars shapes the IMF (Klessen et al. 1998; Bate et al. 2003; Krumholz et al. 2012). Alternatively, in the monolithic collapse scenario, if a certain fraction of a core is converted into stars, this implies that the overall core mass function (CMF) is similar in form to the stellar mass function; such a relationship has been observed (Motte et al. 1998; Nutter & Ward-Thompson 2007; André et al. 2010; Könyves et al. 2010), with the CMF perhaps shifted by a factor ≈ 3 higher in mass compared to the IMF (Alves et al. 2007; Offner et al. 2014).

1.2 Massive star feedback

The empirical mass–luminosity relation for main sequence stars follows

$$L \propto \begin{cases} M^{3.5} & M \lesssim 20\,\mathrm{M}_\odot \\ M & M \gtrsim 20\,\mathrm{M}_\odot \end{cases} \tag{1.8}$$

(Kuiper 1938) – this is illustrated in Fig. 1.1 using approximate proportionality constants of 1.5 and 3200, respectively (according to the review by Klessen & Glover 2016). The consequence of this strong scaling with mass is that OB stars dominate the energy output of a stellar cluster, despite their relative rarity. Furthermore, as effective temperatures exceed 10^4 K, their spectra peak in or near the ultraviolet (UV) – these energetic photons are able to photoionize atoms, photoexcite dust grains, photodissociate molecules, and exert strong radiation forces. The interaction between the stellar radiation field and the surrounding gas and dust can therefore alter the interstellar medium both thermally and dynamically, and this in turn may influence future star formation.

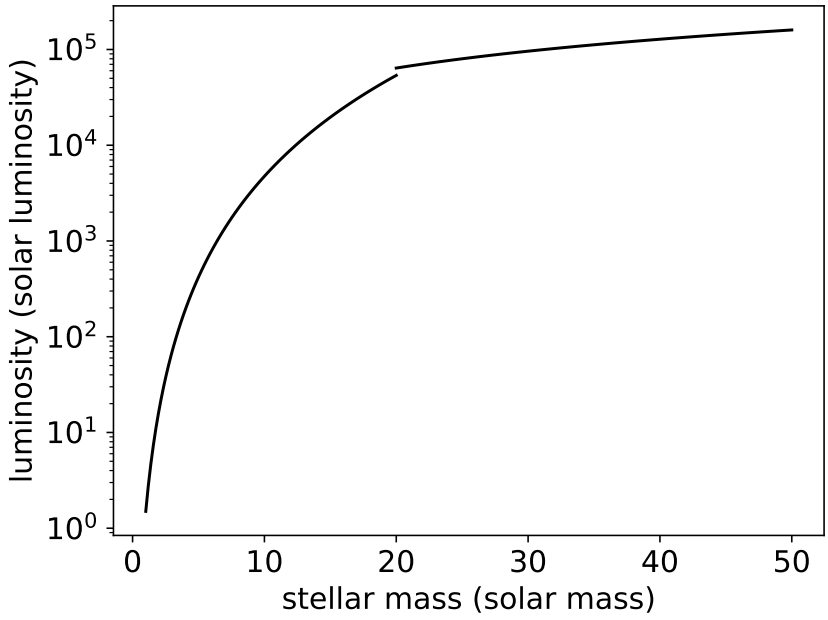

Figure 1.1: Approximate mass–luminosity relation for main sequence stars (equation 1.8).

1.2.1 Computational radiation hydrodynamics

The star formation scenarios discussed in the previous sections require the modelling of 3D hydrodynamics and N-body stellar interactions, plus radiative transfer for the stellar feedback. As models become more complex it becomes necessary to do this using computational methods.

There are three main classes of hydrodynamic codes depending on the method used to discretise fluid elements (reviewed in detail by Hopkins 2015): smoothed particle hydrodynamics (SPH), in which the total mass is split into particles which move along with the fluid; grid-based codes which split the volume into regular, static cells that can become smaller or larger depending on where the spatial resolution is required (called AMR, adaptive mesh refinement); and moving-mesh codes, which combine characteristics of both, having irregular, adaptive volume elements such as a Voronoi tesselation around points which follow the flow. Popular implementations of SPH in current use include GADGET (Springel et al. 2001, 2005), SPHNG (e.g. Bate 2014), PHANTOM (Price et al. 2017), and SEREN (Hubber et al. 2011). Grid codes include FLASH (Fryxell et al. 2000), RAMSES

(Teyssier 2002), ZEUS (Clarke 1996, 2010), ENZO (Bryan et al. 2014), and ORION (Klein 1999). The most common moving-mesh code is AREPO (Springel 2010).

There are also three commonly used methods of solving the equation of radiative transfer; a review of their usage in feedback models is given by Dale (2015). One is ray-tracing, in which lines are cast from a source of radiation (e.g. a star) to surrounding cells or particles of gas and dust, and the solution is then computed explicitly along each ray. The downside to ray-tracing is that once a ray is absorbed, the radiation that should be re-emitted by the fluid (called the *diffuse* or *indirect* radiation field) is neglected – for example, dust grains absorb ultraviolet radiation and re-emit in the infrared, and this may have a significant dynamical effect in star-forming clouds (Lopez et al. 2014).

Another method is flux-limited diffusion (FLD), which treats radiation as a fluid in the equations of RHD; this method works accurately in optically thick media but can break down in optically thin regimes. Hybrid algorithms exist which ray-trace from the star to an optically thick boundary, from which point the re-emitted radiation diffuses out in the FLD approximation (e.g. Kuiper et al. 2010a; Rosen et al. 2017). However, the greater accuracy of the hybrid technique comes with a greater computational cost.

Another method is Monte Carlo radiative transfer (MCRT), specific details of which are given in chapter 3. This involves propagating photon packets through a fluid in which they are scattered, absorbed, and re-emitted based on randomly sampled probability density functions – the more packets and events, the greater the statistical sampling of the radiation field. This technique handles direct and diffuse field components self-consistently, but introduces Poisson noise depending on the number of photon packets being used in the sampling – this leads to a greater processing requirement. It is currently the norm to advance a hydrodynamical model with a quicker but less detailed ray-tracing or FLD method (e.g. Bate et al. 2002; Dale et al. 2012, 2014), then to produce synthetic flux measurements using MCRT, post-processing the RHD snapshots for more accurate temperatures or ionization states (e.g. Kurosawa et al. 2004; Hubber et al. 2016; Koepferl et al. 2017a; Young et al. 2018). However, combining MCRT with the hydrodynamics

calculation self-consistently is becoming more common as processors and algorithms improve (e.g. Haworth & Harries 2012; Harries et al. 2017).

Examples of MCRT codes with grid structures include TORUS (Harries 2000; Harries et al. 2017), MOCASSIN (Ercolano et al. 2003), RADMC-3D (Dullemond & Dominik 2004), CMACIONIZE (Wood et al. 2004; Vandenbroucke & Wood 2018), MCFOST (Pinte et al. 2006), and HYPERION (Robitaille 2011). SPH implementations of MCRT are less common, but include the code by Forgan & Rice (2010) and SPAMCART (Lomax & Whitworth 2016).

These approaches can and have been used in the literature to study stellar feedback in star-forming regions, as the following sections describe.

1.2.2 Protostellar heating

As protostellar cores contract and accrete material, the gravitational potential energy of the collapsing gas is converted into thermal energy and radiation. This accretion luminosity heats the surrounding dust and gas to temperatures of a few tens to 100 K, increasing the Jeans mass, and providing support against further fragmentation of the protostellar disk (Krumholz 2006). Numerical simulations show that this radiative feedback regulates the formation of low-mass stars and brown dwarfs (Offner et al. 2009), and produces IMFs that are independent of initial cloud properties, hence giving an explanation for the universality of the IMF (Bate 2009, 2012). These studies show the importance of accurately accounting for dust properties and radiative transfer in the simulations, as models without them overestimate the formation of low-mass stars by factors of a few, and give temperatures that are lower than shown in observations.

On the other hand, there may be sufficient material in dense, massive clouds to exceed the increased Jeans mass, such that fragmentation still occurs. This will lead to the growth of high-mass protostars instead, which compete for material, diverting it away from other objects (Peters et al. 2010). Thus, the problem is complex hydrodynamically as well as radiatively.

1.2.3 Photoionization

Photons with energy greater than 13.6 eV are able to ionize atomic hydrogen. When a star begins to emit this radiation, each photon ionizes an atom, forming an ionization front (IF) around the star. This expands supersonically compared to the ionized gas, so its extent is determined by the radiative output of the star. This is termed the *R-type* expansion phase (Kahn 1954). As electrons recombine, photons are consumed in further absorptions to maintain the level of ionization. This, combined with the geometric dilution of the radiation field, slows down the progress of the IF until it approaches the sound speed, and the rate of ionizations balances the rate of recombinations. This marks the transition to *D-type* expansion (Kahn 1954), and occurs at the Strömgren (1939) radius; for a fully hydrogen gas, this is equal to

$$r_S = \left(\frac{3Q}{4\pi n_e^2 \alpha_B} \right)^{1/3} \tag{1.9}$$

where Q is the rate of ionizing photons emitted by the star, n_e is the electron density, and α_B is a recombination coefficient $\sim 2 \times 10^{-13}$ cm^3 s^{-1} at 10^4 K. The higher temperature in the H II region compared to the cold, neutral medium beyond causes a pressure gradient. The ionized gas therefore expands at the sound speed,

$$c_s = \sqrt{\frac{kT}{\mu m_H}} \tag{1.10}$$

which is $c_I \sim 10\,\mathrm{km\,s^{-1}}$ at 10^4 K (Dale et al. 2007a,c; Williams et al. 2018). As shown by Spitzer (1978) and Dyson & Williams (1980), the D-type evolution of the H II region radius with time t follows

$$r_I(t) = r_S \left(1 + \frac{7 c_I t}{4 r_S} \right)^{4/7} \tag{1.11}$$

For an ionizing flux of $10^{49}\,\mathrm{s^{-1}}$ and density $10^3\,\mathrm{cm^{-3}}$, $r_S = 0.7\,\mathrm{pc}$, and after 1 Myr, $r_I = 5\,\mathrm{pc}$. Clearly, an H II region around an O star in a cluster is not localised – it is bound to influence the cloud within which it forms.

1.2.3.1 Gas dispersal by photoionization

The impact of H II region expansion is complicated by the fact that real star-forming regions do not have completely uniform distributions of density. Whitworth (1979) used a two-dimensional axisymmetric model to study a molecular cloud surrounded by diffuse gas, with an O star located near the cloud's interior boundary. On the inner side of the cloud, the H II region growth is bounded by the propagation of radiation, while the outer side is density-bounded such that the expansion of ionized gas leads to the escape of material from the cloud into the diffuse surroundings. This configuration was also studied by Tenorio-Tagle (1979), who coined the term *champagne flow* to describe the outburst of ionized gas; if viewed face-on, with the champagne flow moving towards the observer, this appears as a *blister* H II region (Yorke et al. 1983). Bodenheimer et al. (1979) looked at other scenarios, such as a single long filament where ionized material disperses through two edges, as well a collision between a champagne flow and a dense, neutral blob in the diffuse area outside the cloud. These studies were followed by Yorke et al. (1989), who included supernovae after a period of ionization, and Franco et al. (1990) who took into account power-law density distributions. The conclusion from these early theoretical models was that ionizing feedback from massive stars can efficiently disperse their host molecular clouds, even with a small star formation efficiency of a few per cent.

The issue becomes more complex in three-dimensional, inhomogeneous gas distributions. Numerical simulations of photoionizing feedback in such conditions began with Dale et al. (2005). Unlike previous studies, they concluded that clouds may not necessarily be destroyed by ionizing radiation, as a small fraction of the gas may effectively shield the rest of the cloud, carrying significant amounts of energy out of the system instead of distributing it evenly. Later parameter studies by Dale et al. (2012) and Dale et al. (2013a) found that the degree of dispersal was closely coupled to the initial conditions of their simulations, such as cloud mass and hence escape velocity; for example, a significant fraction of gas was expelled in low-mass GMCs ($M = 10^4$ to 10^5 $M_\odot$, where the ionized

sound speed exceeds the escape velocity), but higher mass clouds (10^6 $M_\odot$) were mostly undisturbed.

The location of stars relative to the filamentary structure must also be taken into account. Dense gas can block the expansion of ionization fronts (Dale & Bonnell 2011), and gas and radiation may leak out through cavities present in the initial conditions (Dale et al. 2005; Dale & Bonnell 2011; Dale 2017). How effectively this stops the dispersal of gas is not clear, as some studies still find effective destruction of clouds with highly fractal geometries (Walch et al. 2012). The number of massive stars is also a factor, as Geen et al. (2016) found that a star formation efficiency greater than 10 per cent is required to disperse a 10^5 $M_\odot$ cloud.

To what extent a cloud is destroyed by ionizing feedback is evidently still uncertain, and is heavily dependent on initial conditions (which may be unrealistic; Rey-Raposo et al. 2015). Nonetheless, the motions and heating of gas can still lead to the reduction in the SFE and SFR (Colín et al. 2013), bringing them closer to observational findings (Geen et al. 2017).

The presence of dust is of vital importance as dust grains absorb ionizing photons and re-emit in the infrared. Haworth et al. (2015) investigated the relative role of different microphysics on the expansion of H II regions, using the TORUS Monte Carlo radiative transfer and hydrodynamics code. They concluded that dust is important in the early stages of the evolution, as the rate $\dot{N}_{\rm Ly}$ that goes into ionizing the gas is reduced; the effect is to reduce the Strömgren radius $r_{\rm S}$ by about 10 per cent, since $r_{\rm S} \propto \dot{N}_{\rm Ly}^{1/3}$. Haworth et al. also tested how temperatures affect the expansion. By treating the radiation field polychromatically, including the diffuse radiation from gas as well as stellar radiation, and also including cooling from helium and metals, the ionized radius at later times is reduced by another 10 per cent compared to models which only consider hydrogen and a monochromatic, on-the-spot treatment (see section 2.3.3). For this reason, I include the full microphysics in the simulations presented in chapter 4 (published in Ali et al. 2018) and chapter 5, thus improving upon previous simplifications.

1.2.3.2 Star formation triggered by photoionization

Expelling gas reservoirs will hinder the formation of stars, but the expansion of material could also trigger star formation. Elmegreen & Lada (1977), Whitworth et al. (1994), and Elmegreen et al. (1995) showed that expanding H II regions can drive material together into dense layers which become gravitationally unstable and collapse to form stars – this is termed *collect and collapse*. These stars could go on to induce a further wave of star formation once they become ionizing sources themselves. Alternatively, an external source of radiation may compress material that is already in place and intially stable – this is called the *radiatively driven implosion* scenario (RDI; Bertoldi 1989).

The number of numerical simulations aiming to determine the efficacy of these scenarios has increased in recent years, whether looking at clouds irradiated from the inside such that gas collects and collapses (Dale et al. 2005, 2007a; Walch et al. 2013) – or irradiated from the outside to cause RDI (Kessel-Deynet & Burkert 2003; Dale et al. 2007b; Gritschneder et al. 2009; Bisbas et al. 2011; Dale & Bonnell 2012; Haworth & Harries 2012). Although these models do find evidence of triggered star formation, any increases in star formation efficiency and rate appear to be modest – the positive impact of photoionization feedback is likely to be weaker than the negative impact.

1.2.4 Stellar winds

Line scattering at the surfaces of O stars drives winds with terminal velocities exceeding 1000 km s^{-1}, and these winds can shock-heat the surrounding gas to temperatures reaching 10^7 K. This process can carve out a bubble of low-density hot gas surrounded by a cold dense shell. The cumulative amount of energy released over the main sequence lifetime approaches that of a supernova explosion (see section 1.2.7; Castor et al. 1975a,b; Weaver et al. 1977)

Different treatments of stellar winds in numerical simulations include injecting mass with energy/momentum (Dale & Bonnell 2008; Wünsch et al. 2008; Pelupessy & Portegies

Zwart 2012; Rogers & Pittard 2013; Agertz et al. 2013; Fierlinger et al. 2016; Gatto et al. 2017), or increasing momentum in a sphere of influence (Dale & Bonnell 2008; Dale et al. 2013b; Ngoumou et al. 2015; Rey-Raposo et al. 2017) – the latter assumes the hot gas mixes with the swept-up cold gas before blowing out into the wider environment, thus the wind is treated as just a ram pressure at GMC scales.

Rogers & Pittard (2013) injected thermal energy as their wind, which blows out a bubble in a turbulent, inhomogeneous clump surrounded by diffuse gas. The bubble escapes out of the clump, and gas at 10^7 K streams out through low-density channels. Some of the dense gas gets ablated into the flow, while other parts effectively act as a shield. This allows almost 75 per cent of the wind energy to escape. Other authors with different methods find a similar result, that material can simply stream out in highly structured clouds, leaving the cloud gas relatively untouched (Fierlinger et al. 2012; Dale et al. 2013b) – the efficacy of winds in disrupting GMCs seems to depend on the initial density structure. In some cases, winds may be able to shut off star formation close to the wind-producing star by dispersing the gas (Dale et al. 2013b). However, simulations which combine ionization with winds find that although the latter can create small cavities in low-mass clouds (Dale et al. 2014), the overall cloud structure is shaped more by ionization than by winds, and a wind's dynamical impact is usually localised (Ngoumou et al. 2015; Dale et al. 2013b). The smaller range of influence combined with the weaker driving of gas means triggered star formation may be negligible in the case of winds, compared to photoionization (Dale et al. 2013b; Ngoumou et al. 2015).

Relatively few simulations have combined the effects of winds acting in concert with ionization, and they have differing levels of complexity in the implementations due to the computational cost (as reviewed by Dale 2015). Models that do include winds tend to simplify (or neglect completely) the radiative transfer, so the combination of winds and accurate photoionization (including dust) is something that has yet to be studied in great detail.

1.2.5 Radiation pressure

As radiation interacts with matter, it transfers momentum, which on macroscopic scales exerts a pressure. This is usually via scattering or absorption by dust grains, or absorption of ionizing photons by gas.

Very luminous massive protostars were thought to produce enough radiation pressure to halt the infall of material beyond an upper mass limit between 40 and 60 $M_\odot$ (Ledoux 1941; Schwarzschild & Härm 1959; Larson & Starrfield 1971; Kahn 1974; Kuiper et al. 2010b). Removing the constraint of spherical symmetry allows material to accrete via a disk, with the radiation pressure escaping perpendicular to the disk. This still provides some dynamical feedback, as it creates bipolar cavities of low-density gas surrounded by high-density shells (Krumholz et al. 2009; Kuiper et al. 2010b; Harries et al. 2017).

On GMC scales, radiation pressure feedback will occur side by side with photoionization feedback. Radiation pressure can form cavities in the centre of H II regions (Mathews 1967; Inoue 2002) and sculpt gas into shells (Draine 2011). However, for radiation pressure to be comparable in magnitude to ionization-driven thermal pressure, cluster luminosities greater than 10^{50} ionizing photons per second (Krumholz & Matzner 2009) are required for densities around 100 cm^{-3} (Draine 2011) – massive clusters or high surface densities may be required for radiation pressure to have a significant role (Fall et al. 2010). The impact may be more pronounced, or even dominant, on galactic scales, as shown by Hopkins et al. (2012) who carried out simulations with simple prescriptions for ionization heating, stellar winds, radiation pressure and SNe; radiation pressure was one of the dominant regulators of the SFR, with its absence causing ten times greater SFRs in some cases. Similarly, Agertz et al. (2013) showed that the combined momentum injection by radiation pressure and stellar winds removes dense gas and lowers star formation.

Observationally, there is still uncertainty as to the role of radiation pressure relative to other feedback mechanisms in H II regions. In 30 Doradus, Lopez et al. (2011) observed

that it dominates over the pressure from ionized gas, as well as the hot gas from stellar winds (10^6 to 10^7 K); however, Pellegrini et al. (2011) found the opposite, concluding that the wind gas is overall more important in shaping the region. Furthermore, the precise source of photons must be taken into account, as some H II regions regions exhibit radiation pressure from stellar photons dominating over the dust-processed infrared radiation (Lopez et al. 2011), while other regions show the opposite (Lopez et al. 2014).

Modelling these conditions has proven difficult, as it has either required subgrid models with momentum injection (Hopkins et al. 2012; Agertz et al. 2013), or radiative transfer with simplified trapping factors to account for the reprocessing of stellar photons as they travel through an optically thick medium (e.g. Krumholz & Thompson 2012). Some models neglect either the direct or indirect radiation field altogether, depending on their problem of interest (e.g. Wise et al. 2012; Kim et al. 2013; Skinner & Ostriker 2015; Raskutti et al. 2016; Kim et al. 2017b).

1.2.6 Far-ultraviolet radiation

Ultraviolet (UV) and far-ultraviolet (FUV) photons with energy greater than 5 eV can photodissociate molecular hydrogen into its constituent atoms by exciting its vibrational modes (Stecher & Williams 1967). If it acts in concert with photoionization, the result is a region of ionized gas at 10^4 K, bounded by a shell of atomic gas at 100 K (termed the photodissociation region, or PDR), surrounded by molecular gas at 10 K.

Hosokawa & Inutsuka (2005) showed that the expanding shock front can overtake the dissociation front, and the atomic shell can reform molecules if sufficiently dense, resulting in a molecular shell. If massive enough, this can become gravitationally unstable, triggering further star formation (Hosokawa & Inutsuka 2006a,b). Photodissociation could also be a negative feedback effect due to the increased temperature and particle number density – for example, Butler et al. (2017) modelled dissociating and ionizing radiation as well as SNe on kiloparsec scales, and found that H_2 photodissociation caused the most

significant reduction to the SFE. The impact of photodissociation on star formation is still a relatively unexplored area, with simulations only recently starting to consider it in concert with other types of feedback (e.g. Peters et al. 2017).

The FUV field between 5 and 13.6 eV also causes heating via photoelectric ejection off dust grains (Draine 1978). In protoplanetary disks, external irradiation from massive stars in a cluster can be more significant than internal irradiation by many orders of magnitude (Bruderer et al. 2012). Models including both radiation from the host star as well as the interstellar radiation show that the latter is the dominant mechanism in photoevaporating the disk (Anderson et al. 2013). It leads to the shape of proplyds observed in the Orion Nebula (Richling & Yorke 2000) and may eventually cause their destruction (Johnstone et al. 1998).

1.2.7 Supernovae

The most massive stars will explode as supernovae (SNe) after a few Myr, releasing 10^{51} erg of energy into the conditions created by the aforementioned feedback processes. Galactic scale simulations show that SN feedback regulates star formation, producing SFRs that are more in line with observations (Dobbs et al. 2011; Hopkins et al. 2012). On individual GMC scales, modelling has been carried out to find how efficiently the energy is transferred to the gas (e.g. Iffrig & Hennebelle 2015). Models have also combined SNe with ionizing radiation (Yorke et al. 1989; Geen et al. 2016), stellar winds (Pelupessy & Portegies Zwart 2012; Rogers & Pittard 2013; Krause et al. 2013; Walch & Naab 2015; Fierlinger et al. 2016; Rey-Raposo et al. 2017), or both (Peters et al. 2017). A common finding is that if the main sequence feedback produces porous environments, the SN energy is not effectively deposited into the gas (as little as 1 to 10 per cent might be transferred), but escapes through low-density channels instead (Fierlinger et al. 2012; Dale et al. 2012, 2013a; Rogers & Pittard 2013; Geen et al. 2016; Rey-Raposo et al. 2017).

1.3 Aims of this thesis

As shown in the previous sections, the role of massive star feedback in shaping molecular clouds, dispersing gas, and modifying star formation has not yet been thoroughly pinned down. In recent times, numerical simulations have been used to study this from a theoretical standpoint. However, there is still much room for improvement when it comes to the level of physical detail included in models, particularly on the scales of stellar clusters and GMCs, and especially as far as radiative transfer is concerned.

As part of this PhD project, I have attempted to make advancements in these areas by applying the microphysical detail of a dedicated Monte Carlo radiative transfer code, side-by-side with hydrodynamics, on the scale of stellar clusters. This also allows the self-consistent creation of synthetic observations, such that observational diagnostics can be tested. In particular, I focus on the radiative feedback from massive stars – that is, photoionization and radiation pressure. I lay out the basic theory and physical concepts in chapter 2, show how they are used computationally in chapter 3, and apply them to simulated clouds of 10^3 and $10^4\,\mathrm{M}_\odot$ (chapters 4 and 5, respectively). I then summarise my conclusions, along with possible future avenues of study, in chapter 6.

Chapter 2

Radiation hydrodynamics

In this chapter I present the theoretical background, definitions, and equations of radiative transfer and hydrodynamics, as they relate to star formation and feedback. For a more comprehensive description of the theory, I refer the reader to Chandrasekhar (1960), Mihalas & Weibel-Mihalas (1999), Osterbrock & Ferland (2006), and lecture notes by Howarth (2010) and Dullemond (2012).

2.1 Definitions for radiation

The specific intensity I_ν describes the energy $\mathrm{d}E_\nu$ of a ray of light in the frequency range $\nu, \nu + \mathrm{d}\nu$, passing through a unit area $\mathrm{d}A$ with surface normal at an angle θ to the observer, through a solid angle $\mathrm{d}\Omega$, for a time $\mathrm{d}t$:

$$I_\nu = \frac{\mathrm{d}E_\nu}{\mathrm{d}t\,\mathrm{d}A\cos\theta\,\mathrm{d}\nu\,\mathrm{d}\Omega}. \quad [\mathrm{erg\,s^{-1}\,cm^{-2}\,Hz^{-1}\,sr^{-1}}] \quad (2.1)$$

This can be converted to wavelength units via

$$I_\lambda = I_\nu \left|\frac{\mathrm{d}\nu}{\mathrm{d}\lambda}\right|. \quad [\mathrm{erg\,s^{-1}\,cm^{-3}\,sr^{-1}}] \quad (2.2)$$

The total intensity is simply I_ν integrated over frequency

$$I = \int_0^\infty I_\nu \, \mathrm{d}\nu \,. \qquad [\mathrm{erg\,s^{-1}\,cm^{-2}\,sr^{-1}}] \quad (2.3)$$

In addition to the specific intensity, it is useful to define the mean intensity J_ν by averaging I_ν over solid angle:

$$\begin{aligned} J_\nu &= \frac{\int I_\nu \, \mathrm{d}\Omega}{\int \mathrm{d}\Omega} \\ &= \frac{1}{4\pi} \int I_\nu \, \mathrm{d}\Omega \end{aligned} \qquad [\mathrm{erg\,s^{-1}\,cm^{-2}\,Hz^{-1}\,sr^{-1}}] \quad (2.4)$$

and the physical flux F_ν by integrating over all angular directions:

$$F_\nu = \int I_\nu \cos\theta \, \mathrm{d}\Omega \,. \qquad [\mathrm{erg\,s^{-1}\,cm^{-2}\,Hz^{-1}}] \quad (2.5)$$

If the ray travels at speed c, the monochromatic energy density u_ν (the radiant energy per unit volume) can be defined using the specific intensity:

$$u_\nu = \frac{1}{c} \int I_\nu \, \mathrm{d}\Omega \,. \qquad [\mathrm{erg\,cm^{-3}\,Hz^{-1}}] \quad (2.6)$$

Comparing with equation (2.4) results in

$$u_\nu = \frac{4\pi J_\nu}{c}. \quad (2.7)$$

This expression is useful in calculations of radiative equilibrium and photoionization equilibrium, as I describe in the following sections. The total flux, total mean intensity, and the total energy density are the integrals of the monochromatic variables over frequency, similar to equation (2.3).

2.2 Radiative transfer

As the ray moves a distance ds through a medium, it is absorbed and scattered by particles, which has the effect of attenuating the ray. Sources of opacity are discussed in section 2.3. If the cross-section per particle is a_ν (in cm^2) and the number of particles per unit volume is n (cm^{-3}), the opacity per unit length k_ν (cm^{-1}) and opacity per unit mass κ_ν (cm^2 g^{-1}) can be defined according to

$$a_\nu n = k_\nu = \kappa_\nu \rho \tag{2.8}$$

where ρ (g cm^{-3}) is the mass density. The attenuation as a function of distance is therefore

$$\mathrm{d}I_\nu = -k_\nu(s) I_\nu \, \mathrm{d}s \, . \tag{2.9}$$

The intensity can also increase via emission from the medium,

$$\mathrm{d}I_\nu = j_\nu(s) \, \mathrm{d}s \tag{2.10}$$

where j_ν is the emission coefficient of the medium. Therefore the net increase in specific intensity is

$$\mathrm{d}I_\nu = (-k_\nu I_\nu + j_\nu) \, \mathrm{d}s \, . \tag{2.11}$$

Defining the optical depth dτ_ν and the source function S_ν to be

$$\mathrm{d}\tau_\nu = k_\nu \, \mathrm{d}s \tag{2.12}$$

$$S_\nu = \frac{j_\nu}{k_\nu} \qquad [\mathrm{erg\,s^{-1}\,cm^{-2}\,Hz^{-1}\,sr^{-1}}] \tag{2.13}$$

means equation (2.11) can be rewritten as

$$\frac{\mathrm{d}I_\nu}{\mathrm{d}\tau_\nu} = -I_\nu + S_\nu . \tag{2.14}$$

This is the equation of radiative transfer. The formal solution to this is

$$I_\nu(\tau_\nu) = I_\nu(0)\mathrm{e}^{-\tau_\nu} + \int_0^{\tau_\nu} S_\nu(t_\nu)\mathrm{e}^{-(\tau_\nu - t_\nu)}\,\mathrm{d}t_\nu \tag{2.15}$$

where t_ν is a dummy variable representing an optical depth along the ray. The first term describes the extinction of the beam originating at $\tau_\nu = 0$, while the second term describes the extinction of radiation emitted at position t_ν as it travels to position τ_ν. An example problem is radiation emitted by a star, which interacts in some way with an intervening cloud of gas on the way to the observer - the background starlight is extincted in the cloud (the first term), and the cloud may produce its own radiation field (that is itself extincted; the second term); the total intensity at some point is then given by equation (2.15). The source function makes this difficult to solve analytically – it is not always known in advance, and S_ν and I_ν are interdependent. This means numerical methods are usually used instead of integrating the formal solution directly. One such method is Monte Carlo radiative transfer, which is described in section 3.2. Other methods are outlined in section 1.2.1.

When matter is in thermal equilibrium, the source function is equal to the Planck function, B_ν, at temperature T:

$$B_\nu(T) = \frac{2h\nu^3}{c^2}\frac{1}{\exp\left(h\nu/kT\right) - 1} \tag{2.16}$$

and therefore equation (2.13) becomes

$$B_\nu = \frac{j_\nu}{k_\nu} \tag{2.17}$$

which is known as Kirchoff's law. In the limit $h\nu \ll kT$, i.e. the Rayleigh-Jeans approximation, the Planck function becomes

$$B_\nu(T) \approx \frac{2kT\nu^2}{c^2} \qquad (h\nu \ll kT) \tag{2.18}$$

and in the limit $h\nu \gg kT$, or the Wien approximation, it is

$$B_\nu(T) \approx \frac{2h\nu^3}{c^2} \exp\bigl(-h\nu/kT\bigr). \qquad (h\nu \gg kT) \quad (2.19)$$

These equations are useful for calculating collisional processes such as free–free emission.

The primary astrophysical regions of interest in this thesis are H II regions within star-forming clouds. In the following sections, I describe the physical processes in play in such regions, and how they contribute to the transport of radiation. I lay out the sources of emission and opacity in atomic gas, before moving on to dust grains.

2.3 Emission and absorption by gas

In interactions between radiation and atomic gas, photons are emitted and absorbed when charged particles undergo transitions between energy levels or are accelerated/decelerated. These can be categorised into three main types depending on the boundness of the charges:

- bound-bound radiation. As a bound electron traverses energy levels inside an atom, it emits or absorbs a photon of energy equal to the difference in energy levels. This is a spectral line process, as the radiative energy is set by the discrete atomic energy levels.

- bound-free radiation. This includes photoionization, in which a bound electron absorbs a photon and is released from the atom with some kinetic energy. The inverse process is recombination, when a free electron becomes bound to an ion. Since the free electron can have an arbitrary amount of kinetic energy, this results in a continuous spectrum. The recombined electron will then cascade down in a series of bound-bound transitions.

- free-free radiation. This involves interactions between two free charged particles, for example an electron and an ion. As an electron decelerates when passing by the

ion, it emits radiation in a continuous manner.

Each process has an emissivity or opacity associated with it, and these will contribute to the source term in the equation of radiative transfer. Therefore, to characterise the intensity of the resulting radiation, it is necessary to understand the microphysical origin of each process. Furthermore, the emission and absorption of radiation will contribute to the energy gains and losses of a system, thereby changing the temperature of the medium.

2.3.1 Heating and cooling processes

In H II regions, the primary source of gas heating is photoionization of H and He, and this is balanced by cooling via recombination lines, collisionally excited lines from metal ions, and free-free continuum; that is, their rates follow

$$\Gamma_{\rm ion} = \Lambda_{\rm rec} + \Lambda_{\rm col} + \Lambda_{\rm ff} + \Lambda_{\rm gas\text{-}dust}. \qquad [\rm erg\,s^{-1}\,cm^{-3}] \quad (2.20)$$

$\Lambda_{\rm gas\text{-}dust}$ accounts for collisional heat exchange with dust grains and is described further in section 2.4. The total cooling rate for a radiative process is the emission it produces over all frequencies:

$$\Lambda = \int 4\pi j_\nu \, {\rm d}\nu \quad (2.21)$$

where the term in the integrand is the emissivity, ϵ_ν. In the following sections, I describe the nature of the gas heating and cooling rates.

2.3.2 Photoionization

A bound electron which absorbs radiant energy that is greater than the ionization potential, ϕ, of the energy level will become unbound from the atom. If the absorbed photon packet had an energy $h\nu$, an amount $\phi = h\nu_I$ will go into unbinding the electron, while the rest goes into the kinetic energy of the free electron; that is, $h\nu = \phi + E_K$.

If some species X is being photoionized from state i to an excited state $i+1$, the number of photoionizations in the gas per unit time, per unit volume is (Osterbrock & Ferland 2006)

$$\dot{n}_{\rm ion} = n(X^i) \int_{\nu_I}^{\infty} \frac{a_\nu(X^i) 4\pi J_\nu}{h\nu} \, {\rm d}\nu \qquad [{\rm cm}^{-3}\,{\rm s}^{-1}] \quad (2.22)$$

where ν_I is the minimum frequency required for ionization, $n(X^i)$ is the number density of species X^i, and $a_\nu(X^i)$ is the photoionization cross-section in units of cm^2. The kinetic energy of the free electrons goes into heating the gas at a rate

$$G(X^i) = n(X^i) \int_{\nu_I}^{\infty} \frac{a_\nu(X^i) 4\pi J_\nu}{h\nu} (h\nu - h\nu_I) \, {\rm d}\nu \, . \quad (2.23)$$

2.3.3 Recombination

The rate of recombinations per unit volume which take X from ionization state $i+1$ to i is

$$\dot{n}_{\rm rec} = n_e n(X^{i+1}) \alpha(X^i, T) \qquad [{\rm cm}^{-3}\,{\rm s}^{-1}] \quad (2.24)$$

where $\alpha(X^i, T)$ is the recombination coefficient. Two regimes of recombination can be considered. The first, case A, includes recombinations to all energy levels n, including the ground state $n = 1$:

$$\alpha_A = \sum_{n=1}^{\infty} \alpha_n \qquad [{\rm cm}^3\,{\rm s}^{-1}] \quad (2.25)$$

where α_n is the recombination coefficient to a particular energy level n. Recombinations directly to the ground state will result in the emission of an ionizing photon; in an optically thick medium, where the mean free path of photons is small and it is likely to be absorbed instantaneously by a nearby atom, this contribution may be subtracted from the total recombination coefficient. This is called the *on-the-spot* approximation and leads to the case B recombination coefficient:

$$\alpha_B = \sum_{n=2}^{\infty} \alpha_n . \quad (2.26)$$

For hydrogen, this has a value of $\approx 2 \times 10^{-13}\,\mathrm{cm^3\,s^{-1}}$ at $T = 10^4\,\mathrm{K}$.

The emission coefficient for a spontaneous radiative decay from a higher energy level j to a lower level i is

$$j_\nu = \frac{1}{4\pi} n_j h\nu_{ji} A_{ji} \tag{2.27}$$

where A_{ji} is the Einstein coefficient for spontaneous emission (in $\mathrm{s^{-1}}$). In a hydrogen atom, the levels j, i are described by the primary quantum number, n, and the orbital quantum number, l, such that the change in l is $\Delta l = l' - l = \pm 1$, while the change in n is $\Delta n = n' - n > 0$. The cooling rate due to recombination into species X^i is

$$\Lambda_{\mathrm{rec}}(X) = n_e n(X^{i+1}) kT\beta(X^i, T) \tag{2.28}$$

where β is the kinetic energy-averaged recombination coefficient.

When the rates of photoionization and recombination are equal, the relative densities of successive ionization states are given by

$$\frac{n(X^{i+1})}{n(X^i)} = \frac{1}{n_e \alpha(X^i, T)} \int_{\nu_I}^{\infty} \frac{a_\nu(X^i) 4\pi J_\nu}{h\nu}\,\mathrm{d}\nu\,. \tag{2.29}$$

Photoionization equilibrium also gives the Strömgren radius as discussed in section 1.2.3 (Osterbrock & Ferland 2006).

2.3.4 Free-free continuum

Radiation is emitted and absorbed when an electron scatters off an ion, as the electron is accelerated or decelerated in the process. This is also known as Bremsstrahlung (braking radiation) or free-free radiation. The free-free opacity is (Rybicki & Lightman 1979)

$$\begin{aligned} k_\nu^{\mathrm{ff}} &= \frac{4e^6}{3m_e hc}\left(\frac{2\pi}{3km_e}\right)^{1/2} Z^2 T^{-1/2} n_e n_i \nu^{-3}(1 - \mathrm{e}^{-h\nu/kT}) g_\nu^{\mathrm{ff}} \\ &= 3.7 \times 10^8 Z^2 T^{-1/2} n_e n_i \nu^{-3}(1 - \mathrm{e}^{-h\nu/kT}) g_\nu^{\mathrm{ff}} \end{aligned} \tag{2.30}$$

where Z is the atomic number, and $g_\nu^{\rm ff}$ is the Gaunt factor and depends on the impact parameter of the electron as it approaches the ion. From Kirchoff's law (equation 2.17), the emission coefficient is

$$j_\nu^{\rm ff} = 5.4 \times 10^{-39} Z^2 T^{-1/2} n_e n_i \mathrm{e}^{-h\nu/kT} g_\nu^{\rm ff}. \tag{2.31}$$

At radio wavelengths, which is the regime of interest in H II regions, these expressions become

$$k_\nu^{\rm ff} = 0.018 Z^2 T^{-3/2} n_e n_i \nu^{-2} g_\nu^{\rm ff} \qquad (h\nu \ll kT) \tag{2.32}$$

$$j_\nu^{\rm ff} = 5.4 \times 10^{-39} Z^2 T^{-1/2} n_e n_i g_\nu^{\rm ff} \qquad (h\nu \ll kT) \tag{2.33}$$

and the Gaunt factor is well approximated by (Osterbrock & Ferland 2006)

$$g_\nu^{\rm ff} = \frac{\sqrt{3}}{\pi} \left[\ln \left(\frac{T^{3/2}}{Z\nu} \right) + 17.7 \right]. \qquad (h\nu \ll kT) \tag{2.34}$$

Integrating the emission coefficient over frequency leads to the total cooling rate via free-free emission

$$\Lambda_{\rm ff} = 1.4 \times 10^{-27} Z^2 T^{1/2} n_e n_i \langle g_{\rm ff} \rangle \tag{2.35}$$

where $\langle g_{\rm ff} \rangle$ is the frequency-averaged Gaunt factor and takes the form

$$\langle g_{\rm ff} \rangle = 1.1 + 0.34 \exp \left[-\frac{(5.5 - \log_{10} T)^2}{3} \right] \tag{2.36}$$

(Wood et al. 2004; Katz et al. 1996; Spitzer 1978).

2.3.5 Collisionally excited forbidden lines

Bound electrons can be excited by free electrons via collisions. An excited electron can also be collisionally de-excited (in which case the energy is simply transferred to the

other electron), or it can spontaneously decay, resulting in the emission of a photon. Calculating the emissivity requires knowing which energy levels the electrons populate, over an ensemble of atoms.

In statistical equilibrium, the rate of populating a level i across the ensemble equals the rate of *de*-populating that level, whether by radiative decay or collisional processes; that is,

$$\sum_{j\neq i} n_e n_j q_{ji} + \sum_{j>i} n_j A_{ji} = \sum_{j\neq i} n_e n_i q_{ij} + \sum_{j<i} n_i A_{ij} \quad [\mathrm{cm^{-3}\,s^{-1}}] \tag{2.37}$$

where the subscript ij denotes a transition from i to j, q_{ij} is the rate coefficient for collisions (in $\mathrm{cm^3\,s^{-1}}$), and A_{ij} is the Einstein coefficient for spontaneous emission. The first term on the left hand side describes collisional excitations and de-excitations from levels j into level i; the second term term counts radiative decays from upper levels j into the lower level i. On the right hand side, the first term sums collisional de-excitations and excitations out of level i into levels j; the second term counts radiative decays from i to lower levels j. The level populations can be found relative to the total density of the species, $n(X)$, by using

$$n(X) = \sum_i n_i \tag{2.38}$$

and solving equation (2.37). From equation (2.27), the emission coefficient for radiative decay is then

$$j_\nu^{\mathrm{col}} = \frac{1}{4\pi} n_i h\nu_{ij} A_{ij} \tag{2.39}$$

(Peimbert et al. 2017) and the total cooling rate for all lines from species X is

$$\Lambda_{\mathrm{col}}(X) = \sum_i n_i \sum_{j<i} h\nu_{ij} A_{ij} \tag{2.40}$$

for transitions from level i to j.

[O II], [O III] and [N II] lines contribute significantly to the grand total cooling rate, at least a factor of a few times more than free-free radiation at temperatures of $\sim 10^4$ K (Osterbrock & Ferland 2006). These ions are included in the numerical simulations

presented in chapters 4 and 5.

2.4 Dust processes

Dust grains can be heated by absorbing radiation and cooled down via thermal emission, with the rates being, respectively,

$$\dot{A} = 4\pi \int k_\nu J_\nu \, \mathrm{d}\nu \tag{2.41}$$

$$\dot{E} = 4\pi \int k_\nu B_\nu(T) \, \mathrm{d}\nu \tag{2.42}$$

(Lucy 1999). Energy can also be transferred between dust grains and gas particles through collisions. An expression for this transfer rate is derived by Hollenbach & McKee (1979), and takes the form

$$\Lambda_{\text{gas-dust}} = 2 f n_H n_d \sigma_d v_p k_B (T_g - T_d) \tag{2.43}$$

where n_d, σ_d, T_d are the number density, cross-section and temperature of dust grains, v_p is the thermal speed of protons at the gas temperature T_g, and f depends on the ionization state and gas temperature. Depending on the sign of $(T_g - T_d)$, this can be a heating rate or a cooling rate for the gas (and vice versa for the dust).

Dust grains can also scatter photons, exchanging momentum. The post-scattering direction depends on the relationship between wavelength and grain size, a. In the regime where $\lambda \gg 2\pi a$, the process can be characterised by Rayleigh scattering. The scattering cross-section is given by

$$\sigma = \frac{2\pi^5}{3} \left| \frac{n^2 - 1}{n^2 + 2} \right|^2 \frac{(2a)^6}{\lambda^4} \tag{2.44}$$

where n is the complex refractive index of the grain. The phase function, which gives the probability of scattering to outward angle θ relative to the incoming direction, is

$$p(\cos\theta)_{\text{Rayleigh}} = \frac{3}{8}(1 + \cos^2\theta). \tag{2.45}$$

When $\lambda \sim 2\pi a$ or $\lambda \ll 2\pi a$, Mie theory is required, treating the grain as a uniform sphere. This increases in difficulty with relative size scale, but the phase function of Mie scattering favours scattering in the forward direction (Dullemond 2012). Both of these scattering processes are elastic.

2.5 Radiation force

As photons are scattered or absorbed by gas and dust, there is an exchange of momentum. The rate of change of momentum is the radiation force. The force per unit volume for photons with momentum E/c is

$$\mathrm{d}f_{\mathrm{rad}} = \frac{\mathrm{d}(E_\nu/c)}{\mathrm{d}t\,\mathrm{d}V}. \qquad [\mathrm{dyn\,cm^{-3}}] \quad (2.46)$$

Combining the definition of specific intensity and the attenuation of specific intensity (equations (2.1) and (2.9) respectively), the energy transferred from the ray to the medium is

$$\mathrm{d}E_\nu = \mathrm{d}I_\nu\,\mathrm{d}\nu\,\mathrm{d}t\,\mathrm{d}A\cos\theta\,\mathrm{d}\Omega \quad (2.47)$$

$$= (k_\nu I_\nu\,\mathrm{d}s)\,\mathrm{d}\nu\,\mathrm{d}t\,\mathrm{d}A\cos\theta\,\mathrm{d}\Omega \quad (2.48)$$

$$\Rightarrow \frac{\mathrm{d}E_\nu}{\mathrm{d}t\,\mathrm{d}A\,\mathrm{d}s} = \frac{\mathrm{d}E_\nu}{\mathrm{d}t\,\mathrm{d}V} = k_\nu I_\nu \cos\theta\,\mathrm{d}\nu\,\mathrm{d}\Omega \quad (2.49)$$

for a volume element $\mathrm{d}V = \mathrm{d}A\,\mathrm{d}s$. This divided by c is just the right hand side of equation (2.46). Integrating therefore gives the total force:

$$\begin{aligned} f_{\mathrm{rad}} &= \frac{1}{c}\int k_\nu \left(\int I_\nu \cos\theta\,\mathrm{d}\Omega\right)\mathrm{d}\nu \\ &= \frac{1}{c}\int k_\nu F_\nu\,\mathrm{d}\nu \end{aligned} \quad (2.50)$$

where the final step uses the definition of the physical flux F_ν (equation 2.5).

2.6 Hydrodynamics

The Euler equations of mass, momentum and energy conservation are, respectively,

$$\frac{\partial \rho}{\partial t} + \boldsymbol{\nabla} \cdot (\rho \mathbf{u}) = 0 \tag{2.51}$$

$$\frac{\partial \rho \mathbf{u}}{\partial t} + \boldsymbol{\nabla} \cdot (\rho \mathbf{u} \otimes \mathbf{u}) = -\boldsymbol{\nabla} P - \rho \boldsymbol{\nabla} \phi + \mathbf{f}_{\text{rad}} \tag{2.52}$$

$$\frac{\partial \rho e}{\partial t} + \boldsymbol{\nabla} \cdot (\rho e \mathbf{u}) = -\boldsymbol{\nabla} \cdot (P \mathbf{u}) - \rho \mathbf{u} \cdot \boldsymbol{\nabla} \phi \tag{2.53}$$

where ρ is mass density, $\mathbf{u}$ is the flow velocity, P is the gas pressure, ϕ is the gravitational potential, and e is the total specific energy (the sum of the specific internal and kinetic energies). The last two terms in the momentum equation account for gravitational and radiation forces, respectively; the gravitational potential is given by Poisson's equation,

$$\nabla^2 \phi = 4\pi G \rho \tag{2.54}$$

while the radiative force $\mathbf{f}_{\text{rad}}$ is taken from equation (2.50).

The Euler equations express the time-evolution of the density, momentum, and energy, plus a spatial gradient of the density flux, momentum flux and energy flux, respectively. It is useful to write the equations in the generalised form

$$\frac{\partial q}{\partial t} + \boldsymbol{\nabla} \cdot \mathbf{f} = \mathbf{s} \tag{2.55}$$

for some state variable q and associated flux $\mathbf{f} = q\mathbf{u}$, with source terms contained in $\mathbf{s}$. Solving this equation using numerical methods is explored in chapter 3.

Chapter 3

Numerical methods: radiation hydrodynamics in TORUS

In this chapter I discuss how the radiation hydrodynamics concepts discussed in chapter 2 can be applied numerically, specifically in regards to TORUS, the RHD code used in the following chapters. These were implemented by others – namely, Tim Harries, Tom Haworth, Dave Acreman, Ryuichi Kurosawa, and Neil Symington – except where stated otherwise. I also describe the changes I made to TORUS to improve its computational efficiency.

3.1 Numerical hydrodynamics

Describing the variation of a fluid in time and space requires solving the Euler equations, presented in section 2.6. It is possible to solve these equations approximately by using discrete methods, which the lecture notes by Dullemond & Wang (2009) cover in detail. The approximate form of the generalised conservation equation in 1D is

$$\frac{\Delta q}{\Delta t} + \frac{\Delta f}{\Delta x} = s. \tag{3.1}$$

In an explicit integration (or forward Euler) method, the state variable at a future time, q^{n+1}, is computed in terms of the variable at the current time, q^n. If there are source terms s, this can be done using operator-splitting, such that the advection of q is computed first (i.e. $s = 0$), then the source term is added onto the result.

When $s = 0$, the new state depends on the flux coming in or going out of the cell (in a finite volume method). For a cell centred at position x_i, with neighbouring cells at x_{i-1} and x_{i+1}, the spatial derivative in equation (3.1) is computed at the cell interfaces, $x_{i-1/2}$ and $x_{i+1/2}$. The new state of the cell is given by

$$q_i^{n+1/2} = q_i^n - \Delta t \frac{f_{i+1/2}^n - f_{i-1/2}^n}{x_{i+1/2} - x_{i-1/2}} \tag{3.2}$$

where $f_{i\pm1/2}^n$ are the interface fluxes (detailed in section 3.1.1), and the time step $\Delta t = t^{n+1} - t^n$; the label $n + 1/2$ denotes that it is an intermediate step towards the final new state $n + 1$. Source terms are then computed at the intermediate stage using this result as the input. For example, in the momentum equation (equation 2.52), where $q = \rho u$ and $f = \rho u^2$, the pressure force is given by $-\,\mathrm{d}P/\mathrm{d}x$, and then

$$q_i^{n+1} = q_i^{n+1/2} - \Delta t \frac{P_{i+1/2}^{n+1/2} - P_{i-1/2}^{n+1/2}}{x_{i+1/2} - x_{i-1/2}}. \tag{3.3}$$

The time step Δt must be constrained such that q does not move more than one cell-distance in a single time step (or else information will be lost). That is, given a cell width Δx_i and velocity u_i, the longest a cell's time step can be is

$$\Delta t_i = C \frac{\Delta x_i}{u_i + c_s}. \tag{3.4}$$

This is known as the Courant–Friedrichs–Lewy (CFL) condition; the Courant number

$C = 0.6$ is a constant used for greater numerical stability; the sound speed c_s is

$$c_s = \sqrt{\frac{\partial P}{\partial \rho}} = \sqrt{\frac{P}{\rho}} \text{ (in the isothermal case).} \tag{3.5}$$

The global time step is the shortest time step on the grid, i.e. $\Delta t = \min(\{\Delta t_i\})$, and this is the value used in equations (3.2) and (3.3).

3.1.1 Fluxes

In a first-order donor-cell advection scheme, each cell has a constant q_i and the flux coming in or going out is computed at the cell interfaces. The advected quantity moves downstream with an interface flux

$$f^n_{i-1/2} = \begin{cases} = q^n_{i-1} u_{i-1/2} & (u_{i-1/2} > 0) \\ = q^n_i u_{i-1/2} & (u_{i-1/2} < 0) \end{cases} \tag{3.6}$$

where the velocity $u_{i-1/2}$ is an interpolation of the cell-centred velocities u_i and u_{i-1}. The donor-cell algorithm can be improved upon by assuming q also varies piecewise-linearly as a function of x within a cell, i.e. $q^n(x) = q^n_i + \sigma^n(x - x_i)$, where q^n_i is the average at the cell centre and σ is a slope. The full derivation of the resulting interface flux is given by Dullemond & Wang (2009), but the final result is

$$f^n_{i-1/2} = \frac{1}{2}|u_{i-1/2}|\left(1 - \left|u_{i-1/2}\frac{\Delta t}{\Delta x}\right|\right)\phi(r^n_{i-1/2})(q^n_i - q^n_{i-1}) + \begin{cases} q^n_{i-1} u_{i-1/2} & (u_{i-1/2} > 0) \\ q^n_i u_{i-1/2} & (u_{i-1/2} < 0) \end{cases} \tag{3.7}$$

where $\phi(r)$ is a flux-limiter – an example is the superbee limiter (Roe 1986; the default in TORUS), which has the form

$$\phi(r) = \max[0, \min(1, 2r), \min(2, r)] \tag{3.8}$$

with

$$r^n_{i-1/2} = \begin{cases} \frac{q^n_{i-1} - q^n_{i-2}}{q^n_i - q^n_{i-1}} & (u_{i-1/2} > 0) \\ \frac{q^n_{i+1} - q^n_i}{q^n_i - q^n_{i-1}} & (u_{i-1/2} < 0). \end{cases} \tag{3.9}$$

The flux equation (3.7) uses the cell-centred value of q_i, with information about the slope encoded in ϕ. This provides a second-order correction term when the state is updated in equation (3.2). Where there is a large gradient in q, $\phi \to 0$ and the flux reduces to first-order piecewise-constant advection. This makes the scheme Total Variation Diminishing (TVD) – the Total Variation is defined as

$$\mathrm{TV}(q) = \sum_i \left| q_i - q_{i-1} \right| \tag{3.10}$$

and the TVD condition satisfies

$$\mathrm{TV}(q^{n+1}) \leq \mathrm{TV}(q^n). \tag{3.11}$$

Piecewise-linear slopes can cause spurious oscillations to develop near sharp gradients, which increases the TV over time. However, as piecewise-constant schemes are TVD, the flux-limiter can avoid this inaccuracy near shocks and therefore equation (3.11) is satisfied.

3.1.2 Artificial viscosity

Viscosity becomes important in real shocks as kinetic energy is dissipated into heat. The scale at which this occurs is not resolved in numerical calculations of hydrodynamics, so a sub-grid model is required to mimic this diffusive effect near shock fronts. This smears out unphysical oscillations which arise due to the discontinuous nature of shock fronts, where the continuous Euler equations break down. To do this, a viscosity term Π is added

to the cell pressure according to

$$\Pi_i = \begin{cases} \frac{1}{4}\eta^2(u_{i+1} - u_{i-1})^2\rho_i & (u_{i+1} \leq u_{i-1}) \\ 0 & (u_{i+1} > u_{i-1}) \end{cases} \tag{3.12}$$

with the parameter $\eta \sim 1$ to 3. This is von Neumann-Richtmyer artificial viscosity (von Neumann & Richtmyer 1950), and takes effect near shocks.

3.1.3 Higher dimensions

The operator splitting method can be used to extend the algorithm to 2D and 3D, so that equation (3.1) becomes

$$\frac{\Delta q}{\Delta t} + \frac{\Delta f}{\Delta x} + \frac{\Delta f}{\Delta y} + \frac{\Delta f}{\Delta z} = s. \tag{3.13}$$

This is solved in a series of 1D sweeps, by first updating q in the x-direction with the y- and z- terms in equation (3.13) set to 0. The equivalent is then done for each of the y- and z-directions. For a more accurate result, half a time step is advanced in x, one time step in y, one time step in z, then finally another half-time step in x.

3.1.4 Summary

In summary, the numerical hydrodynamics algorithm described here is first-order in time and second-order in space, and uses a flux-conserving, finite-volume, forward Euler method to advect fluid from upstream cells. This was implemented in TORUS by Tim Harries and contributed to by Tom Haworth. Results of RHD calculations were published starting with Haworth & Harries (2012). Tim Harries also developed the self-gravity subroutines which solve Poisson's equation (equation 2.54) using a multigrid method and Dirichlet boundary conditions. In a radiation hydrodynamics calculation, the hydrodynamics is assumed to evolve isothermally with temperatures set by the Monte Carlo radiative transfer.

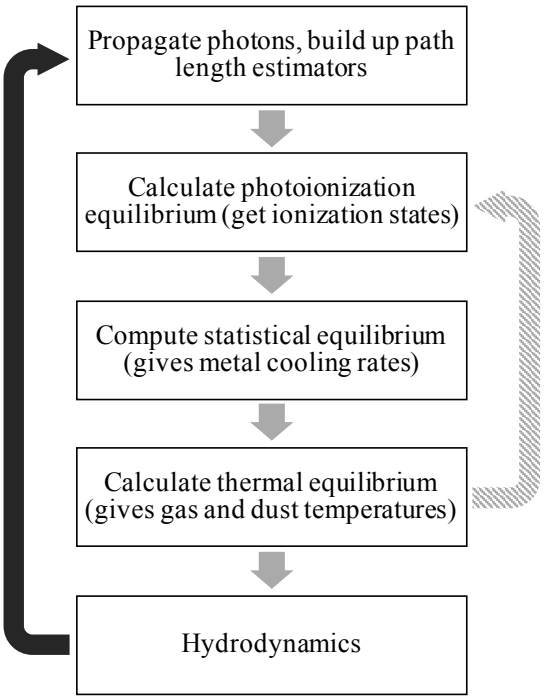

Figure 3.1: Flowchart of a radiation hydrodynamics loop. The dash-filled arrow shows recursion until convergence criteria are met.

3.2 Monte Carlo radiative transfer

As discussed in chapter 2, the interaction with radiation changes the thermal properties of gas and dust. The equation of radiative transfer encompasses the transfer of energy between the two, but the solution is difficult to obtain analytically. Monte Carlo (MC) radiative transfer (RT) is a numerical method which can converge to the correct answer, by sampling the radiation field millions of times and building up a statistical measure of the radiant energy transfer. This is the approach taken by TORUS; the steps taken in a single RHD loop are illustrated in Fig. 3.1.

In MCRT a radiation field – such as the luminosity emitted by a star – is split into discrete packets of energy and propagated through a medium. These undergo scattering or absorption events until they all escape the computational domain, by which point the total contribution of energy from the radiation field to the medium is calculated. TORUS uses the algorithm introduced by Lucy (1999) to compute radiative equilibrium, where the total rate of absorption by the medium equals that of emission. This was implemented

in TORUS, along with adaptive meshes, as part of Harries et al. (2004).

In Ali et al. (2018) I summarised this process, and I adapt that explanation here. At the beginning of a time step of duration Δt, the total stellar luminosity L is split into a total of N packets. Each packet has a total energy

$$\epsilon = \frac{L\Delta t}{N} \tag{3.14}$$

and represents a bundle of photons of a particular frequency. Packets propagate through the grid with randomly sampled path lengths ℓ between events representing absorption, scattering, or cell-boundary crossings. Each path length is randomly sampled from a probability density function (PDF) constructed from the optical depth. The PDF of a photon travelling a depth τ_ν between events in a cell is

$$p(\tau_\nu) = \mathrm{e}^{-\tau_\nu}. \tag{3.15}$$

The cumulative distribution function (CDF) is the integral of the PDF up to this depth, normalised by the total probability:

$$P(\tau_\nu) = \frac{\int_0^{\tau_\nu} \mathrm{e}^{-\tau'_\nu}\,\mathrm{d}\tau'_\nu}{\int_0^{\infty} \mathrm{e}^{-\tau'_\nu}\,\mathrm{d}\tau'_\nu} = 1 - \mathrm{e}^{-\tau_\nu} \equiv \xi \tag{3.16}$$

which lies between 0 and 1. A value of ξ is picked from a random number generator and then equation (3.16) is inverted for the optical depth,

$$\tau_\nu = -\ln\left(1 - \xi\right) \tag{3.17}$$

(Harries & Howarth 1997). This corresponds to a physical distance via

$$\tau_\nu = (k_\nu^{\mathrm{abs}} + k_\nu^{\mathrm{sca}})\ell \tag{3.18}$$

for an absorption coefficient $k_\nu^{\rm abs}$ and scattering coefficient $k_\nu^{\rm sca}$. The travelled distance is truncated if the photon would cross a cell boundary. Selecting many values of ξ samples more points of the CDF, hence more events, building up the Monte Carlo statistics (Wood 2016).

For each event, it must be determined whether the photon is being scattered or absorbed. This depends on the albedo,

$$a = \frac{k_\nu^{\rm sca}}{k_\nu^{\rm abs} + k_\nu^{\rm sca}} \tag{3.19}$$

which is the likelihood for scattering to occur. This number lies between 0 and 1, and much like before, another random number, ζ, is drawn to see whether the photon scatters. If $\zeta < a$, the photon scatters using Mie theory and a pre-tabulated phase matrix (Harries 2000). On the other hand, if $\zeta > a$, the photon gets absorbed and then re-emitted with a frequency sampled from a PDF constructed from the possible emissivities that that absorption could cause. Frequencies are interpolated between logarithmically-spaced bins; the smallest frequency bin is $\nu_1 = c/10^7$ Å, the largest is $\nu_N = c/100$ Å, and there are 1000 bins. This is how TORUS uses a polychromatic treatment for both the stellar and diffuse radiation fields.

If the photon energy exceeds the ionization potential, it can be absorbed by either gas or dust. Similar to equation (3.19), the probability for the photon to be absorbed by gas is given by

$$p = \frac{k_\nu^{\rm abs,gas}}{k_\nu^{\rm abs,gas} + k_\nu^{\rm abs,dust}}. \tag{3.20}$$

If a newly drawn random number lies below this value, emissivities are added for Lyman continuum radiation, hydrogen recombination lines, and forbidden lines from collisionally excited metals. These use calculations of statistical equilibrium to get the level populations as shown in section 2.3.5 (Symington et al. 2005).

If, however, the ionizing photon is absorbed by dust, the emissivity is given by thermal Planck emission at the cell's dust temperature T_d. All non-ionizing photons are

also absorbed and re-emitted by dust.

If each path takes a time $\delta t = \ell/c$, then for a total time step Δt the path contributes an energy $\epsilon\delta t/\Delta t = \epsilon\ell/c\Delta t$ to the radiation field. The total energy density is then

$$\mathrm{d}u_\nu = \frac{\epsilon}{cV\Delta t}\sum \ell \tag{3.21}$$

where the sum is over paths travelled between events, and this is proportional to the mean intensity J_ν via

$$\mathrm{d}u_\nu = \frac{4\pi J_\nu}{c}\,\mathrm{d}\nu \tag{2.7}$$

hence

$$J_\nu\,\mathrm{d}\nu = \frac{1}{4\pi}\frac{\epsilon}{V\Delta t}\sum \ell. \tag{3.22}$$

Once these Monte Carlo estimators are calculated, they can be used to calculate temperatures and ionization states.

A similar process to that described above can be used to produce synthetic observations (Kurosawa et al. 2004; Acreman et al. 2010). Photons can be emitted from stellar luminosities or cell emissivities, and then followed if they propagate towards a 'detector'. At the detector, the photon count is converted to a physical flux, simulating a telescope. To reduce the variance of the Poisson noise at the detector, the so-called peel-off method can be used (Yusef-Zadeh et al. 1984): if a photon packet scatters away from the line of sight, instead of being discounted, it directs a fraction of the light towards the detector (regardless of the new direction of the photon packet; recall that a photon packet represents a *collection* of real photons, not a single photon). This method is usually used to post-process an already completed RHD model, provided temperatures, densities, and ionization states are known. A self-consistent observation is one where these variables are calculated and updated as part of the RHD calculation, not as part of the observational post-processing.

3.2.1 Gas photoionization and thermal balance

In photoionization equilibrium the relative densities of successive ionization states of an element is given by equation (2.29). This can be expressed using Monte Carlo estimators by substituting for the mean intensity (equation 3.22):

$$\frac{n(X^{i+1})}{n(X^i)} = \frac{1}{n_e \alpha(X^i)} \frac{\epsilon}{V\Delta t} \sum \frac{a_\nu(X^i)\ell}{h\nu} \tag{3.23}$$

(Haworth & Harries 2012). Once this is calculated, the ionization states are fed into the statistical equilibrium calculation. This provides the cooling rates for the thermal balance. The temperature of the gas is obtained by finding the temperature which gives the total heating rate equal to the total cooling rate, using a root-finding bisection method. The cooling rates are presented in section 2.3.1. The heating rate (equation 2.23) from MCRT is

$$\Gamma(X^i) = n(X^i) \frac{\epsilon}{V\Delta t} \sum_{\nu_I}^{\infty} \frac{a_\nu(X^i)\ell}{h\nu} (h\nu - h\nu_I). \tag{3.24}$$

Once the gas temperature is found, it is fed back into the ionization balance, and this repeats until the ionization fractions and temperatures converge to within one per cent of the previous iteration's estimate.

3.2.2 Dust thermal balance

Gas and dust are thermally decoupled in this numerical scheme. The rates at which dust absorbs and emits radiant energy are given by

$$\dot{A} = 4\pi \int k_\nu J_\nu \, \mathrm{d}\nu \tag{2.41}$$

$$\dot{E} = 4\pi \int k_\nu B_\nu(T_d) \, \mathrm{d}\nu \tag{2.42}$$

equation (2.41) can be rewritten in terms of the Monte Carlo path lengths

$$\dot{A} = \frac{\epsilon}{V\Delta t} \sum k_\nu \ell. \tag{3.25}$$

The emission rate can be simplified using the Planck-mean opacity, k_P

$$k_P = \frac{\int_0^\infty k_\nu B_\nu \, \mathrm{d}\nu}{\int_0^\infty B_\nu \, \mathrm{d}\nu} = \frac{\int_0^\infty k_\nu B_\nu \, \mathrm{d}\nu}{B} \tag{3.26}$$

which leads to

$$\begin{aligned} \dot{E} &= 4\pi k_P B(T_d) \\ &= 4\pi k_P \frac{\sigma T_d^4}{\pi} \end{aligned} \tag{3.27}$$

where σ is the Stefan-Boltzmann constant. In radiative equilibrium, this can be set equal to the absorption rate such that the dust temperature is obtained from

$$T_d = \left(\frac{\dot{A}}{4\sigma k_P} \right)^{1/4}. \tag{3.28}$$

To account for gas-dust collisions, the gas and dust temperatures from the previous iteration are used in equation (2.43) to get the heat transfer rate. This rate is added onto the total dust heating rate before re-calculating T_d in the next iteration.

3.2.3 Radiation pressure

As photon packets interact inside a cell, they exchange momentum with the fluid; the net amount transferred to the fluid is the difference between the photon packet's initial momentum and its final momentum. That is, if it enters along some initial unit vector $\hat{\mathbf{u}}_{\text{in}}$ and exits along $\hat{\mathbf{u}}_{\text{out}}$, the change in momentum is

$$\Delta \mathbf{p} = \frac{\epsilon}{c\Delta t} (\hat{\mathbf{u}}_{\text{in}} - \hat{\mathbf{u}}_{\text{out}}) \tag{3.29}$$

and therefore the force exerted onto the fluid by the photon packet is

$$\mathbf{f}_{\rm rad} = \frac{\Delta \mathbf{p}}{V \Delta t}. \tag{3.30}$$

The limitation of this method is that it requires many photons to enter and exit the cell to achieve a statistically significant result (and is independent of what occurs within the cell itself). An alternative method involves using the set of equations in section 2.5, where the radiation force is

$$\mathbf{f}_{\rm rad} = \frac{1}{c} \int k_\nu \mathbf{F}_\nu \, \mathrm{d}\nu \tag{2.50}$$

which gives

$$\mathbf{f}_{\rm rad} = \frac{1}{c} \frac{\epsilon}{V \Delta t} \sum k_\nu \ell \hat{\mathbf{u}}. \tag{3.31}$$

Since this depends on the sum of all photon path lengths, ℓ, any interactions inside the cell (e.g. scattering and absorption) also contribute to the force estimator, in addition to entries and exits.

This was added by Harries (2015) and used by Harries et al. (2017) to study massive star formation in a single core. However, in practice the momentum approach is more numerically stable than the path-length method, so the models in the following chapters use equations (3.29) and (3.30).

3.2.4 FUV interstellar radiation field

The far-UV radiation field between 912 and 2400 Å can photodissociate H_2 molecules and photoexcite dust grains in real regions. The frequency-integrated mean intensity is given by

$$\begin{aligned} G_0 &= \frac{1}{H} \int_{912\,\text{Å}}^{2400\,\text{Å}} 4\pi J_\lambda \, \mathrm{d}\lambda \\ &= \frac{1}{H} \frac{\epsilon}{\Delta t V} \sum_{\lambda=912\,\text{Å}}^{2400\,\text{Å}} \ell \end{aligned} \tag{3.32}$$

(Osterbrock & Ferland 2006) specified in units of the solar neighbourhood value, $H = 1.63 \times 10^{-3}$ erg s^{-1} cm^{-2} (Habing 1968). I added this to TORUS based on a similar implementation in Bisbas et al. (2015). Although there are no molecules in the models I present in chapters 4 and 5, there are dust grains, which absorb photons at these wavelengths and re-emit thermal radiation.

3.3 Parallelisation

3.3.1 Context

A common technique in simulations of photoionization is the Strömgren volume method, where rays are cast between stars and fluid elements, and the ionization front is found by balancing the ionizing flux with recombinations. The temperature is usually set to $\sim 10^4$ K without calculating the heating and cooling rates explicitly. Such methods are used by Dale & Bonnell (2011) and Walch et al. (2012).

However, since the radiative transfer plays a crucial role in setting the dynamics of an H II region, it is necessary to calculate these parameters in a detailed and self-consistent manner – ionization will define the heating and cooling rates, which will set the temperature, which will produce a pressure, which will cause expansion. Furthermore, this is intertwined with dust microphysics, which can attenuate ionizing radiation, thus reducing the extent of the ionized volume (Haworth et al. 2015). This is normally neglected in models of H II regions.

MCRT has two significant advantages over other techniques: it can model both scattering and absorption/re-emission by both the stellar and diffuse radiation fields; and, since MC events are independent, the domain can be split up and MCRT computed in parallel over many processors. This complements the parallelisation of grid-based hydrodynamics, where fluid cannot travel more than one cell spacing.

The disadvantage in the increased parallelism is that communication is then required

to connect events between sub-domains. This is not a simple problem, as hundreds of processors may be involved in propagating tens of millions of photon packets, which together undergo billions of events. Furthermore, if events are concentrated in a particular region of the domain where it is more optically thick, some processors will do more work than others, and load-balancing becomes necessary. However, as photon packets are independent of each other, multiple copies of each sub-domain can be made, and their individual results combined at the end; this is the key point which permits the load-balancing of MCRT.

3.3.2 Message Passing Interface

In a parallel distribution method, each sub-problem is put on a single processor (or core, or thread; these terms are used interchangeably here) with its own memory, and each thread runs the same program independently. Communication between threads is facilitated by Message Passing Interface (MPI).

In a basic one-to-one MPI communication, one thread sends some data to another thread, which receives the data and stores it in its own memory. Each thread is assigned a unique number, or *rank*, within a group of threads called a *communicator*. The sending thread makes a call such as

```
call MPI_SEND(sendBuffer, count, dtype, destination, tag, comm, ierr)
```

`sendBuffer` is the variable being sent (e.g. an integer, float, array, string, etc.). `count` is the number of elements of `sendBuffer` being sent (e.g. if a single integer, `count` = 1; if sending two elements of a five-element array, `count` = 2). The data type is specified by `dtype`, equal to a standard MPI data type (e.g. `MPI_INTEGER`), or a custom declared type (e.g. `MPI_PHOTON_STACK`). The message is sent to `destination`, which is a rank number in the specified communicator, `comm`. `tag` is an integer which identifies this message, and `ierr` saves an error code after completion. On the destination thread, the corresponding receive call is

```
call MPI_RECV(recvBuffer, count, dtype, source, tag, comm, status, ierr)
```

This receives `count` number of `dtype` elements and saves into the `recvBuffer` variable. This explicitly requires a `source` thread – therefore, every `MPI_RECV` must match an `MPI_SEND`. If the exact rank number is unknown, this can be set to `MPI_ANY_SOURCE`. The `status` tag contains metadata information about the received message.

A collective communication is one where multiple threads communicate at the same time. An example is

```
call MPI_BCAST(buffer, count, dtype, source, comm, ierr)
```

which broadcasts a variable `buffer` from a `source` thread to all other threads in `comm`, who save it in their own `buffer` variable.

3.3.3 Domain decomposition

TORUS decomposes the domain of hydrodynamical models using an octree method (in 3D). The grid is split into 8 sub-domains, each of which can be split into another 8, repeating down the tree. Each sub-domain can be put onto its own processing thread, meaning the total hydrodynamics problem can be split over 8^l threads, where $l > 0$ is the number of levels on the octree; so a 3D hydrodynamics model can be split over 8, 64, or 512 threads. Since the fluid can move between adjacent sub-domains, the relevant threads are required to communicate with each other. This is achieved using MPI. An analogous method is used for grid structures in 1D (2^l) and 2D (4^l).

In a radiation calculation, the Monte Carlo photon packets need to be distributed to stars where they are 'emitted', before being propagated through the fluid and undergoing absorption/scattering events until they leave the grid. Since photon packets are independent of each other, MCRT is 'embarrassingly parallelisable' – that is, the problem can hypothetically be split across as many threads as there are events.

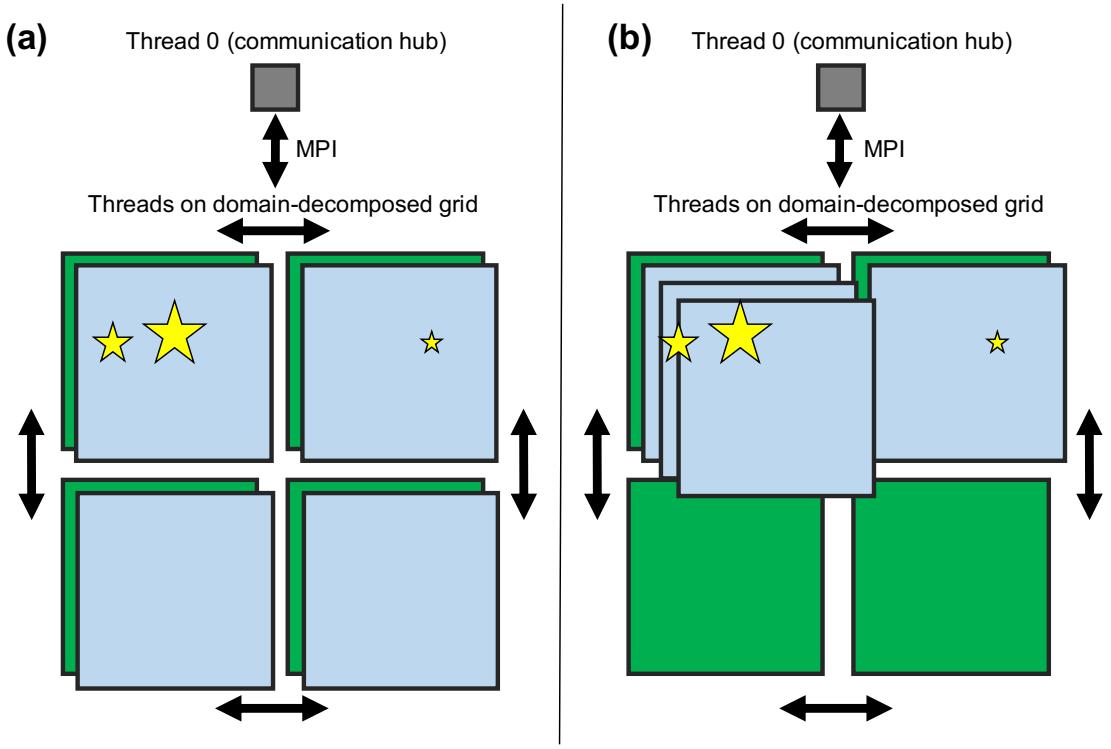

Figure 3.2: Illustration of load-balancing on a 2D grid. The grey square is the communication hub (referred to in the text as the 'zeroth thread'). Green squares represent domains ('hydrodynamics threads') and do both MCRT and hydrodynamics. Blue squares represent MCRT load-balancing threads and only do MCRT. Arrows show MPI communications. (a) Load-balancing threads are allocated evenly, for example because every domain has an equal number of cells. (b) Allocated unevenly, based on number of stars or photon events. Bigger stars have higher luminosities.

3.3.4 MCRT load-balancing

To ensure the work is distributed evenly across threads, additional threads are assigned to a particular domain (also referred to as a hydrodynamics thread) based on a weighting factor describing how much work each domain is doing. This could be the number of photon events, the number of cells, or the number of emitting sources, or the total luminosity. These load-balancing methods were added by Tim Harries and myself. The allocation of load-balancing threads to hydrodynamical domains is illustrated in Fig. 3.2.

Each method is suited for a particular purpose. For example, at the very beginning of a simulation, when no photons have yet been propagated (and therefore there are no previous events), it can be quicker to balance the load according to number of sources rather than cells, as a proxy for where photons will be experiencing events. After the

estimators have been calculated, it then becomes more efficient to use the number of events for the next photon propagation step.

However, for the photoionization and thermal balance calculation, since each cell is doing roughly the same amount of work, the load-balance weighting is chosen to be the number of cells. On a fixed grid, every domain contains the same number of cells, so the load-balancing threads are distributed equally.

At the end of each radiation step, the load-balancing threads do a collective MPI communication with the associated domain, so the Monte Carlo estimators, temperatures, and ionization states get stored on that hydrodynamics thread. The load-balancing threads get reallocated at the beginning of every MCRT step (once before the photon propagation, and once before the photoionization/thermal balance, in order to switch the weighting factor). The time taken to redistribute threads and collate information is negligible compared to the time this method saves.

3.3.5 Parallelisation of photon propagation

An additional thread is used as a communication hub during the radiation step. This is referred to as the zeroth thread, as its rank is equal to 0 in the communicators it is included in. At the beginning of each radiation step, this thread assigns information for each photon. It chooses an 'emitting' star by randomly sampling from a probability distribution function constructed from the stellar luminosities. The location of the star and the corresponding hydrodynamics thread is then identified; if this has load-balancing threads assigned to it, one is chosen from the list in a round-robin manner. This work-thread will be the one carrying out the actual MCRT algorithm.

The zeroth thread assigns a stack for each work-thread, into which it saves the photon packets. Once a stack has reached a predetermined maximum size called `maxStackLimit` (say, 200 packets in a stack), the stack is sent using `MPI_BSEND`: this saves the stack into a memory buffer of pre-allocated size on the receiving end, meaning there does not need

to be a handshake between the two threads – the zeroth thread can continue creating and sending photons; the receiving thread can continue propagating its stack of photons and, when ready, take the next stack off the memory buffer. The combined effect of the stacking procedure and the buffered send is to reduce the total communication time; the higher the `maxStackLimit`, the fewer sends that need to be made.

Whilst the zeroth thread is doing this, each work-thread waits to receive a photon stack from `MPI_ANY_SOURCE`. It goes through each photon in the stack, carrying out the MCRT routines. Photons will eventually reach the domain boundary or escape from the grid altogether. The former photons are stored in the same way as the zeroth thread – stacked by destination thread, then sent off only once `maxStackLimit` is reached. The work-thread then loops back to the beginning, waiting to receive another photon stack – this could be from the zeroth thread (i.e. freshly created stellar photons) or from other work-threads (stacks which have crossed into its domain).

Threads can pass each other signals by giving the first photon in a stack a dummy variable in the photon's destination variable (which is part of a Fortran derived type). This is a negative integer, as all legitimate destination ranks are positive. When a thread receives a stack, it first checks this variable for a signal, for example an instruction to tell the zeroth thread how many photons have escaped the grid, or to end the MCRT loop.

In the following sections, I describe the improvements I made to TORUS to improve its computational efficiency. I approached this by solving the slowest bottlenecks first, so I present them in roughly that order.

3.3.6 Random source selection

For the zeroth thread to determine which stars emit photons requires setting up probability density functions such that the most luminous stars emit the most. This is done by calling the subroutine `randomSource` with the argument `initialize=.true.` – this sets up the PDFs by integrating over the spectrum of every star. Previously, this was done for every

photon at every time step. I carried out time tests to see which parts of the MCRT algorithm were bottlenecks: using 264 threads (64 of which were hydrodynamics domains, with the rest being load-balancing), 3×10^7 photons, and a `maxStackLimit` of 100 (reasonable parameters for an RHD calculation), this took approximately 9.25 minutes, or 80 per cent of the total MCRT propagation time. Clearly, the stellar SEDs do not change from photon to photon, so the PDFs do not need to be recalculated for every one. I therefore set `initialize=.false.` for all photons bar the first, which saves the PDFs. This reduced the `randomSource` runtime to 2 seconds, or 0.5 per cent. The net effect was to reduce the runtime of a representative MCRT propagation step by half, as it then moved on to the next bottleneck.

3.3.7 Flushing mode

A work-thread could be waiting for a new stack even if other threads have collected photons to give it – this is because photons are hoarded until `maxStackLimit` is reached on the sending thread. While this is desirable early on, when photons are sure to be collated efficiently and MPI communication time is therefore minimised, this proves to be a bottleneck later in the process. Ideally, near the end, the work-threads need to be allowed to pass messages with stacks of *any* size (even of size 1). This was termed *flushing*, as threads will release any photons they have in storage, and then pass future photons one by one.

In a previous implementation of TORUS, threads started to flush too early in an MCRT calculation, with most photons being sent one-by-one between work-threads. This resulted in a large communication overhead as many threads spent the majority of their time doing large numbers of small MPI messages, and this is computationally costly.

To correct this issue, I modified the flushing-mode initiation to gauge when most of the hard work has been done, and only then to start sending photons individually. The very last photon sent out by the zeroth thread is tagged with a true `lastPhoton`

Boolean variable before being sent off to a work-thread. Once this photon escapes, the work-thread tells the zeroth thread, which immediately passes on a message to all threads telling them to flush. By this stage, most of the photons should already have escaped, with a relatively smaller number still requiring processing or sending. This method resulted in a more efficiently timed signal, as threads would stack photons for a larger portion of the calculation. The MCRT runtime was reduced from approximately 5.75 to 1.5 minutes, a speed-up by a factor of 3.5 (using the same model parameters as section 3.3.6).

3.3.8 Storing stacks of photons

In a previous version of TORUS, the zeroth thread kept an array with `maxStackLimit * nThreads` number of elements (of the order 10^4 or 10^5 for a large simulation), enough to store a full stack for every work-thread. As it initialised each photon at the beginning of the MCRT step, it stored the photon in an empty element of the array. Once the stack limit for a particular destination thread was reached, the stack was sent off, making empty spaces for new photons. These empty spaces were scattered arbitrarily, as photons were not sorted by destination thread (and the destination would change from photon to photon). This meant the zeroth thread had to loop through the array to find an empty entry before it could store something. This repetitive looping through for every photon (and there may be tens of millions of photons) caused another bottleneck.

I solved this by compartmentalising the storage array by destination thread. When a new photon is initialised, it is simply appended into the compartment for its intended destination. Once that section is full (reaching `maxStackLimit`), the stack is sent – and the entire section becomes free. In other words, the zeroth thread knows exactly where in the array to put new photons, making looping through it unnecessary.

3.3.9 Idling threads

The improved 'flushing' mode discussed in section 3.3.7 relied on the escape of the last photon sent by the zeroth thread. This was not always a reliable indicator of when most of the work was done, as that photon could be optically thin and simply stream out. This would initiate the flushing mode too early, resulting in many one-photon MPI messages. Furthermore, some threads would hang, waiting for a photon to be received, while others were busy processing theirs.

Therefore, I implemented a more robust mechanism to identify when this threshold is reached, such that the flushing mode could initiate on-the-fly for each thread depending on the activity of that thread.

I introduced a test to check if a thread is idling waiting to be sent a photon stack, and if it is, to relax the `maxStackLimit` condition. The zeroth thread repetitively sends a dummy signal photon to each thread asking how many times it has consecutively received that signal. The work thread interprets the photon as a signal, and each time increments an integer `iIdle` by 1. If the thread receives actual photons between signals, `iIdle` resets to 0. If `iIdle` reaches `nIdleMax` (nominally set to 2), this means it has done no useful work between the `nIdleMax` requests – after this point, it flushes out any photon packets it has stored up (and tells the zeroth thread to stop polling it). If it receives more photon packets later on, it sends them off as and when it can.

Once all threads have been idling with `nIdleMax` consecutive polls, the zeroth thread goes on to check how many photon packets have escaped the grid.

3.3.10 End results

These improvements relieve much of the communication overhead in highly parallelised domains, with a speed-up of a factor ~ 10 compared to the old implementation. This means it is feasible to run a radiative transfer calculation with as much detail as a dedicated RT code such as CLOUDY (Ferland et al. 2013), step by step with the hydrodynamics. Many of

the improvements were used in Harries et al. (2017) where I was a co-author. They also permitted the calculations in chapters 4 and 5, making them the first of their kind in this field.

Typical run times using the DiRAC Data Centric facility with 768 threads on 2.6 GHz Intel Xeon E5-2670 Sandy Bridge cores are: 110 s for the photon propagation step, a total of 180 s to calculate photoionization, statistical and thermal equilibria, and 130 s for the hydrodynamics step (of which 80 per cent is solving the self-gravity). This is using a uniform grid with 256^3 cells, with 3×10^7 photon packets, and a `maxStackLimit` of 150.

3.4 Comparison with other codes

In this section I lay out some of the differences between TORUS and contemporary RHD codes being used to model H II regions in clusters. An overview is provided in Table 3.1.

The photoionization calculations by Dale et al. (2012, 2013a, 2014) use SPH (Benz 1990; Monaghan 1992) with sink particles to track star (or cluster) formation and accretion. TORUS uses a fixed grid and does not self-consistently model sink particle growth; stars are placed in dense places, begin on the zero-age main sequence, and follow evolutionary tracks so they lose mass, but they do not accrete it. More detail is provided in chapter 4. Dale et al. use a ray-tracing method to calculate the Strömgren volume around sink particles with overlapping H II regions, although only stars more massive than $20\,M_\odot$ are ionizing sources. A case B recombination coefficient is used with the on-the-spot approximation, meaning the diffuse ionizing radiation field is not included. Furthermore, there is no explicit treatment of dust. In comparison, TORUS calculates both the stellar and diffuse radiation fields, uses full case A recombination, and includes scattering and absorption by dust. Radiation is emitted across ionizing and non-ionizing wavelengths ($100\,\text{Å} < \lambda < 10^7\,\text{Å}$) from all stars. Neutral gas in the Dale et al. models is treated using a barotropic equation of state which mimics heating and cooling effects at different densities. Fully ionized gas is set to 10^4 K and partially ionized gas is 10^4 K multiplied

by the ionization fraction. In TORUS, temperatures for gas and dust are found by explicitly calculating their heating and cooling rates. Dale et al. have a subgrid model for mechanical stellar wind feedback, which TORUS does not yet include.

Geen et al. (2015, 2016, 2017) use the AMR code, RAMSES-RT. This includes a diffusion method using the first-order angular moment of the equation of radiative transfer (Rosdahl et al. 2013). Like TORUS, RAMSES-RT considers ionization of both H and He, but with frequencies integrated over three bins separated by the ionization potentials of H I, He I, and He II. Non-ionizing radiation is not included and there are no dust microphysics. Although RAMSES-RT can calculate radiation pressure on gas, Geen at al. do not include this in their models. They calculate the heating due to photoionization of H and He, and the cooling rates are given by recombination, free-free emission, collisional excitation of H and He, and Compton cooling. These are computed for each of the three bins, which are much less resolved than the TORUS frequencies. Metal cooling is approximated using a constant rate below 9000 K, another constant rate above 10^5 K, and linear interpolation in between. TORUS, however, does a full statistical equilibrium calculation to find the metal cooling rate. RAMSES-RT also includes magnetic fields and SNe feedback, while TORUS does not. Like Dale et al., Geen et al. use sink particles to accrete material onto stars.

The SILCC collaboration (Walch et al. 2015; Girichidis et al. 2016; Gatto et al. 2017; Peters et al. 2017) focuses on larger regions of space, namely kpc-scale segments of a galactic disk. However, zoom-in simulations have also been carried out with volumes of the order of $(100\,\mathrm{pc})^3$ (e.g. Seifried et al. 2017). The project uses the AMR code, FLASH, and includes magnetic fields and a chemical network for H and C species, including molecules; these aspects are not present in TORUS. Ray-tracing is used to compute the column density between cells and sink particles (which accrete and represent clusters), but this does not include the diffuse radiation field. Radiation is split into four bins starting from 5.6 eV, based on whether they can cause photoelectric heating from dust, photodissociate H_2, photoionize H, and photoionize H_2 (which results in immediate recombination and dissociation). However, there is no ionization of He or metals as there is in TORUS.

Likewise, radiation pressure is not included and neither is dust scattering, although dust absorption is taken into account in the ray-tracing. Many thermal and chemical rates are used to calculate abundances and temperatures, the full details of which are given by Glover et al. (2010) and Baczynski et al. (2015).

Kim et al. (2017b, 2018) use ATHENA (Stone et al. 2008) with a fixed grid and ray-tracing. Sink particles are used to represent accreting clusters. They use two frequency bins, one for Lyman continuum and one for FUV radiation. Radiation pressure is calculated for the dust. H ionization and recombination is calculated using the on-the-spot approximation with no diffuse field, and He and metals are not included. The temperature of the ionized gas only varies with ionization fraction, with a maximum temperature of 8000 K – the heating and cooling rates are not calculated explicitly.

The simulations by Mellema et al. (2006b), Henney et al. (2009), Arthur et al. (2011), and Medina et al. (2014) use the ray-tracing code C^2-RAY (Mellema et al. 2006a) to solve the photoionization rate equations for hydrogen on a fixed grid combined with an Eulerian hydrodynamics solver. They also produce synthetic observations of recombination lines and forbidden lines; however, as they do not explicitly treat the ionization of He and metals, their ionization fractions are functions of that of H, using fits to CLOUDY models. Similarly, CLOUDY fits are used to calculate the X-ray heating rate for molecules (which is not computed in TORUS) and the FUV heating of dust grains. Cooling rates include collisionally excited lines and free-free emission.

The strengths of TORUS compared to these codes lie in the radiative transfer and dust microphysics, which include scattering and absorption, for potentially many grain compositions and size distributions. Furthermore, it calculates the diffuse radiation field and uses a polychromatic treatment with finer discretisation than the other codes. Ionization fractions are calculated for many atomic species and they all contribute to the electron density and temperature. This means synthetic observations are consistent with the properties involved in the RHD evolution. However, TORUS does not include molecular photodissociation or heating. Similarly, there is room for improvement in the gridding (as

the feedback models in chapters 4 and 5 use fixed grids), and in the formation and growth of stars; ideally, AMR should be used to refine regions where gas is gravitationally collapsing, until sink particles need to be formed. This means the direct impact of feedback on star formation (e.g. triggering) is not measured, as it is in many of the aforementioned simulations. Future goals for development in these areas are discussed in chapter 6.

Table 3.1: Overview of codes used to model photoionization feedback, as used in the cited papers (see section 3.4)

	This thesis	Dale et al. (2014)	Geen et al. (2017)	SILCC	Kim et al. (2018)	Medina et al. (2014)
	TORUS	SPH	RAMSES-RT	FLASH	ATHENA	C^2-RAY
Hydrodynamics	Fixed grid	SPH	AMR	AMR	Fixed grid	Fixed grid
RT method	MCRT	Ray	Diffusion	Ray	Ray	Ray
Ionizing radiation	✓	✓	✓	✓	✓	✓
Non-ionizing radiation	✓	×	×	FUV	FUV	FUV
Diffuse radiation	✓	×	✓	×	×	×
Ionized species	H, He, metals	H	H, He	H	H	H
Heating/cooling	✓	×	✓	✓	×	✓
Dust absorption	✓	×	×	✓	✓	For FUV
Dust scattering	✓	×	×	×	×	×
Radiation pressure	Dust, gas	×	×	×	Dust	×
Magnetic fields	×	×	✓	✓	×	×
Stellar winds	×	✓	×	✓	×	×
SNe	×	×	✓	✓	×	×
Photodissociation	×	×	×	✓	×	×
Sink accretion	×	✓	✓	✓	✓	×

Chapter 4

Feedback in a 1000 solar mass cloud

In this chapter I present work published in Ali et al. (2018), with section 4.3.1 being contributed by Tom Douglas.

4.1 Abstract

We simulate a self-gravitating, turbulent cloud of 1000 $M_\odot$ with photoionization and radiation pressure feedback from a 34 $M_\odot$ star. We use a detailed Monte Carlo radiative transfer scheme alongside the hydrodynamics to compute photoionization and thermal equilibrium with dust grains and multiple atomic species. Using these gas temperatures, dust temperatures, and ionization fractions, we produce self-consistent synthetic observations of line and continuum emission. We find that all material is dispersed from the $(15.5\,\mathrm{pc})^3$ grid within 1.6 Myr or 0.74 free-fall times. Mass exits with a peak flux of $2 \times 10^{-3}\,M_\odot\,\mathrm{yr}^{-1}$, showing efficient gas dispersal. The model without radiation pressure has a slight delay in the breakthrough of ionization, but overall its effects are negligible. 85 per cent of the volume, and 40 per cent of the mass, become ionized – dense filaments resist ionization and are swept up into spherical cores with pillars that point radially away from the ionizing star. We use free-free emission at 20 cm to estimate the production rate of ionizing photons. This is almost always underestimated: by a factor of a few at early

stages, then by orders of magnitude as mass leaves the volume. We also test the ratio of dust continuum surface brightnesses at 450 and 850 μm to probe dust temperatures. This underestimates the actual temperature by more than a factor of 2 in areas of low column density or high line-of-sight temperature dispersion; the H II region cavity is particularly prone to this discrepancy. However, the probe is accurate in dense locations such as filaments.

4.2 Introduction

Stars are formed in clusters within giant molecular clouds (GMCs), with observations in the Galaxy showing that the star formation efficiency (SFE), the fraction of the total mass in stars as opposed to gas, is a few per cent (Lada & Lada 2003). Numerical simulations of star formation tend to overestimate this proportion unless they invoke feedback mechanisms to drive down the SFE (Krumholz 2015), for example by introducing thermal feedback which can prevent fragmentation (Krumholz et al. 2007; Bate 2009) or by removing reservoirs of gas that might otherwise condense into stars. This then effects the state of the stellar cluster once gas has been fully dispersed, as the exposed cluster may expand, lose stars, or become entirely unbound, depending on the SFE and dispersal timescale (Lada et al. 1984).

Gas dispersal is thought to be driven by massive stars (of spectral type O or B and mass $> 8\,M_\odot$), since they emit ionizing radiation which heats gas to 10^4 K, increasing thermal pressure and driving expansion on length scales large enough to disrupt GMCs. The effect of ionizing feedback can be positive or negative with regards to the SFE. Elmegreen & Lada (1977) and Whitworth et al. (1994) showed using analytical arguments that the material collected together by shocks from expanding ionized gas can drive material into dense layers which then gravitationally fragments to form new stars. This is supported by numerical models of clouds irradiated by ionizing stars internally (Dale et al. 2007a) as well as externally, with Dale et al. (2007b) finding that feedback caused some

stars to form earlier compared to control runs without feedback; furthermore, it caused the formation of new stars that would not have formed without feedback. On the other hand, the same simulation also displayed negative effects, with star formation being delayed for some objects, and overall the increase in SFE was small. Similarly, simulations by Walch et al. (2013) found that although triggering was effective on small timescales, on large timescales the SFE was reduced due to the dispersal of gas. This was also supported by Geen et al. (2017), whose models showed low SFEs consistent with observations of nearby clouds in the Galaxy.

Photoionization is not the only feedback process in play, however. As photons interact with gas and dust grains they exert a radiation pressure which can change the morphology of H II regions and sculpt gas into shells (Draine 2011), or reduce the SFE by clearing cavities (Agertz et al. 2013). Massive stars also launch winds at high velocities ($> 1000\,\mathrm{km\,s^{-1}}$), shocking gas to high temperatures ($> 10^7$ K; Krumholz 2015), and this may propagate out into the surrounding ISM (Lopez et al. 2011). At the end of their lifetime, after a few Myr, massive stars explode as supernovae (SNe), injecting energy and momentum into the surroundings cleared out by feedback during the main-sequence (Yorke et al. 1989; Rogers & Pittard 2013). The relative importance of these feedback processes is still not certain. In observational studies of the H II region 30 Doradus, Lopez et al. (2011) concluded that direct radiation pressure (from stellar photons) dominated over thermal pressure from ionized gas and wind-shocked gas, as well as indirect (dust-processed) radiation pressure. In 32 other H II regions, Lopez et al. (2014) observed that the ionized gas pressure was dominant, with two regions having a similar level of indirect radiation pressure, and all had significantly lower direct radiation pressure.

Analytical and numerical models provide a way to constrain the impact of feedback and much work has been done towards this at different length scales and time scales. Whitworth (1979) and Tenorio-Tagle (1979) modelled the dispersal of ionized gas via champagne flows in 1D, and this was built upon by Yorke et al. (1989) using 2D simulations with supernovae exploding into the H II-region cavity. Models by Matzner (2002)

concluded that expanding H II regions had a greater impact than stellar winds and supernovae in driving turbulence within GMCs. Krumholz & Matzner (2009) determined that the impact of radiation pressure in the dynamics of H II regions increased with the number of massive stars and luminosity, and this requires high-surface density clouds (Fall et al. 2010). Peters et al. (2010) studied the growth of compact H II regions as protostars developed in a cluster, while Dale & Bonnell (2011) simulated larger-scale GMCs, first with ionizing feedback, then later combining with stellar winds; the latter had less of an effect on the dynamics of large clouds, but in small clouds sculpted cavities through which ionizing radiation could leak (Dale et al. 2014). Rogers & Pittard (2013) simulated stellar winds and SNe and found that dense gas was largely resistant, with energy blowing out through low-density channels. More recently, Geen et al. (2015) and Geen et al. (2016) combined photoionization with SNe, with the latter's deposition of momentum depending on the number of ionizing sources pre-SN and the extent to which they had dispersed gas.

While numerical simulations such as these provide crucial information on the dynamics of star-forming regions, they must still be analysed in the same way that observers view real clouds to properly compare simulation with observation. It is therefore necessary to produce synthetic observations from the hydrodynamical models. This is a growing field, with examples such as Kurosawa et al. (2004), who used the Monte Carlo radiative transfer (MCRT) code TORUS to produce synthetic spectral energy distributions (SEDs) and Spitzer far-infrared observations of a completed Smoothed Particle Hydrodynamics (SPH) simulation of accretion disks in a low-mass star forming region. They used this data to verify the robustness of disk identification diagnostics. Haworth et al. (2012) synthesised metal forbidden-line images to calculate electron densities and temperatures of an H II region. Similarly, Koepferl et al. (2017a) used HYPERION (Robitaille 2011) and FLUXCOMPENSATOR (Koepferl & Robitaille 2017) to extract realistic observations of dust continuum from SPH models of massive star feedback by Dale et al. (2014). This allowed the testing of diagnostics used to calculate densities, temperatures and star formation rates (Koepferl et al. 2017b,c). Models by Dale et al. (2012) were also post-processed by Hubber

et al. (2016) using MOCASSIN, another MCRT photoionization code, extracting emission lines from H, He, and metals.

The standard in modelling star forming regions has so far been to carry out a radiation hydrodynamics (RHD) calculation with a simplified radiative transfer (RT) scheme, for example ray-tracing to find the ionized Strömgren volume and setting the temperature inside to 10^4 K (e.g. Walch et al. 2012; Dale et al. 2012). Snapshots from these models are then post-processed with a more detailed RT scheme to synthesise observations. However, since radiation and dynamics are physically intertwined every step of the way – temperature changes pressure which causes motion which sets a new condition for radiation, and so on – it would be more accurate to use the detailed microphysical prescription at every timestep of the RHD calculation. The resulting parameters, such as ionization states and temperatures, can then be fed into the synthetic observation processing without having to make post-hoc assumptions. This is what I set out to do in this chapter. I describe the numerical methods in section 4.3 and set out the initial conditions in section 4.4. I present the results of the RHD model in section 4.5, discuss them in section 4.6, and show synthetic observations in section 4.7. Finally I summarise and conclude in section 4.8.

4.3 Numerical methods

This work uses the radiation hydrodynamics algorithms presented in chapters 2 and 3, so the full detail has been omitted from this chapter. In summary, these models calculate photoionization and thermal equilibria for the elemental species listed in Table 4.1. Sources of gas cooling are free–free radiation, recombination lines from H and He, and collisionally excited forbidden lines from metals. Separate dust temperatures are calculated using the Lucy (1999) algorithm. Radiation pressure is computed using momentum transfer (equation 3.30). The hydrodynamics is assumed to evolve isothermally, with temperatures set by MCRT at each step. Self-gravity is included. Mass is allowed to flow out through the simulation boundary but not in.

4.3.1 MC estimator smoothing

This section was authored by Tom Douglas, who implemented the algorithm in TORUS. In order to increase the efficiency of the Monte-Carlo estimators for the radiation field we use a scheme where each of the previous estimates are weighted according to how many time steps ago they occurred and then averaged. The weighting for each estimate of the radiation field is given by

$$w_i = \exp\left(\frac{k\Delta t}{t_{\rm rad}}\right) \tag{4.1}$$

where k is the number of time steps ago the estimate was made, Δt is the time step of the simulation and $t_{\rm rad}$ is the radiation timescale. For a sufficiently large number of previous estimates the total of the weights can be approximated to the infinite sum

$$\sum_{k=0}^{\infty} \mathrm{e}^{-ak} = \frac{\mathrm{e}^{a}}{\mathrm{e}^{a}-1} \tag{4.2}$$

$$a \equiv \frac{\Delta t}{t_{\rm rad}} \tag{4.3}$$

$$f_{\rm sum} = \sum_{k=0}^{\infty} \left(f_k \mathrm{e}^{-ak}\right) \tag{4.4}$$

Using this formulation of the weights allows us to retain all the information for all the previous radiation history as a single value (equation 4.4). In order to calculate the weighted radiation value for the next timestep from the instant estimate of that time step and the weighted sum from the previous time step, we can use the fact all the weights from the previous timestep are simply multiplied by e^{-a} to give the weights for the next time step. This allows us to calculate the new weighted radiation value using

$$f_{n,\rm weighted} = \left(f_n + \mathrm{e}^{-a} f_{\rm sum}\right) \frac{\mathrm{e}^{a}-1}{\mathrm{e}^{a}}. \tag{4.5}$$

Once this has been done $f_{\rm sum}$ is set to the new value of $f_n + \mathrm{e}^{-a} f_{\rm sum}$ for the next time step. For the value of $f_{\rm sum}$ at $t = 0$ we assume the radiation field has been static for a long time so that $f_{\rm sum} = f_0 \frac{\mathrm{e}^{a}}{\mathrm{e}^{a}-1}$.

This method gives an improved estimate of the radiation field by drawing on more information at the cost of introducing some time lag into the radiation field as it changes.

4.3.2 Stars

Stars are represented by moving Lagrangian sink particles as implemented by Harries (2015), based on Federrath et al. (2010). This implementation was used by Harries et al. (2017) to model the formation of a single massive star on sub-parsec scales. In our simulation, since we do not resolve down to these scales, we do not initiate sink accretion, but we still include the gravitational forces: stars experience the gravitational potential of the gas, and vice versa. We also solve the N-body interactions between stars. Stars begin on the zero-age main sequence (ZAMS) and follow stellar evolution tracks by Schaller et al. (1992) between 0.8 to 120 $\mathrm{M}_{\odot}$. We use the tracks of two masses, M_1, M_2, such that the initial stellar mass lies between $M_1 < M_{*,\mathrm{ini}} < M_2$. We interpolate to find the new mass at the current age in the M_1 track, repeat for the M_2 track, then interpolate between the two resulting masses, yielding the final new mass. We follow the same procedure for the luminosity, effective temperature and radius. Spectra of O-stars follow the OSTAR2002 grid of models calculated using TLUSTY by Lanz & Hubeny (2003), while later-type stars follow the models of Kurucz (1991).

4.4 Initial conditions

We carry out our simulations on a 3D grid with a uniform resolution of 256^3. This resolution is chosen such that the point of complete gas dispersal is reached within a reasonable computing wall time; we have also tested models at lower resolution with bulk grid properties (such as the total mass and ionized mass on the grid) converging at 256^3. The initial condition is a spherical cloud with a uniform-density inner core extending to half the sphere radius, with the outer half going as $r^{-1.5}$. The density outside the sphere is 1 per cent of the density at the sphere edge. These conditions are similar to other cluster

simulations such as Krumholz et al. (2011) and Howard et al. (2016). The sphere has a total mass $M_s = 1000\,\mathrm{M}_\odot$, radius $R_s = 2.66\,\mathrm{pc}$, and mean surface density $\Sigma_s = 0.01\,\mathrm{g\,cm^{-2}}$. The volume density in the inner core ($0 > r > R_s/2$) is $1.6 \times 10^{-21}\,\mathrm{g\,cm^{-3}}$ and at the outer edge ($r = R_s$) is $5.5 \times 10^{-22}\,\mathrm{g\,cm^{-3}}$. If a $34\,\mathrm{M}_\odot$ star were positioned at $r = 0$ using this initial setup, its Strömgren radius (equation 1.9) would be 0.7 pc, or about half the inner-core radius (with $Q = 7.4 \times 10^{48}\,\mathrm{s^{-1}}$ and a case B recombination coefficient).

The size of the grid is approximately six times the sphere radius at 15.5 pc, giving a resolution of 0.06 pc per cell. We impose the same random Gaussian turbulent velocity field as Bate et al. (2002), with a power spectrum $P(k) \propto k^{-4}$ for wavenumber k, such that the kinetic energy equals the gravitational potential energy, i.e. the virial parameter $\alpha_{\mathrm{vir}} \equiv 2E_{\mathrm{kin}}/E_{\mathrm{grav}} = 2$. The temperature is 10 K everywhere (for both gas and dust) until radiation sources are switched on.

We evolve the clouds under gravity and turbulence without stars up to $0.75\,\langle t_{\mathrm{ff}}\rangle$, where $\langle t_{\mathrm{ff}}\rangle = 2.17\,\mathrm{Myr}$ is the average free-fall time associated with a sphere of uniform density $\rho = 3M_s/4\pi R_s^3 = 9.4 \times 10^{-22}\,\mathrm{g\,cm^{-3}}$; this is when Krumholz et al. (2011) see a SFE of 10 per cent. At this time we randomly sample stars from a Salpeter (1955) initial mass function such that the cumulative stellar mass is 10 per cent of the cloud mass ($100\,\mathrm{M}_\odot$) and at least one massive star is present. The most massive star ($33.7\,\mathrm{M}_\odot$) is placed in the cloud's most massive clump. The other 28 stars (the next most massive being $11\,\mathrm{M}_\odot$) are placed according to a probability density function assuming a star formation rate $\dot{M}(\mathbf{r})$ at some position $\mathbf{r}$; that is, $p(\mathbf{r}) \propto \dot{M}(\mathbf{r}) \propto \rho(\mathbf{r})/t_{\mathrm{ff}} \propto \rho(\mathbf{r})^{1.5}$. The initial velocity of each star is the velocity of the gas in the cell containing the star. The initial radius, luminosity, effective temperature and ionizing photon production rate of the massive star are listed in Table 4.2. The initial distribution of stars is shown in Fig. 4.1 overlaid on top of column density. At this point, we switch on the radiation field and evolve the simulation until all the mass leaves the volume.

Elemental abundances are listed in Table 4.1, using the same values as Haworth et al. (2015). We include the first few ionized states of each element, with ionization fractions

Table 4.1: Total abundance of each element and the ionized states included in the simulation.

Element	$\log_{10}$(abundance) (rel. to H)	Ionized states
Hydrogen	0	I–II
Helium	-1	I–III
Carbon	-3.66	I–IV
Nitrogen	-4.40	I–III
Oxygen	–3.48	I–III
Neon	-4.30	I–III
Sulphur	-5.05	I–IV

Table 4.2: Initial parameters of the massive star.

Parameter	Value
Mass	$33.7\,M_\odot$
Luminosity	$1.49 \times 10^5\,L_\odot$
Radius	$7.59\,R_\odot$
Effective temperature	41 189 K
Ionizing flux ($h\nu \geq 13.6$ eV)	$7.36 \times 10^{48}\,s^{-1}$

calculated using the photoionization equilibrium equation (3.23). The total abundance of each element remains constant. We also include silicate dust grains using properties from Draine & Lee (1984) – Fig. 4.2 shows the dust absorption, scattering, and total opacities as a function of wavelength. We use a constant dust-to-gas ratio of 0.01 and follow a standard ISM power-law density distribution (Mathis et al. 1977)

$$n(a) \propto a^{-q} \tag{4.6}$$

using grain sizes a between 0.1 to 1 µm and a power-law index q of 3.5, giving a median grain size of 0.12 µm.

4.5 Results

In this section we present the results from a model with both photoionization and radiation pressure feedback, along with a model with just photoionization (i.e. $\mathbf{f}_{\rm rad}$ in equation (2.52) is set to zero).

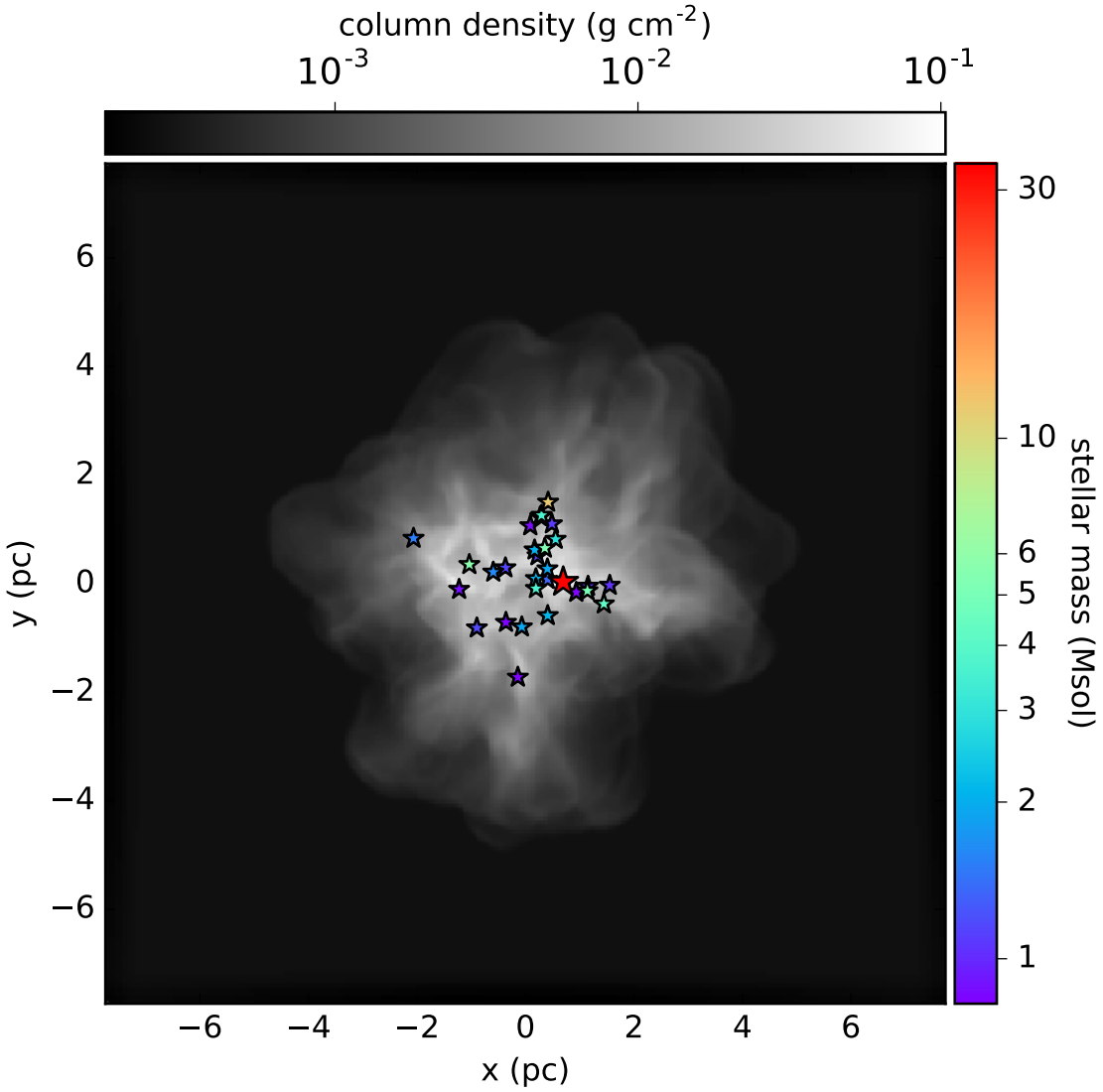

Figure 4.1: Positions of stars at the onset of feedback, with stellar mass in colour scale, overlaid on column density in greyscale (both are logarithmic). The most massive star is 33.7 $M_\odot$ in red. The second highest is 11.3 $M_\odot$. The third is 5.7 $M_\odot$. The least massive is 0.82 $M_\odot$.

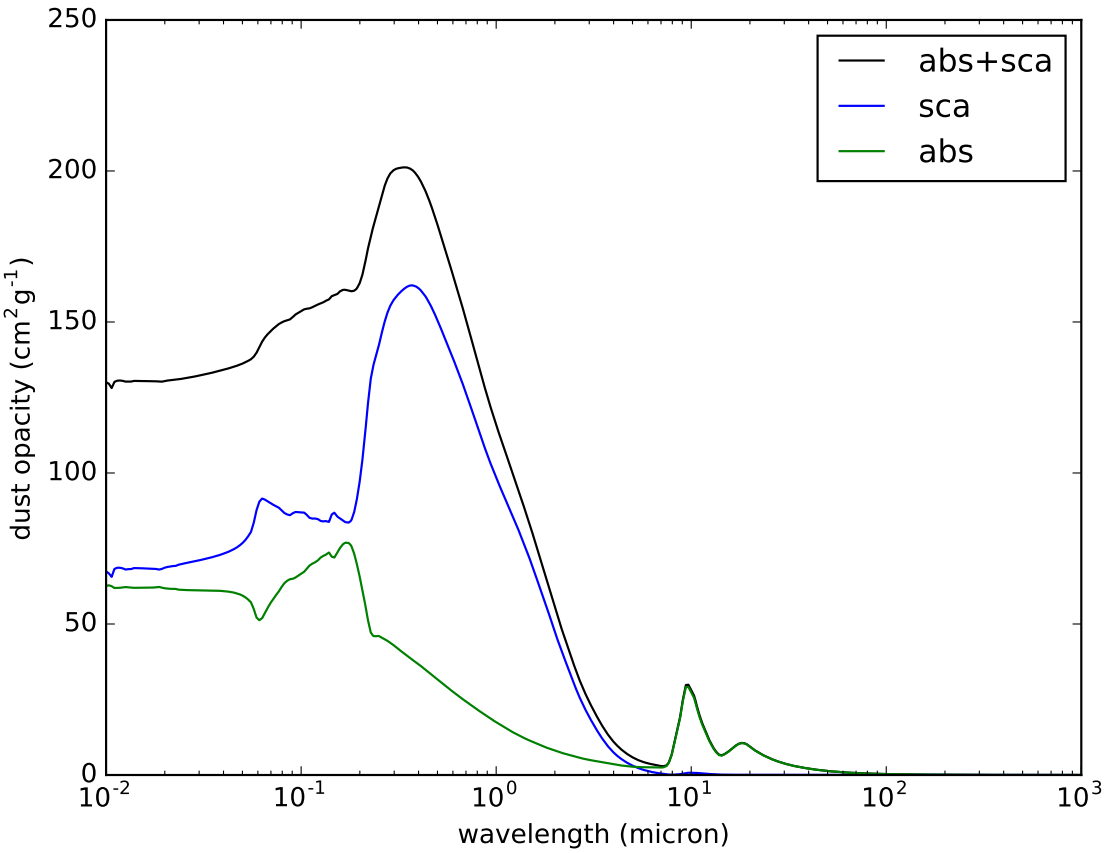

Figure 4.2: Dust opacity per unit mass as a function of wavelength showing scattering, absorption, and total opacities.

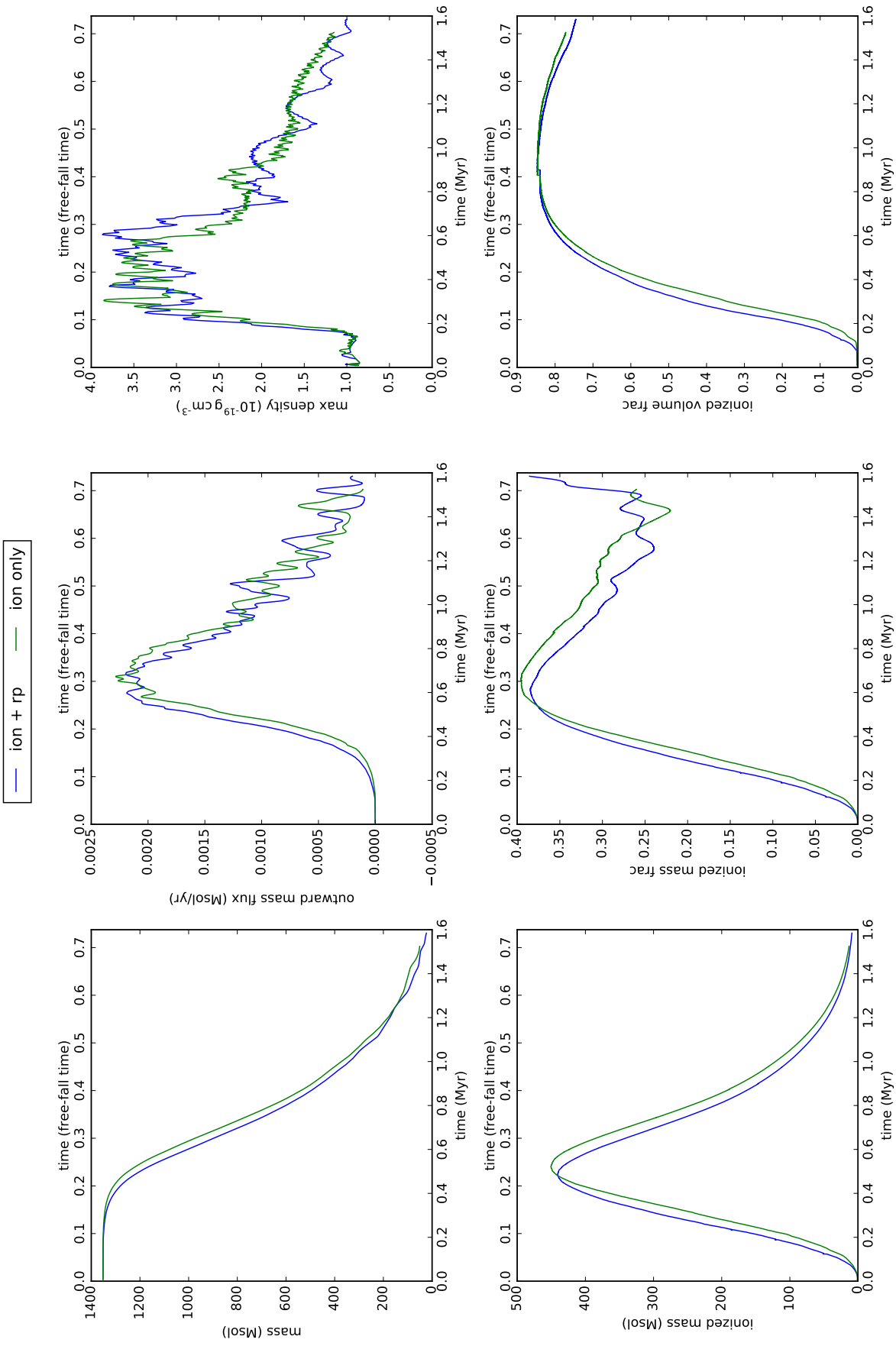

Figure 4.3: Bulk grid properties as a function of time, showing total mass, mass flux off the grid, maximum mass volume density, ionized mass fraction, and ionized volume fraction. The blue line is the model with ionization and radiation pressure; the green line is only ionization. $t = 0$ corresponds to the onset of feedback.

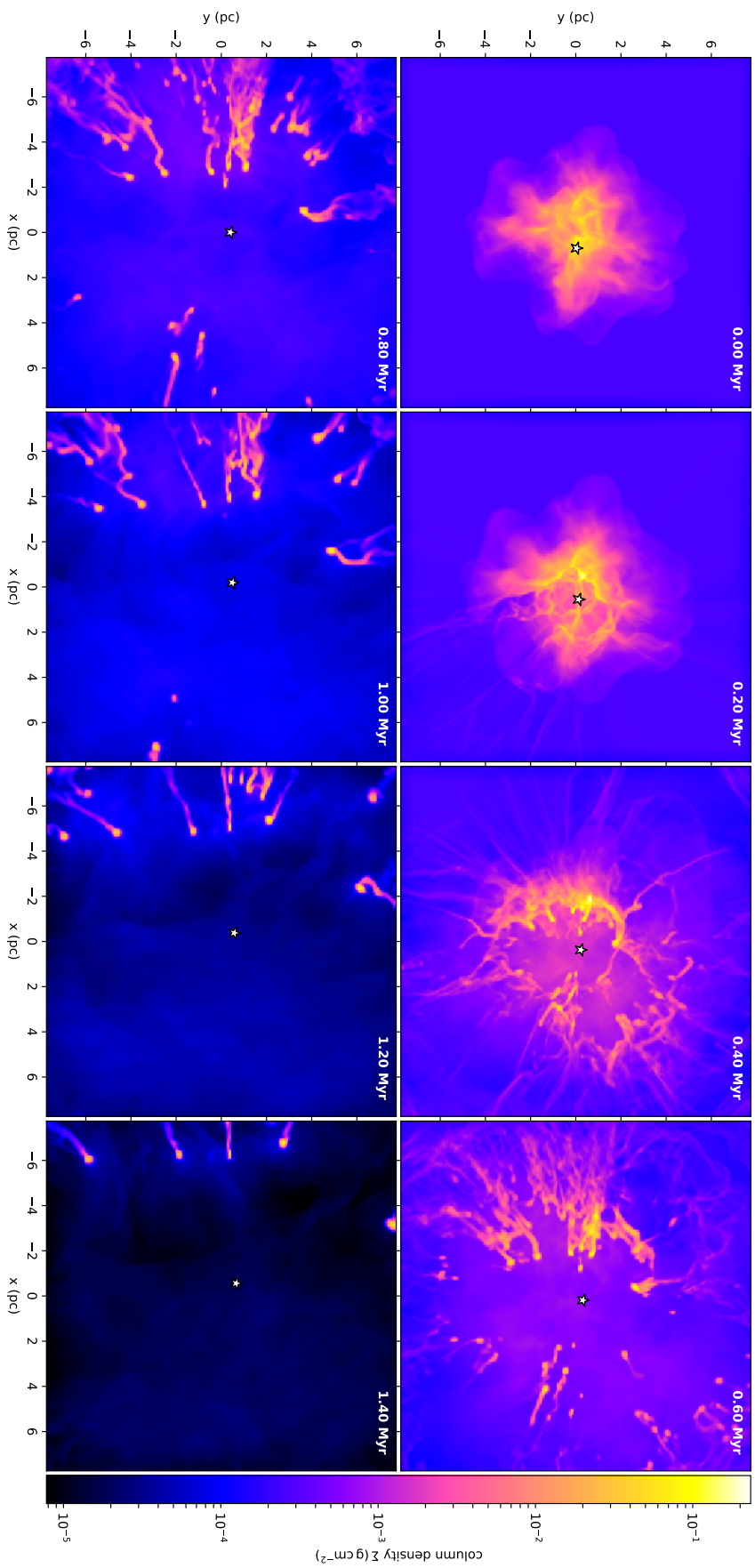

Figure 4.4: Column density integrated along the z-axis at 0.2 Myr intervals in the combined feedback model. Each frame is 15.5 pc a side. The 34 $M_\odot$ star is indicated with a point near the centre of each frame. $t = 0$ corresponds to the onset of feedback.

4.5.1 Bulk grid properties

In Fig. 4.3 we plot as a function of time the total mass on grid, mass flux off the grid, maximum density, ionized mass and mass fraction, and ionized volume fraction. Fig. 4.4 shows column density at 0.2 Myr snapshots.

The peak mass flux off the grid is $2 \times 10^{-3}\,\mathrm{M_\odot\,yr^{-1}}$, reached 0.6 Myr after initiating feedback – this is the ionized sound-crossing time from the centre of the grid to the boundary. From the onset of feedback ($t = 0$) to 0.6 Myr, the mass flow is steady, with low-density ionized gas streaming through the channels carved out of the high-density filaments by the expanding ionization front. The envelope of diffuse gas outside of the initial cloud is also pushed outwards by the expanding gas. The right half of the cluster (in Fig. 4.4) is dispersed more quickly than the left half, which contains higher-density structures and is therefore more resistant to destruction and dispersal. They remain on the grid and close to their initial positions, but the ionization front creates holes in low-density areas, and curves around high-density areas, creating clumps with tails pointing away from the ionizing star. These objects move radially away from the massive star due to the rocket effect caused by photoevaporation along their star-side edges (as in e.g. Bertoldi & McKee 1990; Mellema et al. 1998). They approach the edge of the volume over the course of the simulation with an average speed $\approx 6\,\mathrm{km\,s^{-1}}$. After 0.6 Myr the overall mass flux begins to decrease but contains spikes corresponding to the removal of the clumps. The size of the spikes grows with time, as the densest clumps are the last to leave the grid. By about 1.6 Myr, or 0.74 $\langle t_{\mathrm{ff}} \rangle$, all the mass has left the $(15.5\,\mathrm{pc})^3$ volume.

The third panel of Fig. 4.3 shows the maximum density in $\mathrm{g\,cm^{-3}}$ as a function of time. This peaks at just under $4 \times 10^{-19}\,\mathrm{g\,cm^{-3}}$ at 0.6 Myr. Between 0.2 and 0.6 Myr are when the densities become highest, as the expansion of the H II region drives material together. In the first 0.2 Myr, as gas gets ionized, the dense core containing the massive star expands spherically outwards, colliding with another set of dense filaments nearby ($\approx 10^{-19}\,\mathrm{g\,cm^{-3}}$; at $(x, y) \approx (-1, 0)$ pc in Fig. 4.4, which shows column density). Between

0.2 and 0.4 Myr the outflung material sweeps across the filament, with the densest areas remaining more stationary ($\sim 3\,\mathrm{km\,s^{-1}}$) while the lower-density gas is carried along with the flow ($\sim 10\,\mathrm{km\,s^{-1}}$). During this process, the filament is compressed and material that is initially perpendicular to the expanding shell is broken up and carved into pillars oriented parallel to the flow, ending up as tails behind spherical cores (pointing radially away from the ionizing star). Compression of the filament causes the maximum density to increase, reaching its highest value of $4 \times 10^{-19}\,\mathrm{g\,cm^{-3}}$ at 0.6 Myr. Once the expanding material has passed through and the pillars are formed, the densest cores are more exposed to the stellar radiation field and there is less collisional compression – photoevaporation removes material from the clumps, parts of the pillars break off into separate chunks, and the maximum density falls.

The fourth and fifth panels of Fig. 4.3 show the total ionized mass and the ionized mass fraction, respectively. The highest value of ionized mass is $440\,\mathrm{M_\odot}$ at 0.5 Myr (36 per cent of the total mass). The peak ionized mass fraction is reached 0.1 Myr later, still just under 40 per cent of the total mass. This is despite 85 per cent of the volume being ionized (sixth panel of Fig. 4.3), showing that most of the mass remains in small, dense clumps which resist ionization.

The photoionization-only model is mostly similar to the model with both photoionization and radiation pressure, but there are a few minor differences. The bulk effect of feedback is delayed in the photoionization-only model, with the peak in the ionized mass fraction being reached 0.03 Myr later. The later breakout of ionization results in a slightly different distribution of gas, as it has had more time to evolve under gravity and turbulence, so the total amount of gas being ionized is affected (very marginally) – the peak ionized mass fraction is about 2 per cent higher. The removal of gas from the grid also occurs with the same delay. Overall, the differences are negligible.

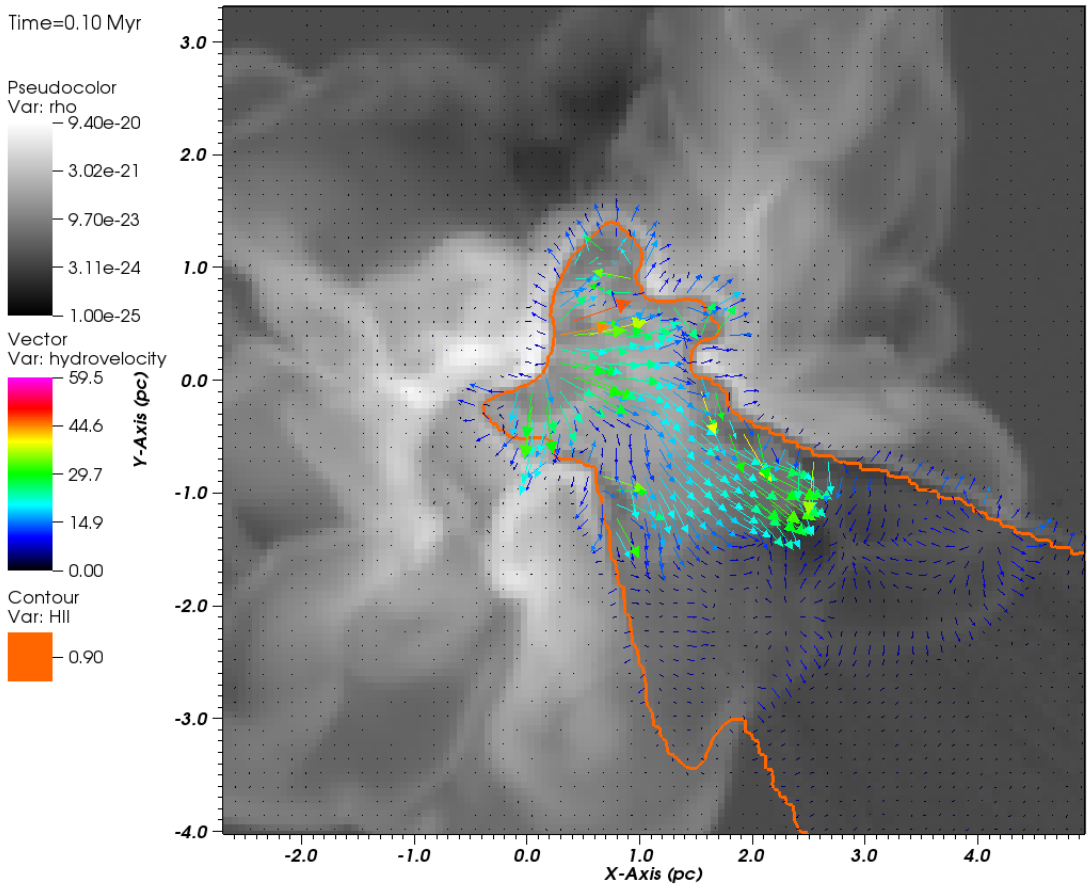

Figure 4.5: Zoomed-in slice in the xy plane at 0.1 Myr showing mass density in greyscale between 10^{-25} and 9.4×10^{-20} g cm^{-3}; vectors with size and colour corresponding to velocity between 0 and 60 km s^{-1}; and a contour where the ionization fraction is 0.9. The 33.7 $M_\odot$ star is at position $(x, y) = (0.6, 0.1)$ pc. This model includes ionization and radiation pressure.

4.5.2 Morphology

Snapshots of column density in Fig. 4.4 show how the destruction of the cloud proceeds via the expansion of ionized gas over the course of 1.6 Myr in the model containing both photoionization and radiation pressure. Fig. 4.5 shows a 2D slice of mass density and velocity vectors at 0.1 Myr. Most of the H II region is confined at 0.1 Myr by high-density filaments, but a champagne flow breaks out through the low-density region on the edge of the cloud on the opposite side. At the boundaries of the H II region, the gas travels outwards at the ionized sound speed (approximately $12\,\mathrm{km\,s^{-1}}$), while the photoevaporation of gas on the inside of the boundary leads to outflows moving inwards and then out through the champagne flow at velocities of 20 to $30\,\mathrm{km\,s^{-1}}$, with a few cells around $40\,\mathrm{km\,s^{-1}}$.

The H II region is able to break through some parts of the filament (e.g. near $(x, y) = (0.8, 1.4)$ pc in Fig. 4.5), while curving around nodes such as $(x, y) = (0.1, 0.1)$ pc which resist photoionization and are carved into globules and pillars by the expanding ionization front. The densest clumps shield material that is downwind of the ionizing source as seen in Fig. 4.6, which shows the ionization fraction of hydrogen at 0.6 Myr. Some of the shielding is only partial, for example at $(-4, 1.5)$ pc of that frame, as the diffuse radiation field ionizes gas behind the clump but to a lesser degree. This highlights the importance of including the diffuse field in RHD models.

Fig. 4.7 shows column density histograms for the combined feedback model at 0.2 Myr intervals. The spike at $t = 0$ (the onset of feedback) at $\Sigma \approx 3 \times 10^{-4}\,\mathrm{g\,cm^{-2}}$ corresponds to the stationary gas outside around the gravoturbulent cloud, which is only perturbed when the star photoionizes it or cloud material expands into it, at which point the surrounding density increases. Overall, as the simulation evolves, the PDF shifts towards lower densities, as a result of the H II region expansion and the increase in low-density, ionized material. The early high-density hump at $\approx$ a few $10^{-2}\,\mathrm{g\,cm^{-2}}$, produced during the initial starless collapse phase, is flattened out in the first 0.4 Myr. Although higher densities are achieved up to the same period, they are not long-lived, as the maximum

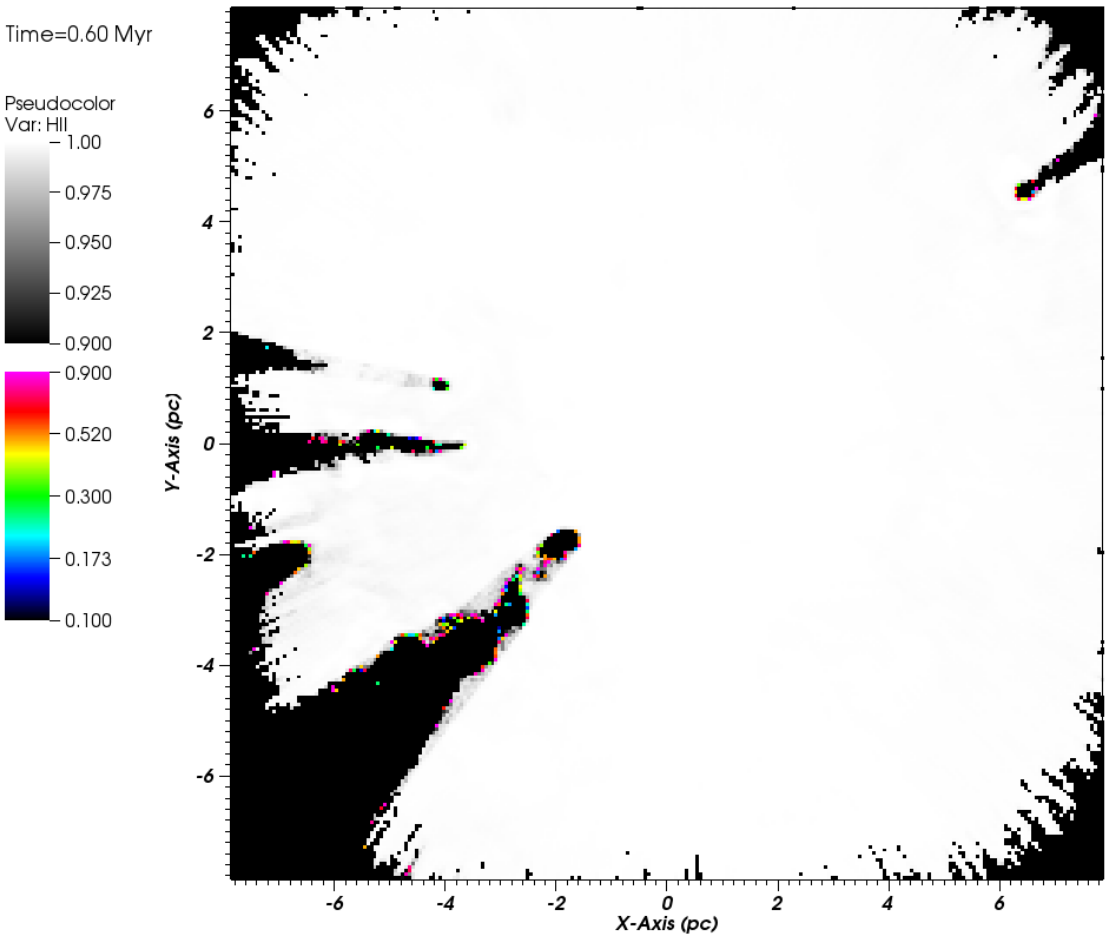

Figure 4.6: 2D slice in the xy plane at 0.6 Myr showing the hydrogen ionization fraction. The linear greyscale is the fraction between 0.9 and 1 (fully ionized gas). The logarithmic colour scale is the fraction between 0.1 and 0.9 (essentially fully neutral to partially ionized). The densest clumps and pillars are neutral but have partially ionized edges. The interior is fully ionized.

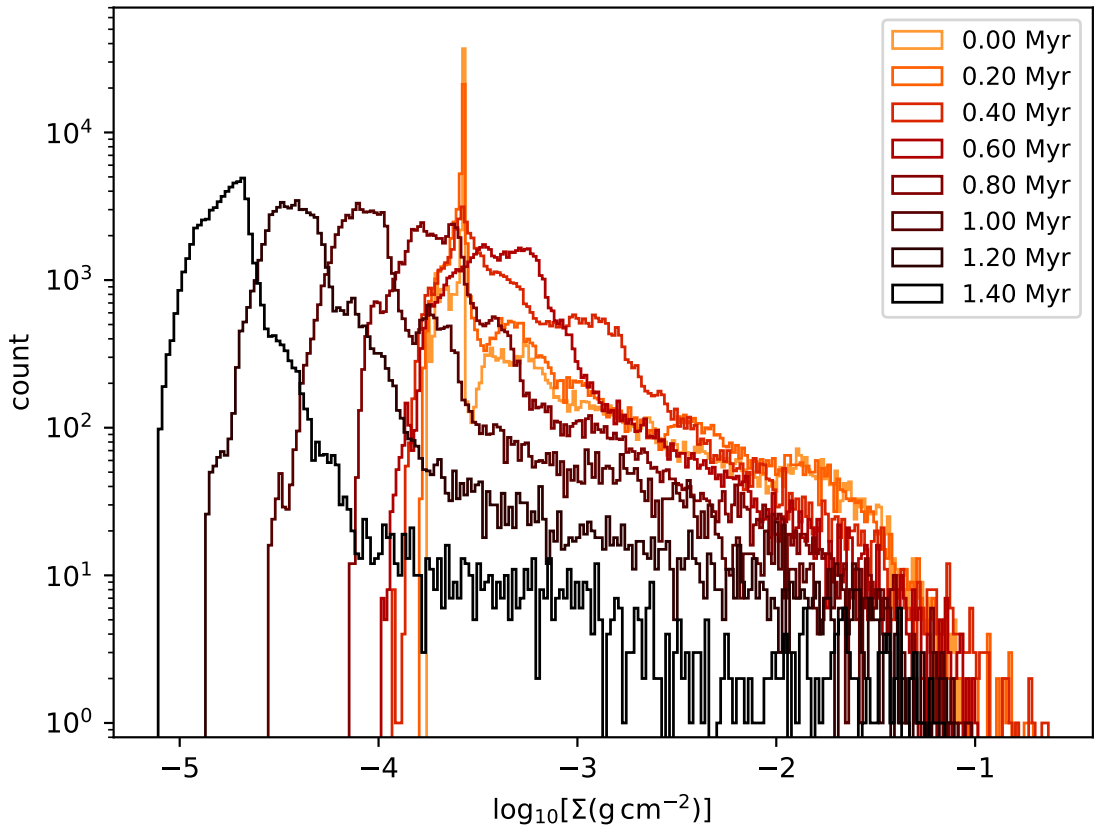

Figure 4.7: Column density histograms at 0.2 Myr intervals for the combined feedback model. Histograms shift towards lower densities as time progresses. The spike at $t = 0$ (the onset of feedback) corresponds to the stationary, uniform-density material outside the turbulent cloud.

density is reduced after another 0.2 Myr.

4.5.3 Electron temperature and density

In order to gauge the temperature of the ionized gas, we calculate weighted averages over the volume using

$$T_0 = \frac{\int wT \, \mathrm{d}V}{\int w \, \mathrm{d}V} = \frac{\sum_i w_i T_i \Delta V}{\sum_i w_i \Delta V} \tag{4.7}$$

where T_i is the temperature of cell i with volume ΔV, and we consider two different weights w: (a) $w = n_e(n_{\mathrm{H\,II}} + n_{\mathrm{He\,II}})$ as per Rubin (1968), which is well approximated by $w \approx n_e^2$; (b) mass $w = \rho \Delta V$ if hydrogen in the cell is more than 90 per cent ionized or $w = 0$ if less. In Fig. 4.8 we plot the volume-average temperature as a function of time.

The mass-weighted average temperature is highest at 0.2 Myr having a value 9300 K whilst the ionization front is still largely contained inside the cloud, but then decreases to 8000 K over the next 1.4 Myr. The n_e^2-average is 9000 K over the whole duration. The standard deviation is about 10 per cent for the n_e^2 average and is steady until about 1 Myr, at which point the deviation rises, with greater fluctuation, towards 14 per cent. The mass-weighted average also has an standard deviation around 10 per cent, but after 0.4 Myr this drops to 6 per cent and is much more steady than the electron density-weighted average. This is due to the high-mass globules and filaments which are neutral (and hence don't contribute to either average) but whose edges are partially ionized (so they do contribute to the electron density-weighted average but not the mass-weighted average). This is visualised in Fig. 4.6 where the greyscale denotes cells which are more than 90 per cent ionized, and the colour scale shows cells which are less. Since the interaction of the ionization front and the dense, neutral gas changes relatively quickly over time, the spatial extent and degree of partial ionization similarly changes, giving rise to the fluctuation in the n_e^2 average.

Fig. 4.9 shows the (unweighted) volume-average electron density in gas which is more than 90 per cent ionized. This reaches a maximum of 30 cm^{-3} at $\approx$ 0.1 Myr before

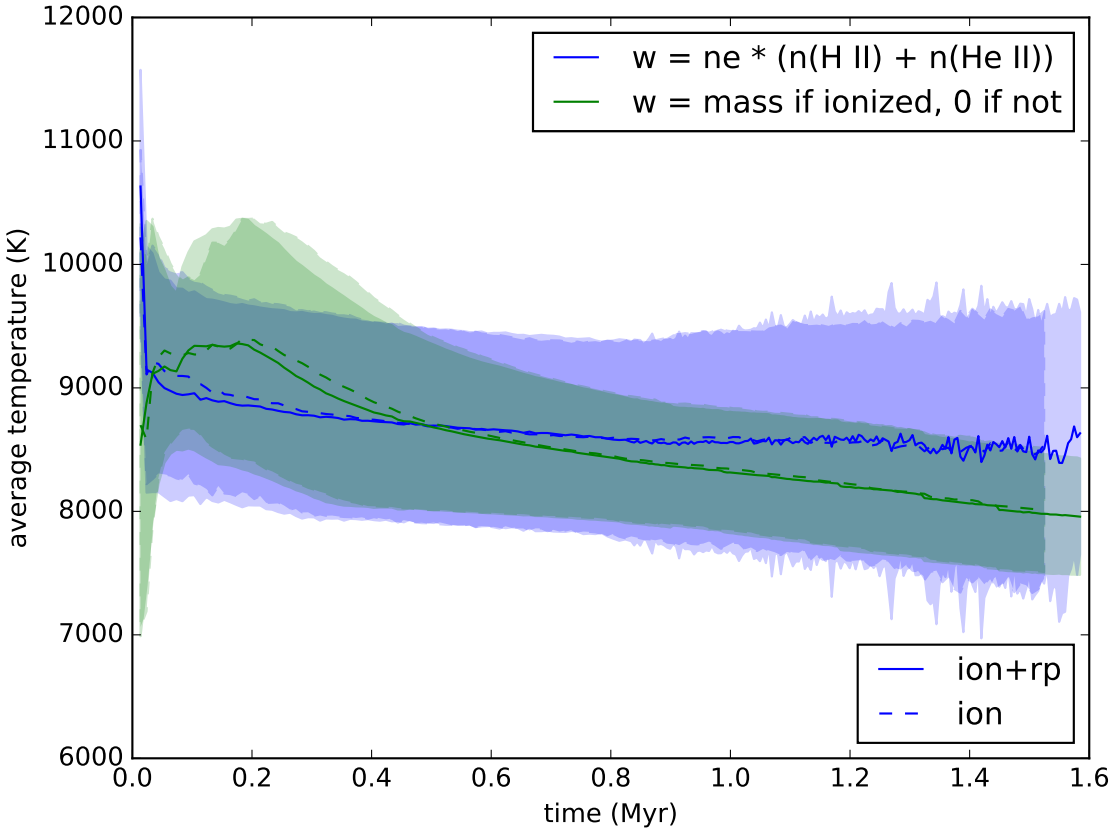

Figure 4.8: Volume-average gas temperature (with filled boundaries showing the standard deviation), plotted against time. The average is weighted by $w = n_e(n_{\mathrm{H\,II}} + n_{\mathrm{He\,II}}) \approx n_e^2$ (blue), mass $w = \rho\Delta V$ if the cell is more than 90 per cent ionized or $w = 0$ if less (green). Solid lines are the model with ionization and radiation pressure; dashed lines are the model with just ionization.

dropping down to $8\,\mathrm{cm}^{-3}$ by 0.2 Myr. It remains at this value until 0.5 Myr. As the gas flows off the grid over the next Myr the density decreases once again, reaching $0.2\,\mathrm{cm}^{-3}$ by the end of the simulation.

4.5.4 FUV interstellar radiation field

Fig. 4.10 shows a representative 2D slice of G_0, the FUV flux (equation (3.32)), in the plane of the $34\,\mathrm{M}_\odot$ star, showing the variation with distance at $t = 0.4$ Myr. The flux decreases as $r^{-2}\mathrm{e}^{-\tau}$ due to geometrical dilution and the optical depth τ, as in Bisbas et al. (2015), with shadowed cones caused by dense, dusty clumps which shield the downstream material from the stellar radiation field. The maximum value is of the order 10^6 in the cell containing the star, with values of order 10^5 in adjacent cells. In Fig. 4.11, we plot

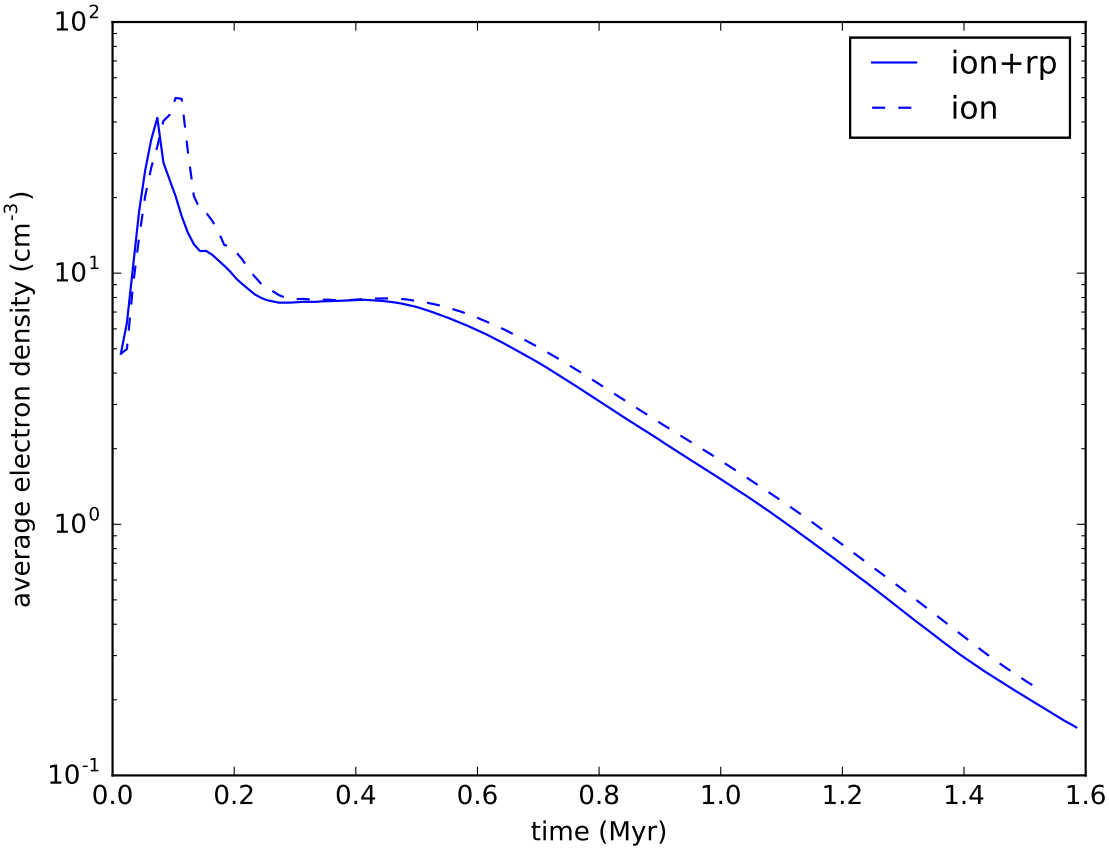

Figure 4.9: Volume-average electron density n_e in the ionized gas, plotted against time. Solid lines are the model with ionization and radiation pressure; dashed lines are the model with just ionization.

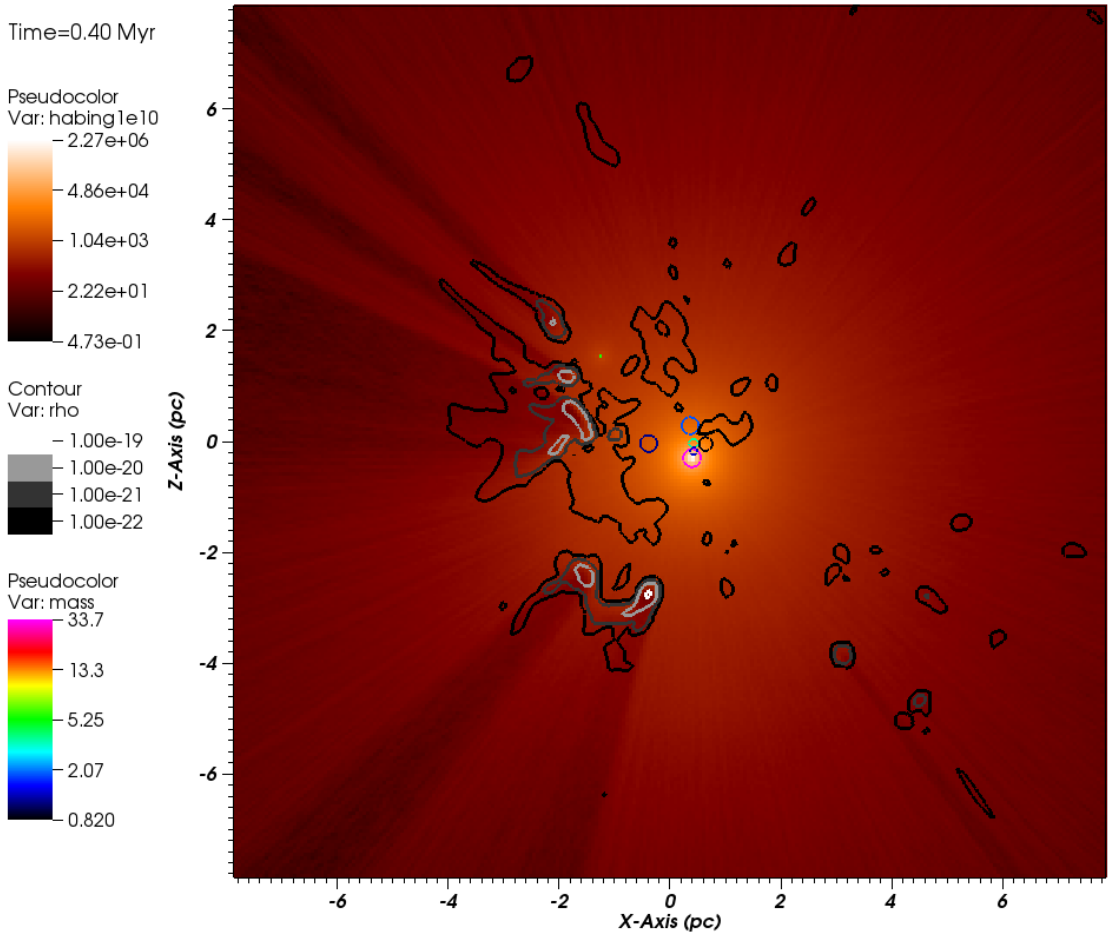

Figure 4.10: Interstellar FUV flux G_0 in units of the Habing flux (1.63×10^{-3} erg s^{-1} cm^{-2}). This is a slice in the xz plane at 0.4 Myr, taken through the position of the most massive star (pink circle, 34 $M_\odot$). Stars are plotted as 3D surfaces with a radius of 2.5 grid cells, therefore intersections of the slice with star surfaces result in circles (rainbow colour scale, with the size corresponding to the proximity to the slice). Grayscale contours show mass volume density at levels of 10^{-19}, 10^{-20}, 10^{-21}, 10^{-22} g cm^{-3}.

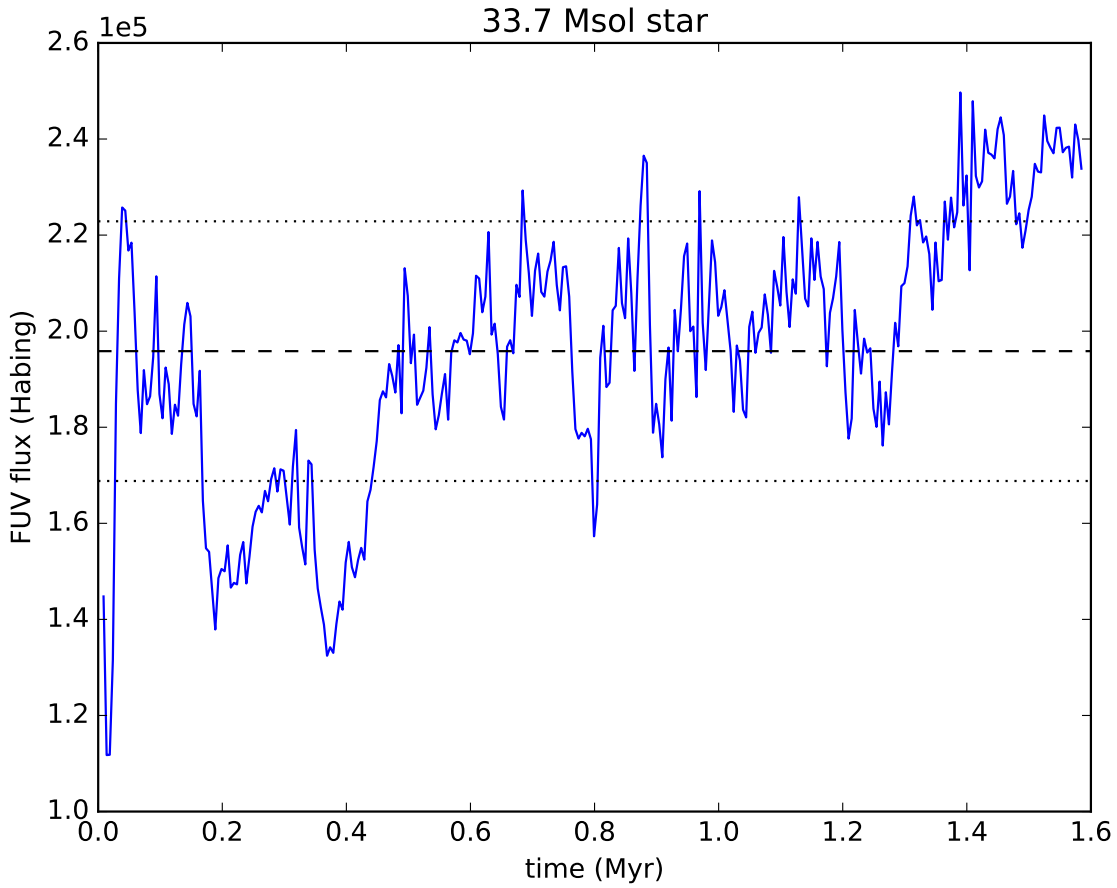

Figure 4.11: Interstellar FUV flux G_0 in units of the Habing flux (1.63×10^{-3} erg s^{-1} cm^{-2}), at the location of the most massive star, as a function of time. This is the mass-weighted average within a radius of 2.5 grid cells (0.15 pc) around the star. The horizontal dashed black line shows the time-average flux and the dotted lines show the standard deviation.

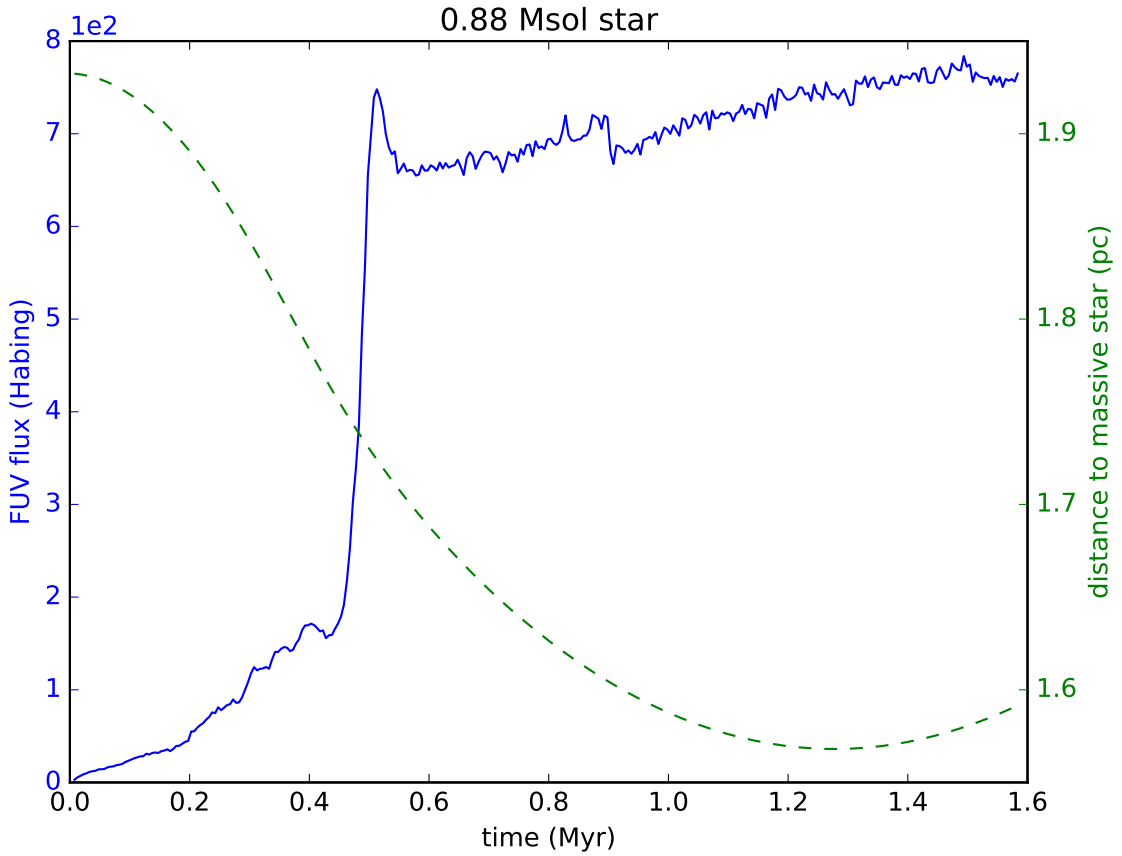

Figure 4.12: Left axis, solid blue line – interstellar FUV flux G_0 in units of the Habing flux (1.63×10^{-3} erg s^{-1} cm^{-2}), at the location of a 0.88 $M_\odot$ star, as a function of time. This is the mass-weighted average within a radius of 2.5 grid cells (0.15 pc) around the star. Right axis, dashed green line – distance to the most massive star (33.7 $M_\odot$) in pc. The rapid increase in flux at 0.5 Myr is caused by the sudden exposure to the radiation field of the most massive star as material gets removed from the smaller star's surroundings.

as a function of time the average G_0 inside a radius of 2.5 cells (0.15 pc) around the star, weighted by mass. Averaging over time, this is $(2.0 \pm 0.3) \times 10^5$ in units of the Habing flux. Fluctuations arise from the star moving between cells which have different densities and therefore different optical depths. The inner Orion Nebula is observed to have values around 4×10^5 (Osterbrock & Ferland 2006) which is comparable in magnitude to the region we model here.

We include a similar plot for a $0.88\,M_\odot$ star. This is shown in Fig. 4.12 alongside the time-varying distance to the massive star. Between 0 and 0.5 Myr, G_0 rises steadily to a value of 2×10^2, before jumping up by more than a factor of 3.5 within ≈ 50 kyr. This occurs because it is located inside a pillar which is being photoevaporated and pushed away from the ionizing source, decreasing the column density between the two stars; once it becomes completely exposed to the radiation field of the brightest source, the flux rapidly rises. After this point, G_0 remains relatively level up to the end of the simulation as the intervening material is diffuse, with a slight increase as the stars approach each other.

4.6 Discussion of the RHD model

4.6.1 Dynamics

The differences between the model with both ionization and radiation pressure, and the model with just ionization, are negligible, leading to the conclusion that photoionization is a more important process than radiation pressure for the dispersal of gas in the conditions presented here. According to Draine (2011) the latter process is expected to have a more significant role in higher-density clouds, e.g. $n > 100\,\mathrm{cm}^{-3}$ with a star having the same Lyman continuum photon flux as our model ($\approx 10^{49}\,\mathrm{s}^{-1}$).

Gas dispersal is more pronounced than in simulations by Rogers & Pittard (2013), who modelled stellar winds and supernovae feedback in a cloud with similar density but slightly higher mass ($3240\,M_\odot$), containing three massive stars between 28 to $35\,M_\odot$.

During the main sequence phase, the mass flux does not exceed $5 \times 10^{-4}\,M_\odot\,yr^{-1}$, or a quarter of the peak flux in our model. Although their grid is twice the size of ours, meaning material must travel further to leave the grid, the mass flux is relatively uniform over the first 4 Myr, with fluxes only increasing after the evolved Wolf-Rayet and supernova phases; fluxes higher than $2 \times 10^{-3}\,M_\odot\,yr^{-1}$ are only achieved after this point. This implies photoionization is a more efficient feedback mechanism for dispersing clouds than stellar winds, and is more comparable to SNe, lending support to Matzner (2002) who concluded that H II region expansion is the dominant source of feedback in GMCs. Rogers & Pittard (2013) found that dense gas was largely unaffected by feedback, with winds dispersing through low-density channels from the initial conditions. The resilience of dense gas was also found by Dale et al. (2012). This is borne out by our model as well.

The early hydrodynamical models of champagne flows in 1D and 2D by e.g. Tenorio-Tagle (1979), Bodenheimer et al. (1979) and Yorke et al. (1989) – of an ionizing O star located next to the interior boundary of a molecular cloud – show the same characteristics as our 3D model presented here (see Fig. 4.5): the ionized cloud gas escapes as a champagne flow at $30\,km\,s^{-1}$ while the diffuse ionized gas outside of the cloud expands at $10\,km\,s^{-1}$. Such velocities are also observed in real H II regions such as the Orion Nebula (M42; O'Dell et al. 2017), DR 21 (Immer et al. 2014), and the Hourglass in M8 (Chakraborty & Anandarao 1997). The schematic in Figure 4 of O'Dell et al. (2009), interpreting observations of the Orion Nebula, is remarkably similar to the champagne flow we see in Fig. 4.5, including the supersonic gas travelling away from the massive star, as well as the ionization front stalling at dense cores, from which photoevaporated material flows back towards the ionizing source.

The structures produced in our model are likely to be a result of the initial conditions. Walch et al. (2013) found similar structures in simulations where the initial conditions were filamentary and had high fractal-dimension, whereas spherical H II regions arose from conditions with lower fractal dimensions and more spherical geometries. Dale & Bonnell (2011) note that accretion flows towards deeply embedded massive stars limit the

expansion of H II regions, and therefore molecular clouds with such stellar distributions remain relatively undisturbed by feedback. On the other hand, when massive stars are located closer to the edge of molecular clouds, such as in the Orion Nebula, their H II regions may disperse gas effectively via champagne flows (Henney et al. 2005). In our model, the massive star is located deep within the cloud but it is still able to blow out a champagne flow through nearby low-density channels. Once the flow breaks out, the expanding H II region is able to disrupt and disperse the rest of the cloud – even if the starting position was dense and more resistant.

One of the limitations of our model is that stars are placed in a particular location instead of being formed self-consistently via accretion; the star is positioned fully-formed in a node between several filaments after the initial self-gravitating, turbulent evolution of the cloud. Therefore we also do not model the evolution of an ultracompact H II region alongside the growth of the star and the possible feedback effects this may incur. However, models by Peters et al. (2010) of massive protostars at the sub-parsec scale show that ultracompact H II regions 'flicker' while the star is still accreting and only grow to substantial sizes after mass reservoirs are depleted. Therefore, as an approximation for scales of a few to 10 pc, a significant H II region only blows out into the cloud once the star reaches its final mass, which is the stage we start with in our model. Furthermore, our calculation is informative for how the gas is displaced *after* this stage, and allows us to compare with, for example, models of stellar winds by Rogers & Pittard (2013) who place three massive stars in the centre of a turbulent medium. That said, for more comprehensive and self-consistent simulations we plan to use sink particles to self-consistently grow star- or cluster-particles, using subgrid models to compensate for the limited spatial resolution.

4.6.2 Temperature

The volume-average ionized gas temperature is approximately (9000 ± 1000) K over the course of the simulation. M42 (the Orion Nebula) has a comparable electron temperature

at (9200 ± 1600) K, with the fluctuation depending on the observational diagnostic (O'dell 2001).

Haworth et al. (2015) provided a temperature parameterisation of the same thermal balance calculation as in our model, but for an H II region expanding into an initially uniform-density medium. The ionized gas temperature is described by

$$T_i = T_n + \eta \left[1.1 \times 10^4 - 3.8 \times 10^3 \left(\frac{z}{z_0} - 0.5 \right)^{0.839} - T_n \right] \tag{4.8}$$

where T_n is a prescribed fully neutral gas temperature (e.g. 10 K or the dust temperature), η is the ionization fraction of hydrogen, and z is the metallicity relative to the Lexington benchmark metallicity z_0 (which we also use here; Ferland 1995; Ercolano et al. 2003; Haworth & Harries 2012). Haworth et al. used the same gas heating and cooling rates as our model, and so it accurately matches our volume-average temperature (9000 K; Fig. 4.8). (The two models used slightly different dust size distributions, so the gas-grain heat exchange term would be different; however, in the ionized gas, the rates of ionization heating and metal cooling would dominate over the gas-grain exchange rate.) This equation may be useful for those looking to use a simplified temperature scheme to account for the same thermal balance terms as our calculation, provided the ionization fraction is already known. However, it does not take into account the scatter in temperature which is about 10 per cent.

4.6.3 FUV interstellar radiation field

In section 4.5.4 we showed how the FUV flux reaching a 0.88 $M_\odot$ star increases rapidly as gas is removed from its surroundings. Photons at these wavelengths (912 to 2400 Å) cause photolelectric heating of dust and photodissociation of H_2 (Draine 1978; Osterbrock & Ferland 2006). Protoplanetary disks, or proplyds, around such stars in real star-forming regions are therefore stripped of material as the thermal pressure increases, resulting in a photoevaporative wind blowing from their outer layers (O'dell et al. 1993; Kim et al.

2016). This is not negligible, as external irradiation from other stars can be greater than internal irradiation by many orders of magnitude (Bruderer et al. 2012). Disk models typically include some external source of flux that remains constant in time (e.g. Haworth et al. 2016), but this is not representative of real clusters where stars move around and gas is displaced – a proplyd may see a radiation field that switches 'on' or 'off' depending on the intervening gas dynamics. This may in turn affect proplyd dispersal rates.

4.7 Synthetic observations

Synthetic observations are produced using the temperatures, densities, dust properties, elemental abundances and ionization fractions that were calculated and evolved during the RHD model – they were not modified with any post-processing. In this section, we analyse the model with both photoionization and radiation pressure.

4.7.1 Recombination and forbidden lines

We produce synthetic observations of the hydrogen recombination line Hα at 6563 Å, and collisionally excited metal forbidden lines of [S II] at 6731 Å and of [O III] at 5007 Å. Fig. 4.13 shows a three-colour composite at 0.2 Myr intervals corresponding to the column density snapshots in Fig. 4.4. Each line is scaled up to have the same minimum and maximum. As a representative example of the range of original surface brightnesses, at 0.6 Myr the [S II] brightness varies between 0.03 and 9000 MJy sr^{-1}; Hα lies between 0.3 and 3×10^4 MJy sr^{-1}; and [O III] has values between 0.1 and 10^4 MJy sr^{-1}. All three lines are strongest around clumps of high density, where cooling is more efficient, with the [S II] line showing the greatest difference in brightness between diffuse gas and dense gas. This causes the brown colour in the composite. From 0.4 Myr onwards there are several clumps with bright-rimmed envelopes and tails pointing radially away from the massive star. These characteristics are shared with the proplyds, elephant trunks, and cometary knots seen in well-known H II regions spanning multiple size scales, such as the

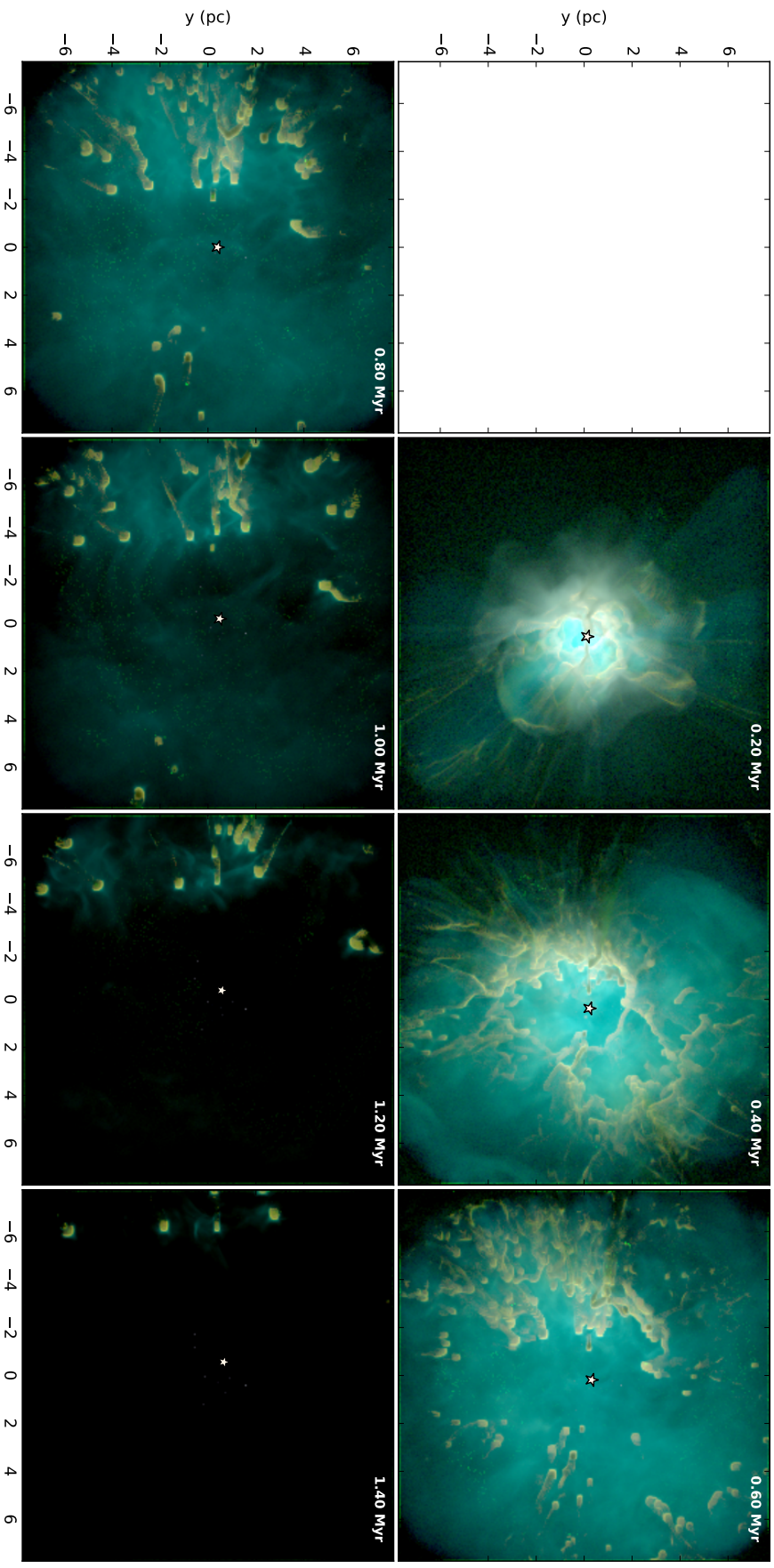

Figure 4.13: Three-colour images using synthetic observations of [S II] 6731 Å (red), Hα (green), and [O III] 5007 Å (blue), at 0.2 Myr intervals (corresponding to the column density maps in Fig. 4.4). The 34 $M_\odot$ star is indicated by a point near the centre of each frame.

Orion Nebula, NGC 7293 (the Helix, a planetary nebula; O'Dell 2000), the Carina nebula (Haikala et al. 2017), the Eagle nebula, and the Rosette cloud (Tremblin et al. 2013). Masses and sizes in the model are of the order 1 to 30 $M_\odot$ and 0.1 to 1 pc^2.

4.7.1.1 Hα line luminosity

In Fig. 4.14 we plot the intrinsic Hα luminosity $L_{\rm int}$ and the observed luminosity $L_{\rm obs}$ as a function of time, where

$$L_{\rm int} = \int 4\pi j_\nu \, {\rm d}V \tag{4.9}$$

and

$$L_{\rm obs} = 4\pi d^2 S_\nu \tag{4.10}$$

where j_ν is the emission coefficient, S_ν is the Hα flux density, or surface brightness integrated over solid angle, and we have arbitrarily observed the model at a distance $d = 400$ pc (the distance to the Orion Nebula) from three different viewing angles $(\theta, \phi) = (0, 0), (90, 0), (90, 90)$ with the colatitude θ and azimuthal angle ϕ in degrees. Within the cloud itself, $L_{\rm obs}$ is reduced along the line of sight due to absorption and scattering by dust. The extinction $A({\rm H}\alpha)$ in magnitudes is

$$A({\rm H}\alpha) = -2.5 \log_{10} \left(\frac{L_{\rm obs}}{L_{\rm int}} \right) \tag{4.11}$$

and this is also plotted in Fig. 4.14. The peak intrinsic luminosity, 8×10^{36} erg s^{-1}, is reached at 0.2 Myr and this drops below 10^{35} erg s^{-1} after a Myr. The extinction is a few magnitudes within the first 0.4 Myr while the H II region is still embedded within the cloud, after which the extinction drops to zero as the region becomes optically thin.

Two schemes of scattering are considered. The first uses the peel-off method (see Yusef-Zadeh et al. 1984): for photon packets which start off travelling away from the line of sight, their scattering events forcibly direct some light towards the observer (regardless of the new direction of the photon packet). This therefore adds scattered light from

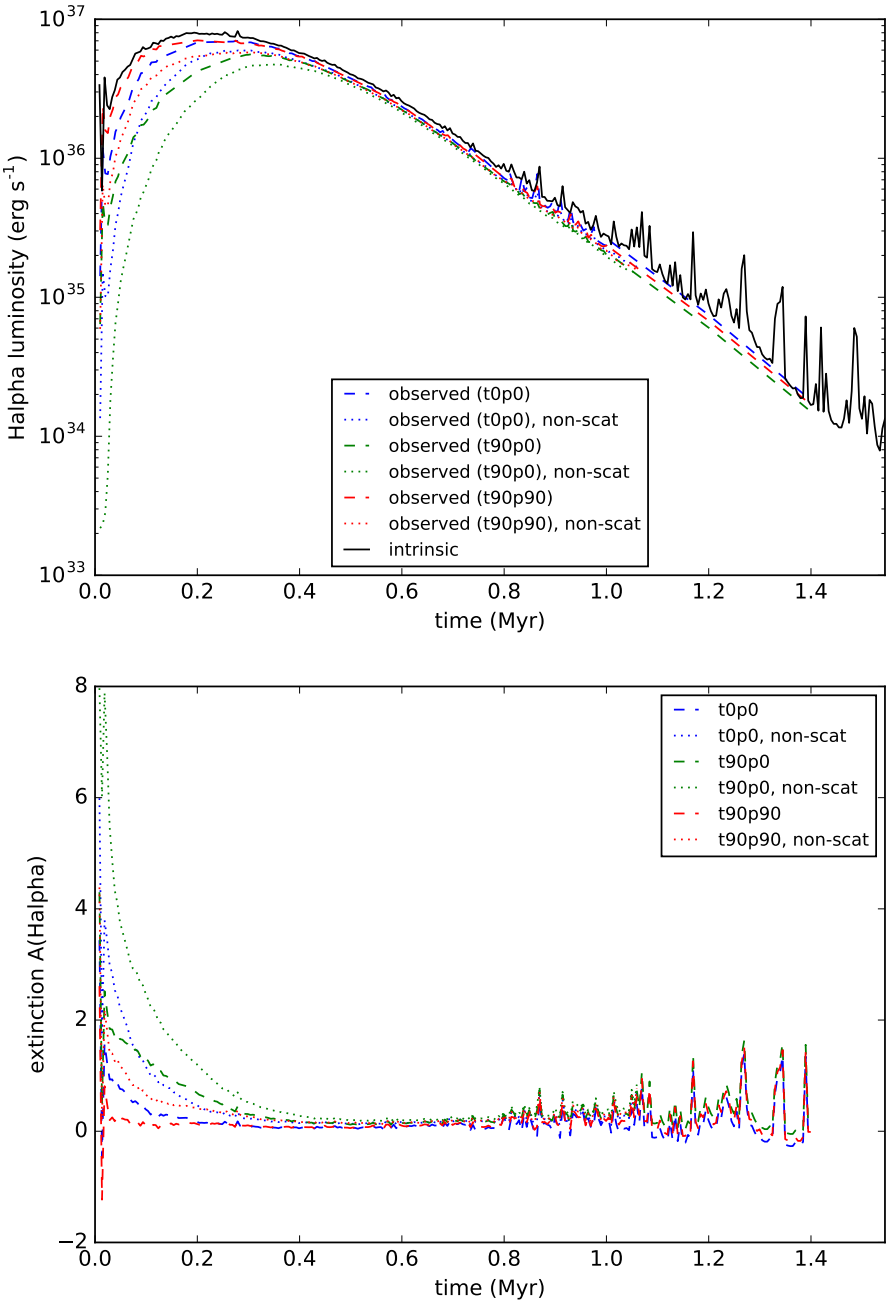

Figure 4.14: Top - Hα luminosities as a function of time, with the intrinsic luminosity in solid black, and observed luminosities at viewing angles $(\theta, \phi) = (0, 0), (90, 0), (90, 90)^\circ$ in blue, green, and red respectively. Observations without taking into account scattering from other lines of sight are in dotted lines, observations with scattering are dashed – see section 4.7.1.1 for a full description. Bottom - extinctions for the aforementioned parameters.

other lines of sight into the observed beam. Additionally, photon packets which do travel directly towards the observer may be scattered away from the observed beam. The second scattering scheme (labelled 'non-scat' in Fig. 4.14) only accounts for the latter effect – scattering from other lines of sight is not included.

The extinction between different viewing angles differs by 1 to 2 magnitudes. Furthermore, the extinction with the full scattering treatment is lower by a magnitude compared to observations neglecting the peeled-off photons. This is because the emitting gas is surrounded by dense filaments of dust which has a scattering opacity peaking near 6563 Å (see Fig. 4.2), and this directs light *towards* the observer, partially compensating for absorption and scattering *away* from the observer. Fluctuations in the extinction after 0.8 Myr arise from small differences in ionization; this has a more pronounced effect on the luminosity at late times as the luminosity is already dim, the ionized gas is diffuse, and recombination lines are sensitive to the square of the density.

4.7.2 Free–free radio observations and Lyman flux

It is possible to estimate the rate of Lyman continuum photons ($\lambda < 912$ Å; $h\nu > 13.6$ eV) being produced in a nebula using radio observations. Rubin (1968) derived an expression to calculate this assuming photoionization equilibrium, which implies

$$\dot{N}_{\rm Ly} \geq \int n_e [n(\mathrm{H\,II}) + n(\mathrm{He\,II})] \alpha(T)\, \mathrm{d}V \tag{4.12}$$

where $\alpha(T)$ is the recombination rate coefficient. Rubin uses the same α for H and He, and to be consistent with the literature and to test the resulting diagnostic, we do the same in our analysis. This takes the form

$$\alpha(T) = 4.10 \times 10^{-10} T^{-0.8}. \tag{4.13}$$

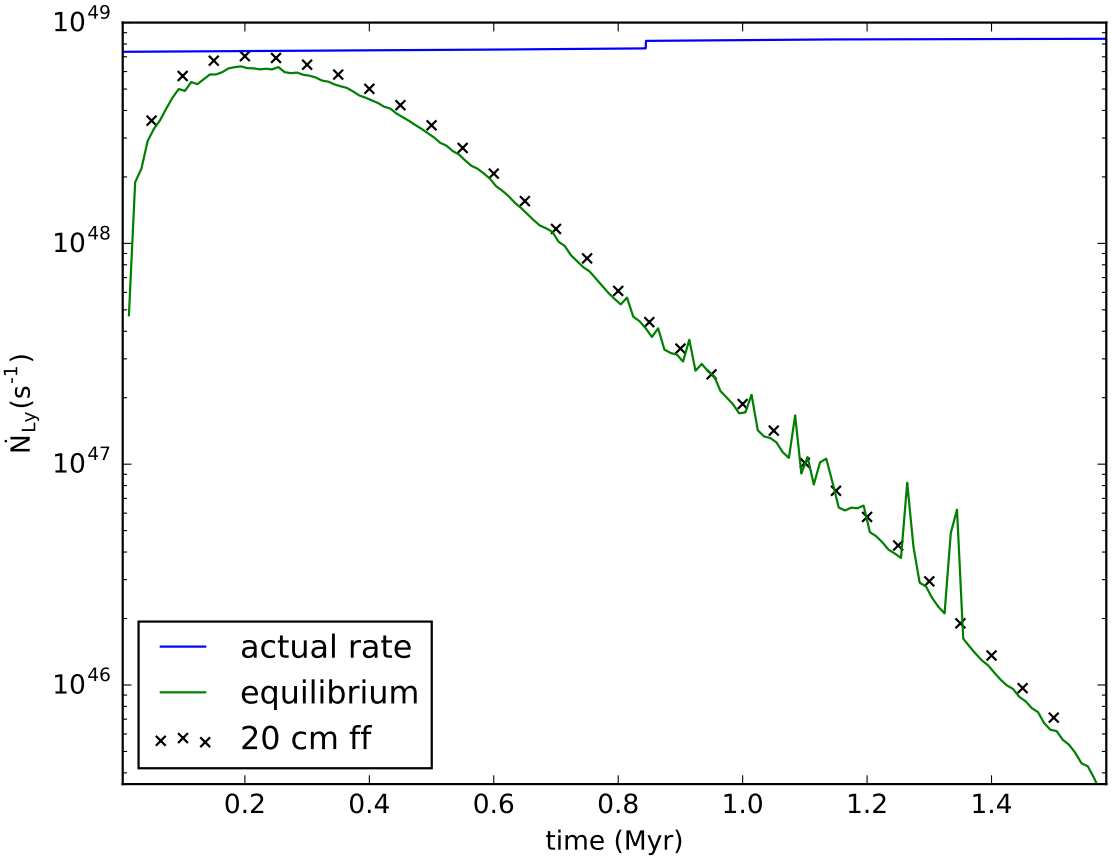

Figure 4.15: Total production rate of Lyman continuum photons as a function of time. Actual rate from integrating stellar spectra in blue. Rate from assuming photoionization equilibrium, equation (4.12), in green. Rate inferred from 20 cm free-free emission, equation (4.16), as black crosses.

The optical depth for free-free radiation is

$$\tau_\nu^{\mathrm{ff}} = 8.235 \times 10^{-2} \left(\frac{T}{\mathrm{K}}\right)^{-1.35} \left(\frac{\nu}{\mathrm{GHz}}\right)^{-2-\beta} \int \left(\frac{n_e n_i}{\mathrm{cm}^{-6}}\right) \frac{\mathrm{d}s}{\mathrm{pc}} \tag{4.14}$$

(Altenhoff et al. 1960; Mezger & Henderson 1967) where $n_i = n(\mathrm{H\,II}) + n(\mathrm{He\,II})$. If $\tau_\nu^{\mathrm{ff}} \ll 1$, the free-free surface brightness is

$$I_\nu \approx \frac{2kT\nu^2}{c^2} \tau_\nu^{\mathrm{ff}}. \tag{4.15}$$

Comparing with equation (4.12) leads to Rubin's expression for the Lyman continuum production rate

$$\dot{N}_{\mathrm{Ly}} \geq 4.76 \times 10^{42} \left(\frac{\nu}{\mathrm{GHz}}\right)^{\beta} \left(\frac{D}{\mathrm{pc}}\right)^2 \left(\frac{T_0}{\mathrm{K}}\right)^{-0.45} \left(\frac{S_\nu}{\mathrm{Jy}}\right) [\mathrm{s}^{-1}] \tag{4.16}$$

where S_ν is the surface brightness integrated over the solid angle subtended by the object observed from a distance D, T_0 is the average temperature, ν is the observation frequency, and β is a spectral index; this depends on the free-free Gaunt factor and is usually 0.1 in the literature (e.g. Mezger & Henderson 1967; Rubin 1968; Lefloch et al. 1997; Kim et al. 2017a). Equations (4.12) and (4.16) represent a lower limit in a density-bounded H II region.

We apply equation (4.16) to infer the Lyman continuum flux from synthetic observations of 20 cm free–free emission at 0.05 Myr intervals. We use a representative temperature of 9000 K as equation (4.16) is only weakly dependent on T_0 and this is the average temperature in our simulation (see Fig. 4.8). The spectral index β is calculated to be 0.15. We plot the results in Fig. 4.15, along with the known production rate taken from the integrated stellar spectra. We also compare this with the equilibrium equation (4.12), which does not depend on any synthetic observations.

The radio measurement closely matches the result from equation (4.12) at all times, showing that the radio emission is accurately measured and tracks photoionization balance

consistently. Before 0.2 Myr, both results underestimate the actual photon production rate by a factor of a few. Rubin's method assumes that Lyman continuum photons only go into ionizing the gas, neglecting the number which are absorbed by dust grains and thermally re-emitted in the infrared, reducing the number available for the gas. Since the star at this stage is deeply embedded in a node between filaments, dust absorption is not negligible. Once the H II breaks out, however, the probe becomes more reliable, matching the actual emitted photon flux at 0.2 Myr. After this stage, the radio flux decreases along with the electron density, and by 0.8 Myr the measured $\dot{N}_{\rm Ly}$ is an order of magnitude lower than the known production rate. By the end of the simulation the discrepancy is 10^3. Mass begins to leave the grid after around 0.4 Myr, so after this stage the ionizing photons may escape from the volume; if our cloud represents a core embedded inside a larger GMC, these photons could go on to excite gas beyond the model boundary. This would account for the increasing discrepancy at later times. Since the radio method is used by observers to get spectral classifications of O-stars, this highlights the importance of knowing the full size scale of an H II region – for a limited observational field of view, the Lyman flux can be underestimated by several orders of magnitude.

4.7.3 Dust emission

These synthetic observations were calculated using dust temperatures which are decoupled from gas, apart from the collisional heat exchange term in equation (2.43).

Dust surface brightness depends on the Planck function $B_\nu(T_d)$ and in the optically thin limit is also proportional to the dust opacity. Taking the ratio of brightnesses at two wavelengths allows the dust temperature to be calculated if the opacity spectral index is known:

$$\frac{S_{\lambda_1}}{S_{\lambda_2}} = \left(\frac{\lambda_2}{\lambda_1}\right)^{3+\beta} \frac{\exp\left(hc/\lambda_2 k T_d\right) - 1}{\exp\left(hc/\lambda_1 k T_d\right) - 1} \tag{4.17}$$

where $S_{\lambda_1}, S_{\lambda_2}$ are the surface brightnesses at wavelengths λ_1, λ_2, and β is the dust opacity spectral index. β is normally taken to be 2 for regions such as the one modelled here (e.g.

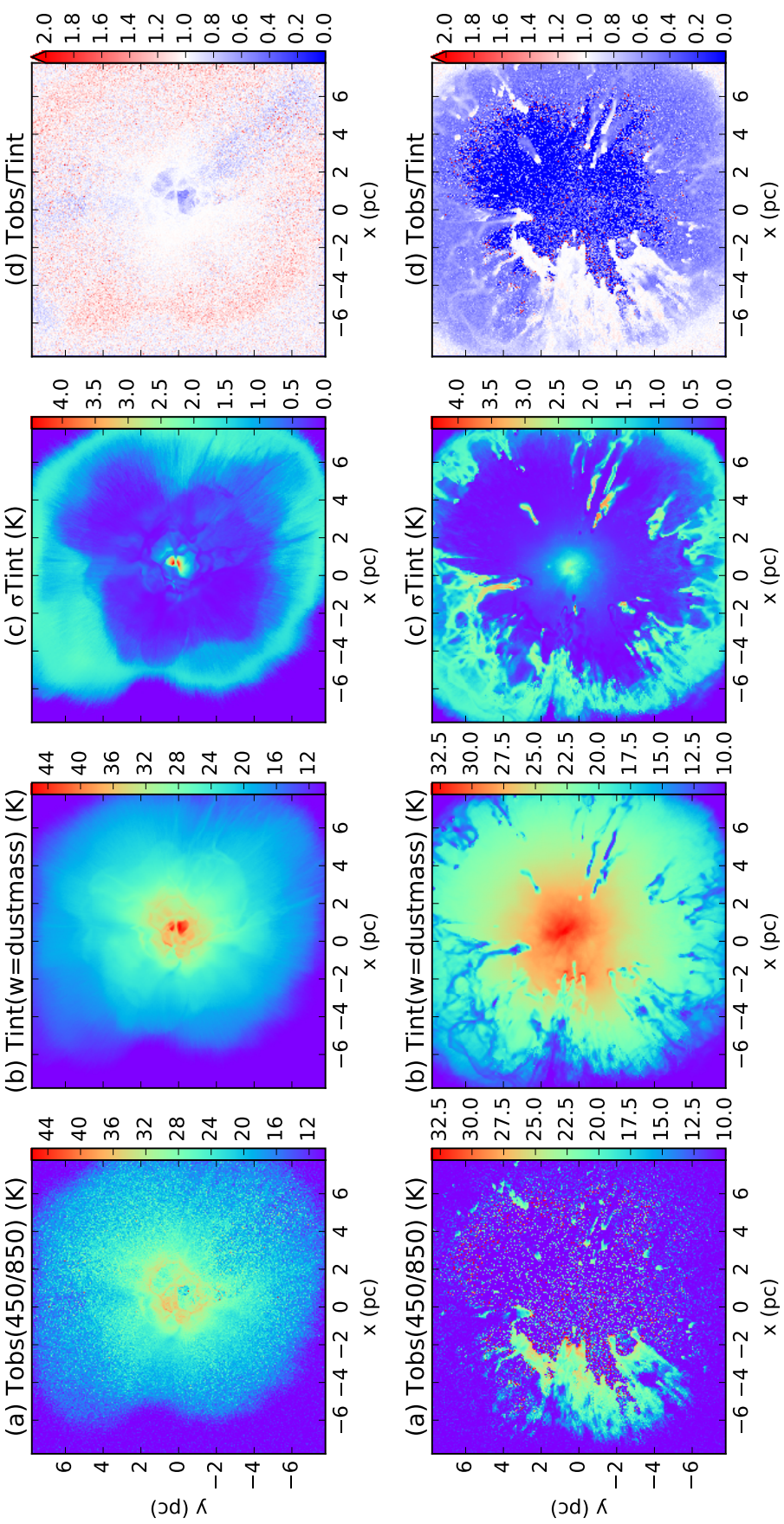

Figure 4.16: (a) Dust temperature extracted from 450 and 850 μm dust emission at 0.2 Myr (top row) and 0.6 Myr (bottom row). (b) Intrinsic temperature averaged along the line of sight, weighted by dust mass. (c) Standard deviation of the intrinsic temperature normalised by the average. (d) Ratio of (a) and (b).

Reid & Wilson 2005; Sadavoy et al. 2012; Rumble et al. 2015; Figueira et al. 2017) and this is the value we use.

We apply equation (4.17) pixel-by-pixel to synthetic observations at 450 and 850 μm, corresponding to the Submillimetre Common User Bolometer Array (SCUBA-2) on the James Clerk Maxwell Telescope (JCMT). The resulting temperature map is presented in Fig. 4.16, next to an intrinsic value $\langle T_d^{\rm int} \rangle$ which is a dust-mass-weighted average along the line of sight calculated directly from the RHD model.

The observed temperature $\langle T_d^{\rm obs} \rangle$ is accurately recovered in dense filaments. In warm diffuse gas, the dust temperature is underestimated by a factor of 2 and this gets worse as the H II region cavity grows and becomes less dense. This is where the most massive star is located and is where discrepancies are highest. Koepferl et al. (2017b) produced synthetic dust emission from SPH models of Dale et al. (2014) and concluded that errors in temperature were present in regions which had both low density and high temperature dispersion. We agree with this at early times when the H II is still mostly confined (top row of Fig. 4.16). At later times when the H II region is extended and diffuse, inconsistencies are more correlated with low densities, with some high-temperature dispersion areas still being recovered fairly accurately (e.g. the filaments on the right of the bottom row of Fig. 4.16). They also note that their errors are found in places that are cooler than their surroundings and are greatest at the edge of the H II region. We do not in general find this to be the case, as the differences in our model are concentrated in the interior at both early and late stages; furthermore, some cool filaments entrenched in warmer areas still have accurate temperatures. Koepferl et al.'s method of SED fitting requires both the surface density and dust temperature to be free parameters, with overestimates in one leading to underestimates in the other. The method we employ here does not make any assumption on the density and therefore any discrepancies are discrepancies in temperature only. Using the ratio method only requires observations at two wavelengths, while the blackbody fitting method needs many wavelengths – temperatures in dense regions with low temperature dispersion are accurately calculated using both methods, so in these areas observers may

find the ratio method more useful due to its less stringent data requirements.

4.8 Summary and conclusions

We have modelled a 1000 $M_\odot$ cloud containing a 34 $M_\odot$ massive star including photoionizing radiation and radiation pressure feedback. In summary:

- The cloud is dispersed within 1.6 Myr or 0.74 $\langle t_{\rm ff} \rangle$, with all mass leaving the $(15.5\,{\rm pc})^3$ grid over this time.
- Thermal pressure from photoionization is an efficient feedback mechanism, causing mass fluxes of the order $10^{-3}\,M_\odot\,{\rm yr}^{-1}$ at the simulation volume boundary.
- At most 40 per cent of the mass gets ionized (440 $M_\odot$), while almost 90 per cent of the volume gets ionized. This arises from the densest filamentary structures resisting ionization, getting shovelled by the expanding ionization front into globules and pillars, which remain neutral and shield downwind material from the stellar radiation field.
- Radiation pressure plays a negligible role, causing only a slight advance in the breakout of the ionization. It is expected to be more significant at higher number densities, $n > 100\,{\rm cm}^{-3}$ (Draine 2011).
- We use a detailed radiative transfer scheme in our models, calculating photoionization balance and thermal balance before each hydrodynamics timestep. Ionization fractions are calculated for multiple atomic species, and temperatures are calculated for gas and dust separately. These are then used to create self-consistent synthetic observations.
- We also calculate the FUV interstellar radiation field, G_0, throughout the simulation volume, including around sink particles which can suddenly be exposed to the flux from the massive star as gas is dispersed.

Our synthetic observations include line and continuum emission. We have tested the use of radio free-free emission in probing the production rate of Lyman continuum photons. The 'observed' rate is almost always underestimated – by a factor of a few at early times (before 0.4 Myr), and by up to three orders of magnitude at late times (once significant amounts of mass have left the simulation volume, and thus photons would excite this gas beyond the boundary). We emphasise that radio measurements serve as a lower boundary on the production rate, especially when only part of the H II region is observed and if ionizing photon escape fractions are not also measured.

We also investigated the use of brightness ratios of synthetic dust continuum at two wavelengths (450 and 850 μm) to probe the dust temperature. This accurately recovers the actual temperature in regions of high density and low temperature dispersion. However, in low densities or high temperature dispersions, the 'observed' temperature is underestimated by a factor of 2 or more, getting worse at late stages in the very diffuse H II region ($n \lesssim 3\,\mathrm{cm}^{-3}$). At high densities the ratio method is as accurate as SED-fitting which requires more than two wavelengths and has surface density as an additional free parameter that can cause further discrepancies in temperature (Koepferl et al. 2017b).

The cloud we have modelled here represents a cloud core as opposed to a GMC in its own right, therefore it would be embedded inside a larger-mass object, which itself would be inside an even larger-mass one. In future models we plan to go up the hierarchy to full GMC-scale regions of $10^6\,\mathrm{M}_\odot$ and 100 pc. Currently we place stars as sink particles in dense regions, but the particles do not accrete material (though they do move around with gas and N-body interactions). For the higher-mass cloud models, we will implement a subgrid model for sink particles such that they represent clusters of stars, and will enable accretion so that they grow self-consistently. This is discussed further in chapter 6.

Chapter 5

Feedback in a 10,000 solar mass cloud

5.1 Abstract

In this chapter I model a $10^4\,M_\odot$ cloud, 10 times more massive than the cloud modelled in chapter 4, with the same surface density ($0.01\,g\,cm^{-2}$) and the same stellar mass distribution (including a $34\,M_\odot$ star). This calculation uses the same Monte Carlo radiative transfer ingredients, including photoionization and radiation pressure feedback, with multiple atomic species and $\sim 0.1\,\mu m$ silicate dust grains.

This cloud is efficiently dispersed, but is also somewhat more resistant than the lower-mass one, with 25 per cent of the mass remaining inside the $(32.3\,pc)^3$ grid after 4.3 Myr ($1.1\,\langle t_{ff}\rangle$). At most 20 per cent of the mass is ionized, compared to 40 per cent in the previous chapter – despite the similar proportion of the volume being ionized (80 percent). The total Jeans-unstable mass increases linearly up to $1500\,M_\odot$ in the first 2 Myr, before plateauing – this corresponds to a core formation efficiency of 15 per cent, relative to the total initial mass, as a crude upper boundary.

I also present the time-dependence of the FUV radiation field at the positions of all other stars in the cluster. It takes approximately 0.5 Myr for many of the stars to be illuminated by the most massive star, as the latter must first disperse the core in which it is embedded. Once this occurs, G_0 can increase by orders of magnitude. Intervening parcels

of gas can cause comparable decreases in flux for $\sim$ 1 Myr durations, before rapidly rising again.

5.2 Introduction

Star formation occurs in giant molecular clouds. Solomon et al. (1987) and Heyer et al. (2009) characterised the masses and sizes of observed GMCs in the Galaxy, finding them to range in mass between $\sim 10^4$ to $10^6\,\mathrm{M}_\odot$, with radii of a few to 100 pc. They contain inside them structures called clumps, of the order $1000\,\mathrm{M}_\odot$. The dynamics of these GMCs are likely to be dominated by the massive stars contained within, via their radiative output – in particular, their photoionizing luminosity (Matzner 2002).

Simulations of stellar feedback including photoionization show that the dispersal and expulsion of gas depends on the initial conditions – high mass clouds seem to be more resilient to the ionizing radiation, which can stream out through low-density channels carved out in the turbulent, inhomogeneous gas distribution; see, for example, Dale & Bonnell (2011); Dale et al. (2012, 2013a). In particular, these authors argue (Dale 2015) that the escape velocity of the cloud determines how much mass gets unbound: the Larson (1981) scaling relations show a near-constant surface density for GMCs, implying that cloud radius increases with mass following $M \propto R^2$; since a cloud's escape velocity varies as $v_{\mathrm{esc}} = \sqrt{2GM/R}$, this results in $v_{\mathrm{esc}} \propto M^{1/4}$ which approaches the sound speed of ionized gas ($10\,\mathrm{km\,s^{-1}}$).

To further investigate the dependence of gas dispersal on initial condition, I model a larger mass cloud than in chapter 4, keeping the initial surface density the same. This provides another step towards exploring the parameter space defined by Galactic clouds, and allows comparison with similar models by other authors using different numerical techniques.

5.3 Initial conditions

I use the same setup as the model presented in chapter 4 (and Ali et al. 2018), except with an initial sphere mass that is 10 times greater ($M_s = 10^4\,\mathrm{M}_\odot$) and a radius $R_s = 8.41\,\mathrm{pc}$, such that the mean surface density $\Sigma_s = 0.01\,\mathrm{g\,cm^{-2}}$ is the same. The free-fall time associated with a uniform sphere with density $\rho = 3M_s/4\pi R_s^3 = 3 \times 10^{-22}\,\mathrm{g\,cm^{-3}}$ is $\langle t_{\mathrm{ff}} \rangle = 3.86\,\mathrm{Myr}$. The density in the inner core ($0 > r > R_s/2$) is $4.9 \times 10^{-22}\,\mathrm{g\,cm^{-3}}$ and at the outer edge ($r = R_s$) is $1.7 \times 10^{-22}\,\mathrm{g\,cm^{-3}}$. The temperature is 10 K everywhere (for both gas and dust) until radiation sources are switched on. The grid size from end to end is 32.3 pc, approximately 4 times the sphere radius, giving a linear resolution of 0.13 pc per cell with 256^3 cells. I keep the same number of stars and stellar masses in order to compare how the same luminosity affects a more massive cloud. This means the imposed star formation efficiency in this model is 1 per cent as opposed to 10 per cent. The stellar positions (plotted in Fig. 5.1) are not necessarily the same as in the lower-mass cloud, as they are placed using the method described in section 4.4 without any further constraints; however, since the turbulence in the initial hydrodynamics-only phase results in a similar morphology at $0.75\,\langle t_{\mathrm{ff}} \rangle$, when stars are created, the most massive star ends up being placed in roughly the same area of the cloud. This keeps the initial conditions broadly consistent, but just scaled up in cloud mass. The parameter space of cloud mass, radius, and velocity dispersion is shown in Fig. 5.2, alongside observations of GMCs in the Galaxy by Heyer et al. (2009) and the suite of simulations by Dale et al. (2012).

5.4 Results and discussion

In this section I present a simulation with photoionization and radiation pressure, and one with photoionization only. The models are evolved for approximately 4 Myr, with $t = 0$ corresponding to the initiation of feedback.

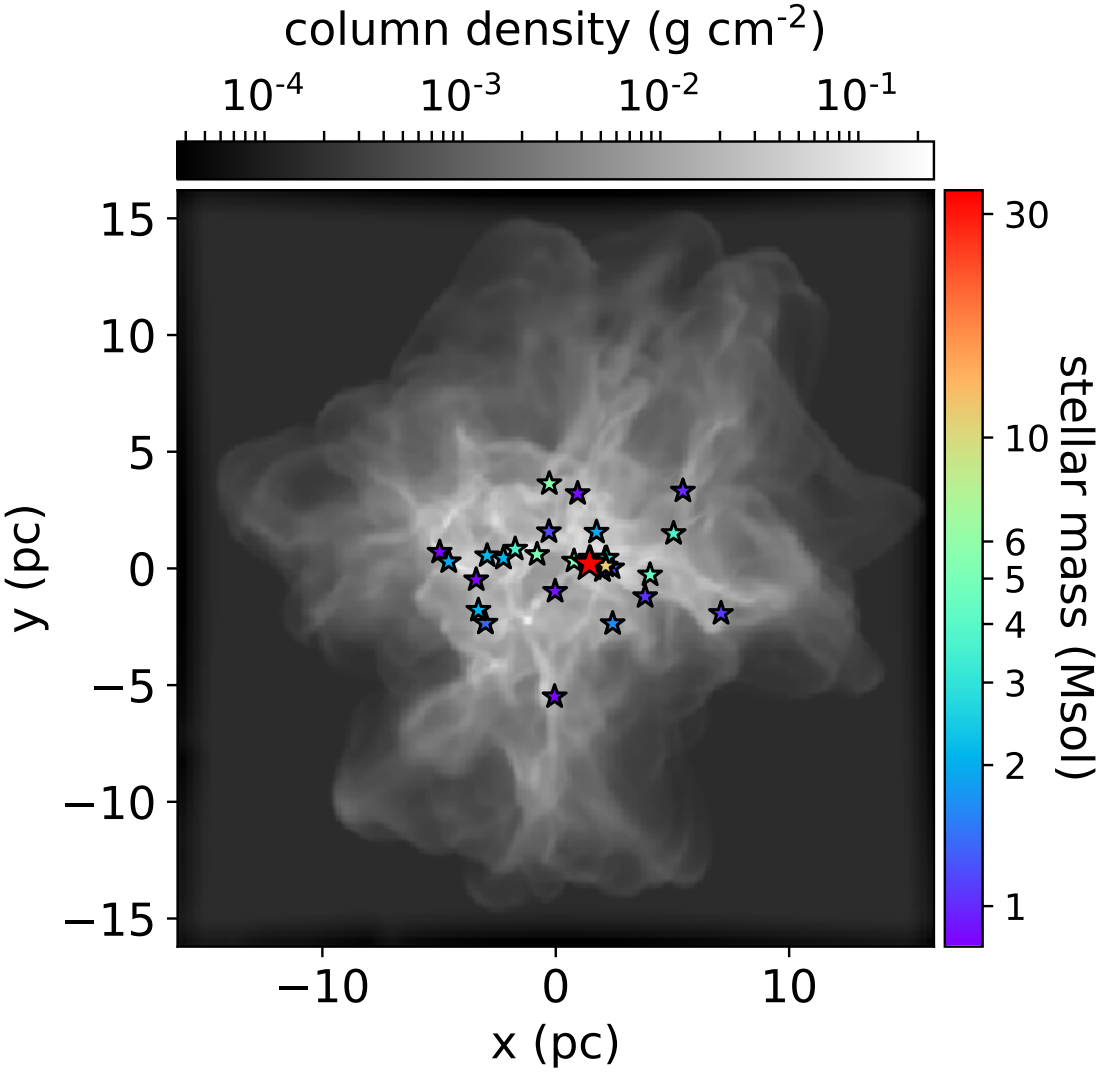

Figure 5.1: Positions of stars at the onset of feedback, with stellar mass in colour scale, overlaid on column density in greyscale (both are logarithmic). The most massive star is 33.7 $M_\odot$ in red. The second highest is 11.3 $M_\odot$. The third is 5.7 $M_\odot$. The least massive is 0.82 $M_\odot$.

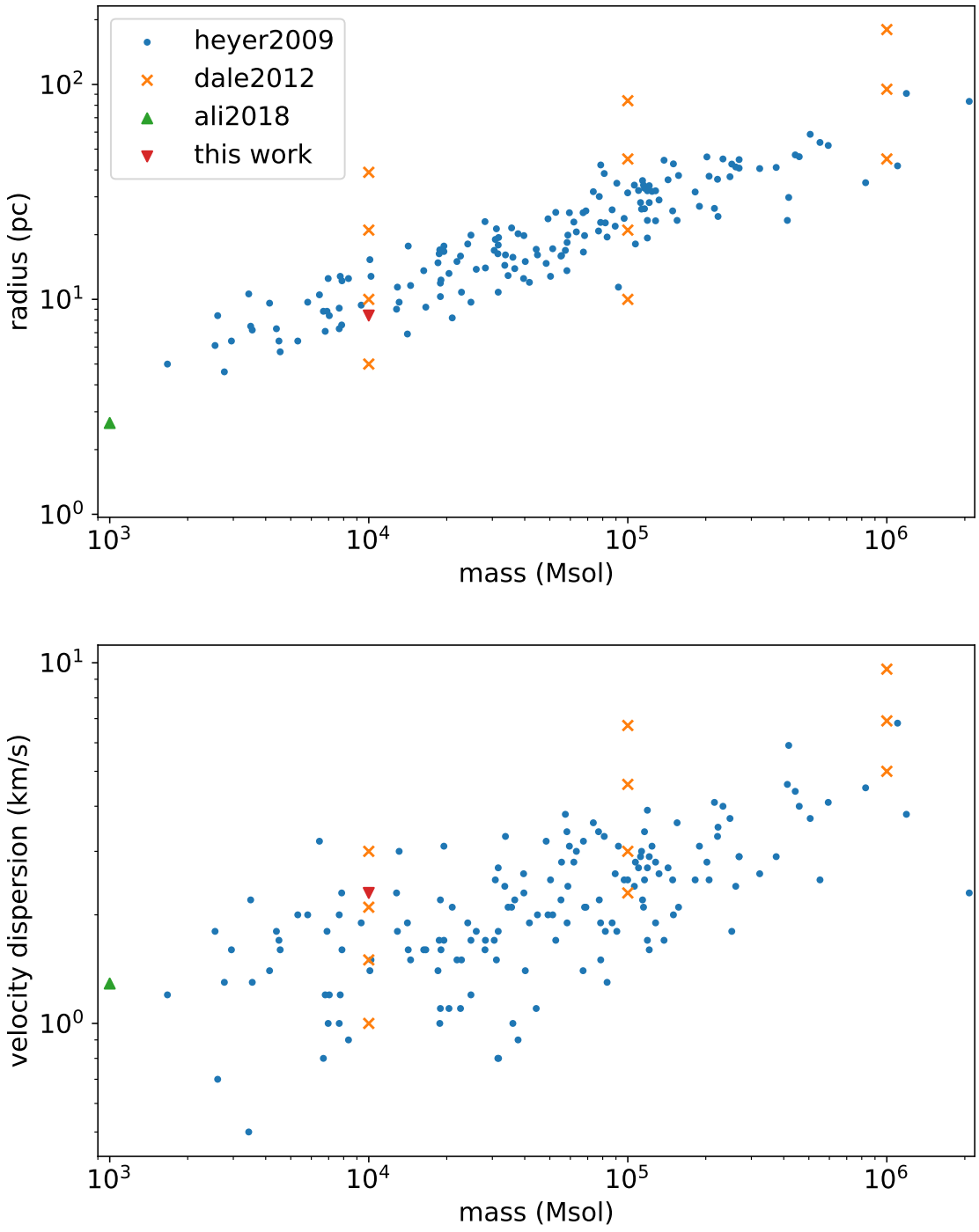

Figure 5.2: Parameter space of Galactic GMC observations by Heyer et al. (2009, dots), simulations by Dale et al. (2012, crosses), Ali et al. (2018, up-pointing triangle), and this chapter (down-pointing triangle).

5.4.1 Bulk grid properties

Fig. 5.3 shows the grid properties as a function of time. The first panel plots the total mass, which starts just under $1.2 \times 10^4\,M_\odot$ (counting the low-density material outside the $10^4\,M_\odot$ turbulent sphere); between 1 and 4 Myr, there is a steady decrease as mass leaves the grid. The total mass flux at the grid boundaries, shown in the second panel of Fig. 5.3, peaks between 1.5 and 2.5 Myr (0.39 and 0.65 $\langle t_{\rm ff} \rangle$ respectively) with a value of $4.7 \times 10^{-3}\,M_\odot\,{\rm yr}^{-1}$. This is more than double the mass flux in the $1000\,M_\odot$ model presented in chapter 4. However, the shape of the curve is essentially the same, with the first phase being dominated by the removal of low-density material, peaking at the crossing time for ionized gas travelling from the centre of the grid to the edge, with a sound speed $\approx 10\,{\rm km\,s}^{-1}$; the decreasing second phase is overlaid with sharp, short-lived spikes corresponding to dense clumps.

At 1.75 Myr (0.45 $\langle t_{\rm ff} \rangle$), the highest value of ionized mass is reached, with $1600\,M_\odot$, or about 17 per cent, of the mass being ionized; this proportion is half that of the low-mass model, which peaked at 40 per cent, again at the time of peak mass flux. This is despite about 80 per cent of the volume being ionized, which is comparable to the low-mass model. The conclusion reached in that model is even more so the case here – most of the mass remains in small, dense, neutral areas.

The final frame of Fig. 5.3 shows the total mass in Jeans-unstable cells (equation 1.4). This represents a crude upper limit in the amount of mass that could fragment to form stars; only a third of a core mass may actually be converted into stars (Alves et al. 2007). Furthermore, to prevent artificial fragmentation, the Jeans length

$$\lambda_J = \sqrt{\frac{\pi c_s^2}{G\rho}} \tag{5.1}$$

should be resolved by at least four grid cells (Truelove et al. 1997). This limit corresponds to a density $\sim 10^{-20}\,{\rm g\,cm}^{-3}$. Howard et al. (2014) use this as a density threshold above which cluster-sink particles are formed, based on observational constraints (Lada & Lada

2003). The total Jeans-unstable mass increases linearly to 1500 $M_\odot$ before plateauing at around 2 Myr (0.5 $\langle t_{\rm ff} \rangle$). Dense clumps start exiting the grid after this stage, which results in the unstable mass decreasing. In terms of the original cloud mass, this represents a core formation efficiency of 15 per cent, or a star formation efficiency of 5 per cent. This order of magnitude is in line with observations in the Galaxy (Lada & Lada 2003). It also agrees with the simulation by Geen et al. (2017), labelled 'L', which has a similar initial mass and surface density, and includes ionization feedback – Geen et al. (2017) found that the SFE for that cloud was closer to observations of local star-forming regions compared to denser models, where SFEs approached 100 per cent.

The bulk grid properties for the ionization-only model are in general similar to the combined feedback model, although there are minor differences. For example, there is a difference of 300 $M_\odot$ for the total Jeans-unstable mass. Since the inferred core- or star-formation efficiency is a rough estimate, this difference is not necessarily significant.

Fig. 5.5 shows column density histograms for the first 4 Myr. Compared to the low-mass cloud, they have similar shapes but are more homogeneous with time, only significantly shifting to lower surface densities beyond 3 Myr. This model starts off with more material in the low-density end, at $\Sigma = 10^{-4.5}$ g cm^{-2}, whereas the low-mass cloud stops at $\Sigma = 10^{-4}$ g cm^{-2}; therefore this model requires less of a left-ward shift to reach the $\Sigma = 10^{-5}$ g cm^{-2} peak by the end of the simulation. There is very little variation during the first 1.5 Myr (the total run time for the low-mass model), other than the spreading out of the high-density peak corresponding to the diffuse gas outside the cloud.

5.4.2 Dispersal

As in chapter 4, the dense filaments on the left side of the cloud are more resistant to being dispersed than the right side. In particular, a cavity is easily blown out in the bottom right quadrant of the x-y plane in the first Myr, allowing ionized material to stream out. This is also the case at ($x = 0, y > 0$) and ($x \approx 3$ pc, $y > 0$). It is not surprising that these

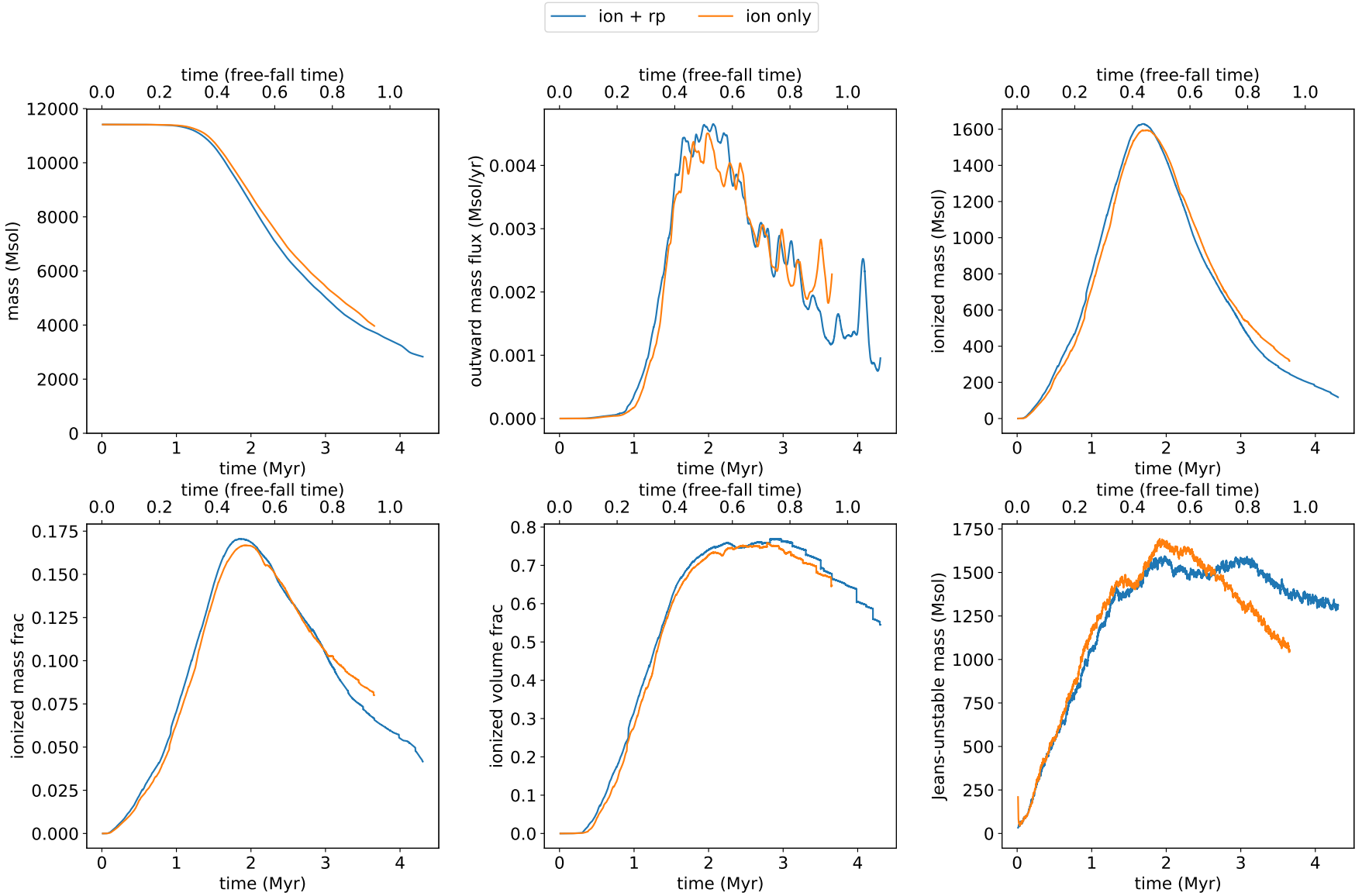

Figure 5.3: Bulk grid properties for the 10^4 $M_\odot$ cloud model. This shows as a function of time the total mass on grid, mass flux off the grid, ionized mass, ionized mass fraction, ionized volume fraction, and total mass in Jeans-unstable cells. The blue line is the model with ionization and radiation pressure; the orange line is only ionization. $t = 0$ corresponds to the onset of feedback.

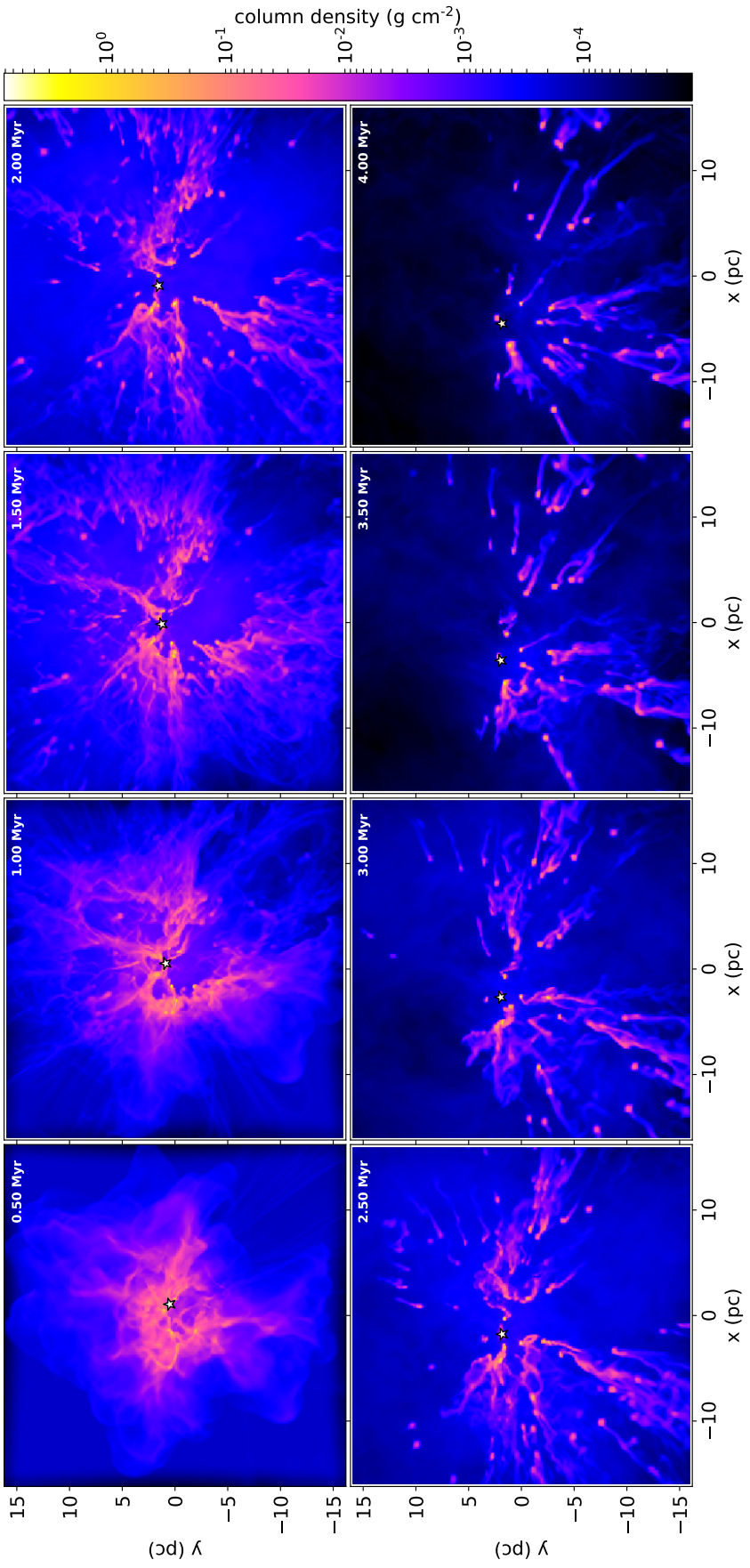

Figure 5.4: Column density integrated along the z-axis at 0.5 Myr intervals in the combined feedback model. Each frame is 32.3 pc a side. The 34 $M_\odot$ star is indicated with a point near the centre of each frame. $t = 0$ corresponds to the onset of feedback.

locations are where the H II breaks out, as this also happens in the low-mass cloud – both have a similar gravo-turbulent structure and a massive star in similar locations.

However, in this massive cloud, the dense filaments on the left side ($x < 0$ in the x-y plane) have more time to accumulate mass before the H II region can reach them. Indeed, the filaments are still collapsing towards the centre while feedback progresses. This makes them less prone to dispersal, whether by ionization heating or the rocket effect – by $t = 4$ Myr, many of the globule–pillar objects are still present inside a 8 pc radius around the massive star, which corresponds to the radius of the entire grid in chapter 4.

The initial conditions are similar to run I of Dale et al. (2012) (the closest point to this model in Fig. 5.2). Although their model starts off with a smoother density distribution than our model, a similar butterfly-shaped H II region is produced – this is the only model in their suite of conditions to create this morphology. Run I showed the greatest effect in terms of structure and dynamics, with 60 per cent of the gas being unbound. Their total ionization fraction did not exceed 10 per cent, whereas the model here approaches 20 per cent, even with similar ionizing fluxes ($\sim 10^{49}$ s^{-1}).

Dale et al. (2013a) summarised their parameter study of GMC masses between 10^4 to 10^6 M$_\odot$, stating that the ionized mass fraction is around 5 to 10 percent regardless of the cloud properties. This disagrees with the models presented here and in chapter 4, which approach fractions of 20 per cent and 40 per cent, respectively; that is, they are both higher and they vary with cloud mass. This is despite their models having ionizing luminosities which increase with cloud mass. As described in section 3.4, the Dale et al. models do not include the diffuse radiation field. This can penetrate into shadowed regions, and therefore more mass can be ionized. This also creates changes in morphology (e.g. pillar heads get detached) which help to explain the differences in total ionization fraction, as the environment becomes more permeable to ionizing radiation. Dale et al. find a strong dependence on dispersal efficiency with cloud escape velocity. $v_{\rm esc}$ for the cloud presented here is still very much below the ionized sound speed (~ 3 km s^{-1} compared to 10 km s^{-1}), but the full parameter space is yet to be explored.

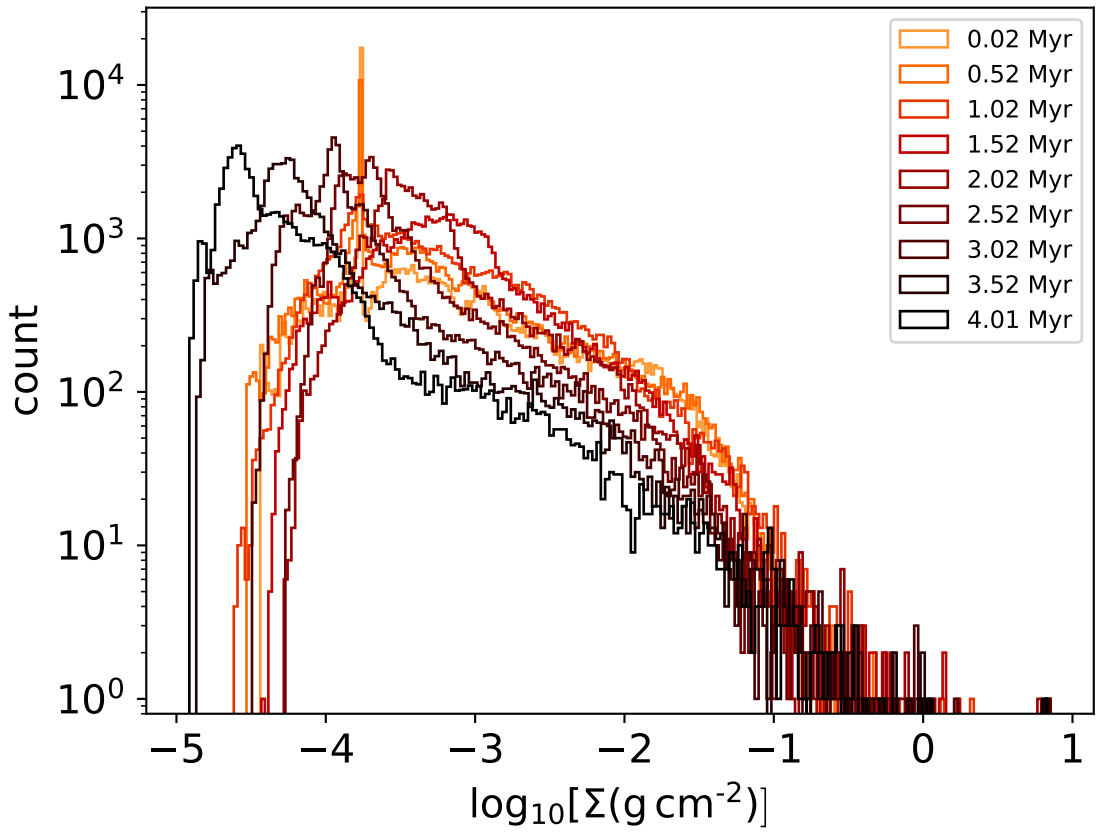

Figure 5.5: Column density histograms at 0.5 Myr intervals for the combined feedback model. The spike at $t = 0$ (the onset of feedback) corresponds to the stationary, uniform-density material outside the turbulent cloud.

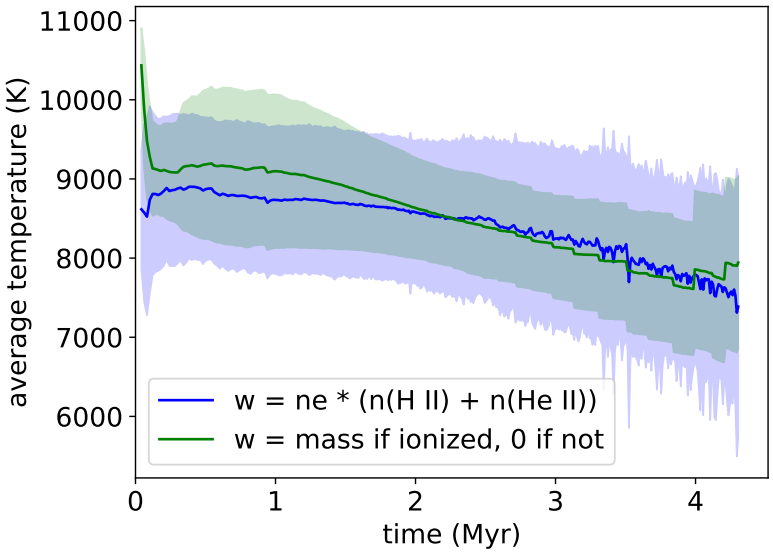

Figure 5.6: Volume-average ionized gas temperature (with filled boundaries showing the standard deviation), plotted against time. The average is weighted by $w = n_e(n_{\mathrm{H\,II}} + n_{\mathrm{He\,II}}) \approx n_e^2$ (blue), mass $w = \rho\Delta V$ if the cell is more than 90 per cent ionized or $w = 0$ if less (green). This shows the model containing both feedback processes.

5.4.3 Temperature and electron density

Fig. 5.6 and Fig. 5.7 show the average temperature and electron density, respectively, of the ionized gas, using the methods described in section 4.5.3. The results follow a similar pattern as the low-mass cloud, with both weighted-averages of the temperature decreasing down to 8000 K by the end of the 4 Myr. The electron density goes down to 0.3 cm^{-3}, again closely matching the low-mass cloud. This average density corresponds to a proton mass density of $5 \times 10^{-25}\,\mathrm{g\,cm}^{-3}$, which is five times more than the simulation floor density of $10^{-25}\,\mathrm{g\,cm}^{-3}$.

5.4.4 FUV interstellar radiation field

The FUV radiation field (equation 3.32) is calculated at all time steps in every cell. The sink particles can be used as test particles representing stars or proplyds, so I calculate G_0 at each of their cell positions. When a sink moves between cells, however, its measured flux may jump up or down due to the discrete nature of the grid structure. Therefore, I average around a radius of 2.5 grid cells (which, if accretion were enabled, would

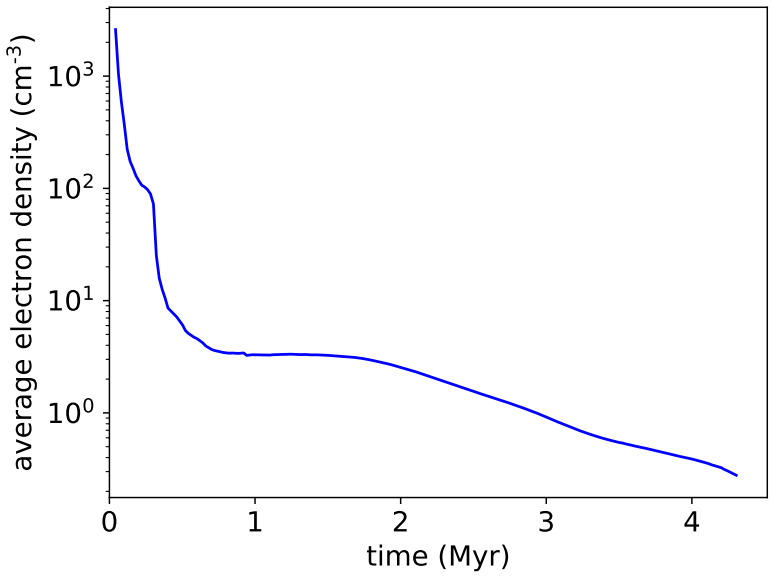

Figure 5.7: Volume-average electron density n_e in the ionized gas, plotted against time. This shows the model containing both feedback processes.

represent the computational accretion radius, but is simply a convenience factor here). The time-dependence of the flux is plotted for every star in Fig. 5.8, alongside the distance to the 34 $M_\odot$ star, which dominates the emission. The results can be roughly split into three categories: stars which start off shielded but then become exposed with G_0 rapidly jumping up; stars which experience shielding later on such that G_0 either dips temporarily, or remains constant despite getting closer to the massive star; stars where the separation is the dominant factor in determining the variation in G_0. These are not exclusive.

In the following sections, I describe the former two categories, referring to the stars by their indices 1 to 29 (where 1 is the most massive star, and 29 is the least massive). The corresponding initial stellar masses are labelled in Fig. 5.8.

5.4.4.1 Sudden illumination

Star 7 begins 4.25 pc away from the massive star (star 1), then moves to 6 pc over 4 Myr. However, its value of G_0 is lowest at the beginning, despite this being its closest approach; it takes 0.75 Myr to rise by a factor of $\sim$ 3 to $G_0 = 200$. This occurs as the massive star disperses material around itself, allowing its radiation field to reach more stars in the

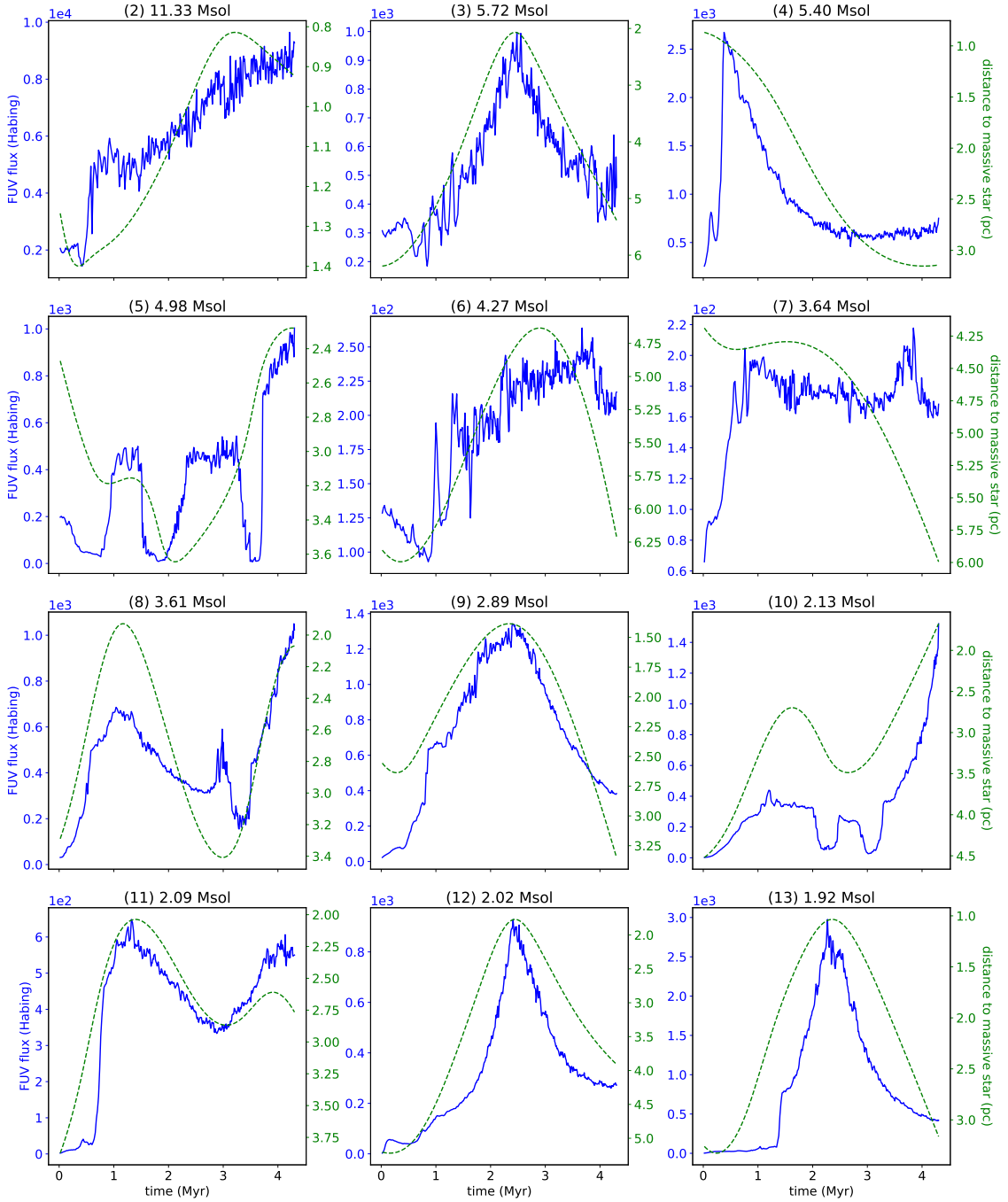

Figure 5.8a: FUV interstellar radiation field G_0 in units of the Habing flux (1.63×10^{-3} erg s^{-1} cm^{-2}) for all non-massive stars (solid blue line, left axis). The dashed green line (right axis) shows the distance to the most massive star in pc – note that the axis goes from high to low separation. Continues on next page.

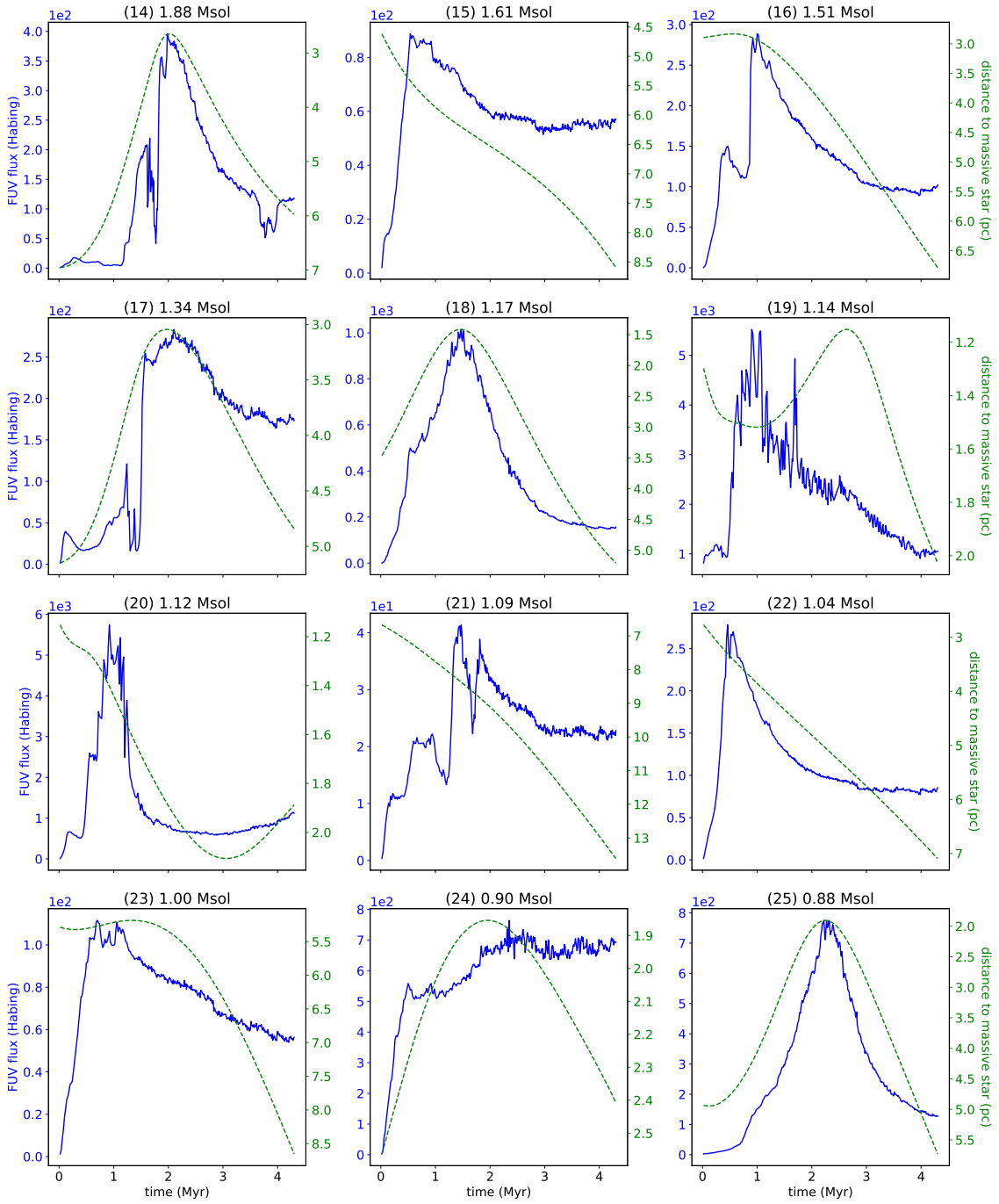

Figure 5.8b: Continued from previous page.

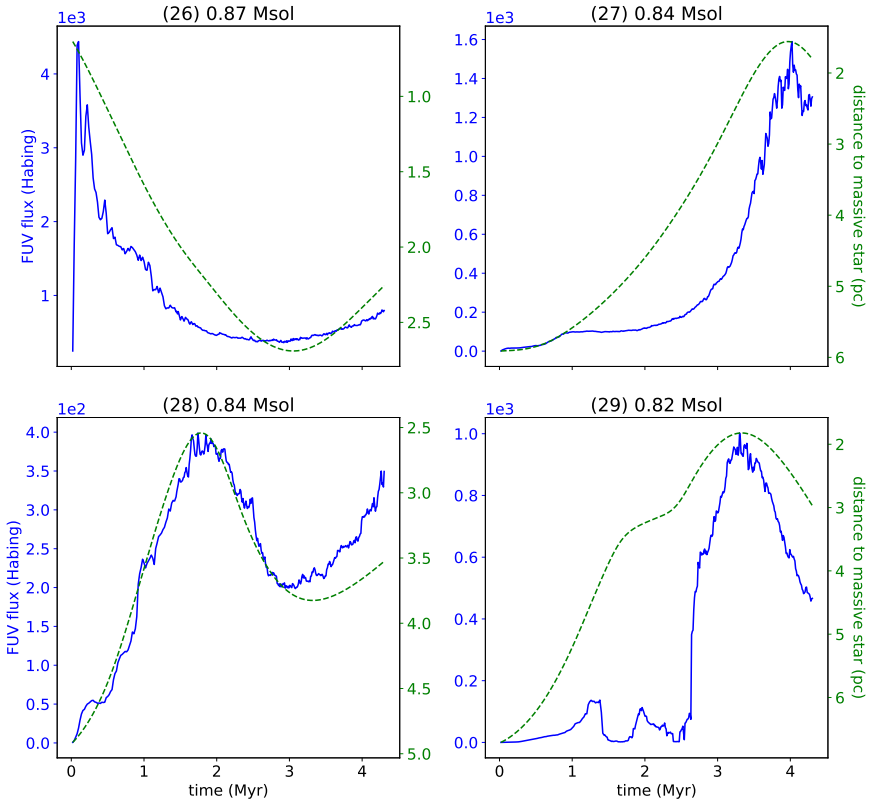

Figure 5.8c: Continued from previous page.

cluster with less intervening opacity. The column density between the two stars reduces around the 4 Myr mark, which results in a corresponding increase in G_0, despite the stars getting further away.

A similar evolution occurs for other stars, such as **star 4** and **star 15**, where the initial exposure takes 0.5 Myr. The latter's position is in one of the cavities blown out by the expanding H II region (the bottom right quadrant of the plots shown in Fig. 5.4), which decreases in column density. This means it does not take as long for G_0 to rise compared to star 7. It remains in the cavity with little intervening material, so there are no rapid rises or dips after the maximum value of $G_0 = 90$ is reached. **Stars 22** and **23** follow a similar pattern, with the latter positioned in the upper right quadrant cavity.

G_0 for **star 16** rises by an order of magnitude to 150 in the first 0.45 Myr, before slowly decreasing down to 110 at $t = 0.8$ Myr, then jumping up to 280 in just 0.12 Myr. This is despite the star starting off at a distance of 3 pc and only getting further away. The

delayed exposure is due to its location near the dense core in which star 1 is embedded. As that core expands and gets eroded, star 16 receives more flux; but due to the inhomogeneous distribution of gas, combined with the motion of the stars themselves, the column density increases, causing the slightly lower flux. Once this is itself dispersed, the star is more fully exposed.

This is even more the case for **star 20**, which is initially only 1.2 pc away from star 1. G_0 increases by a factor of 6 in the first Myr, reaching a maximum value of 5700.

The evolution of **star 21** is somewhat more complex, as it is located further away – starting at 7 pc and increasing to 13 pc. As the H II region expands, it pushes material in the way, so the illumination of star 21 occurs in a series of three steps up to 1.45 Myr.

Star 29 remains embedded in a dense filament (and later globule), which shields it up until 2.5 Myr, when the gas is photoevaporated away and the star becomes exposed. G_0 rises from 2 to 920 from $t = 2.45$ to 3.15 Myr – an increase of almost three orders of magnitude in the space of 0.7 Myr.

5.4.4.2 Temporary shielding and transits

The wide separation between **stars 21** and 1 (7 to 13 pc) means there is a greater chance for material to come in between: at 1.68 Myr, this causes a dip by a factor of 2 from $G_0 = 40$ to 20. This is short-lived, as it rises after another 0.1 Myr.

Star 5 is surrounded by a moving clump of gas which becomes aligned such that it blocks light from star 1. A column density snapshot is shown in Fig. 5.9. At 1.5 Myr, the flux decreases from 420 to 10, before being restored 0.85 Myr later. This happens again around 3.5 Myr, as G_0 drops from just over 400 to 7, a factor of 60 decrease. After 0.2 Myr, it then rapidly jumps up to 750 as the gas is blown away. This, combined with the narrower separation between the two stars, results in a final G_0 of 1000. **Star 10** follows a similar pattern to star 5 as it located near the same clump of gas.

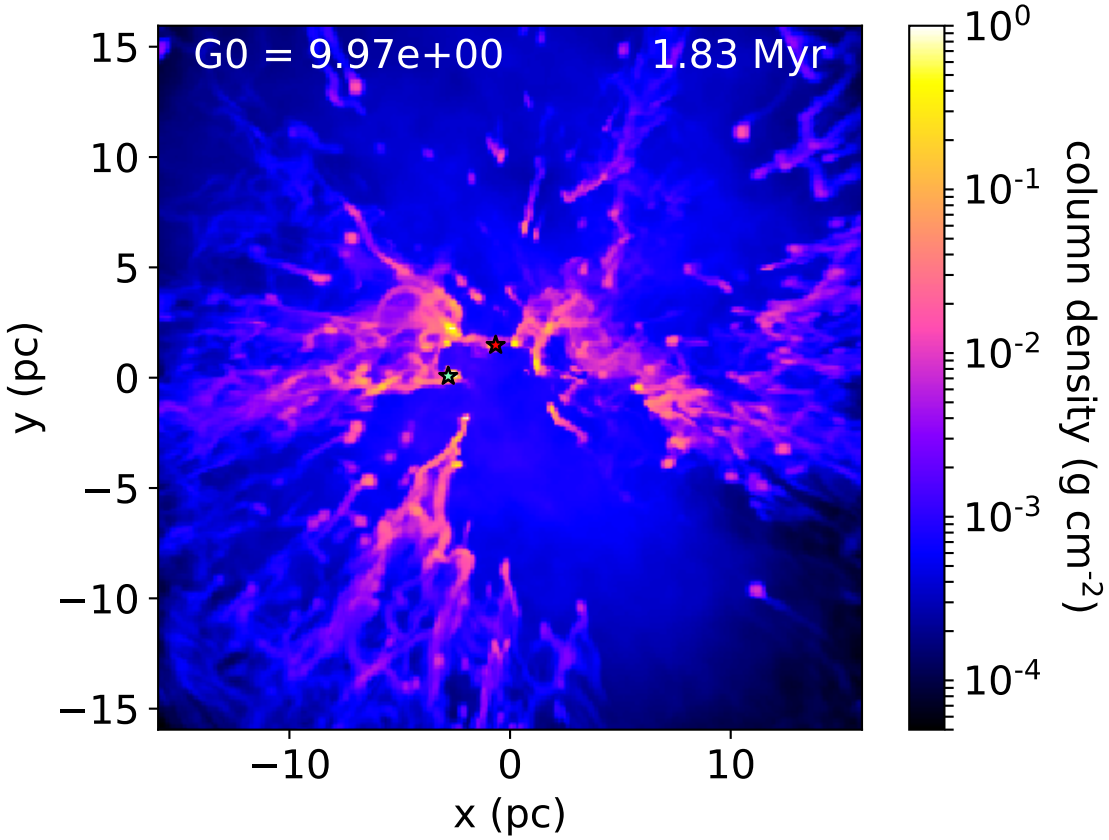

Figure 5.9: Column density snapshot showing the positions of the 34 $M_\odot$ star (red point) and star 5, a 4.98 $M_\odot$ star (green point). The annotation displays G_0 at the location of star 5 (discussed in section 5.4.4.2).

5.4.5 Implications

The models presented here have shown how G_0 evolves in time as both gas and stars move around. In the first ~ 0.5 Myr the most massive star is embedded within a core which takes time to be eroded by the expanding H II region – shells expand outwards and have holes punched through them, allowing radiation to escape into the cluster medium. This means many are stars are initially shielded from the massive star's radiation field, allowing them to evolve in relative isolation, but then become illuminated as material is dispersed. Some parcels of gas may move back in between, causing a drastic decrease in flux.

Models of protoplanetary disks, which have life times of the order of a few to 10 Myr (Haisch et al. 2001; Mamajek 2009; Winter et al. 2018), do not consider the full time-varying effect that cluster-gas interactions have on G_0. This is important, as external fields can truncate and erode the outer edges of disks by photoevaporating them. For example, Adams et al. (2004) found that within time scales of 10 Myr, disks around solar-mass stars can be severely truncated (down to radii below 15 AU) with $G_0 = 3 \times 10^4$, while stellar masses below 0.5 $M_\odot$ only require $G_0 = 3 \times 10^3$. Such fields are present in the models presented here and in chapter 4. Even small values of G_0 can be significant, as models by Facchini et al. (2016) exhibited mass loss rates of 10^{-7} $M_\odot$ yr^{-1} with $G_0 \sim 30$, provided grain growth is taken into account. In the models of Winter et al. (2018), photoevaporation always dominated over tidal truncation caused by encounters between stars. The results found in this chapter may therefore provide crucial information for how protoplanetary disks evolve.

5.5 Summary and conclusions

I have modelled a 10^4 $M_\odot$ cloud with the same surface density and stellar spectrum as in chapter 4. The same numerical methods are present in both models, allowing a comparison to be made between the two mass regimes. In summary:

- The higher mass cloud is somewhat more resistant to feedback, with 25 per cent of the initial mass remaining inside $(32.3\,\mathrm{pc})^3$ after 4.3 Myr. In the lower-mass model, almost all material is removed from the $(15.5\,\mathrm{pc})^3$ grid within 1.6 Myr.

- However, given that 75 per cent of the mass is still removed, photoionization feedback is still an effective mechanism for disrupting GMCs. Mass leaves the grid with a peak flux of $4.7 \times 10^{-3}\,\mathrm{M_\odot\,yr^{-1}}$.

- The total mass in Jeans-unstable cells approaches $1500\,\mathrm{M_\odot}$, representing a 15 per cent core formation efficiency or potential 5 per cent star formation efficiency. This order of magnitude estimate agrees with observational constraints.

- Radiation pressure has a negligible effect on all bulk grid properties, although there is a minor difference in the Jeans-unstable mass – there is $300\,\mathrm{M_\odot}$ more in the combined feedback model than the ionization-only model. Given that this measure is a very rough estimate, it is unlikely to result in a significant difference in actual star formation efficiency.

- The time-variation of G_0 around other cluster members is complex, depending on when the massive star disperses the core it is initially embedded in, and on whether any material passes in between. There can be drastic increases or decreases by orders of magnitude, lasting for durations of ~ 1 Myr.

The total run time of this model (thus far) was 4.3 Myr, about a Myr before the $34\,\mathrm{M_\odot}$ star will explode as a supernova (SN). A quarter of the gas still remains on the grid, and is unlikely to significantly disperse by the time the SN occurs, as the grid-boundary mass flux falls off over time. However, since this material is located in small, dense filaments and clumps, surrounded by large cavities of diffuse ionized gas, it is unlikely that the SN will transfer a significant proportion of its energy into the gas, whether it occurs now or in a Myr. Nonetheless, this is something that should be investigated. TORUS

does not yet include a prescription for SN feedback, so this is something I propose to implement, as discussed further in chapter 6.

Chapter 6

Conclusions

6.1 Summary and main findings

I have described the algorithms used by TORUS to model radiative transfer using Monte Carlo random sampling.

- This allows splitting the problem over many processors using MPI. I have significantly improved the way in which this is implemented by mitigiating bottlenecks, such that photons are initialised at the beginning of the radiation calculation as quickly as possible, and then propagated via MPI more efficiently.
- This has allowed tractable computations of photoionization balance and radiation pressure with multiple atomic species and dust grains, in three dimensions, at scales up to ~ 30 pc and 5 Myr.
- The microphysical detail included in these simulations make them the first of their kind, improving upon the simplified radiative transfer techniques deployed in previous studies.

I have applied this to clouds of 10^3 and 10^4 $M_\odot$, with surface density 0.01 g cm^{-2}, containing a 34 $M_\odot$ star. These conditions broadly match observations of Galactic GMCs by Solomon et al. (1987) and Heyer et al. (2009), and allow comparison with other

simulations by e.g. Dale et al. (2012) and Walch et al. (2012), who use Strömgren-volume methods to find ionization fronts, set gas temperatures without calculating the heating and cooling rates, and do not explicitly include dust. In these models, I find:

- gas is efficiently dispersed within 1.6 Myr for the 10^3 $M_\odot$ cloud, and 4.3 Myr for the 10^4 $M_\odot$ cloud; in terms of the free-fall time scale, this corresponds to 0.75 and 1.1 $\langle t_{\rm ff} \rangle$, respectively. All the mass is removed from the grid in the former case, while about 25 per cent remains in the latter case.

- The dense gas is located inside neutral clumps, roughly spherical in shape, with tails pointing away from the massive star. They move radially away due to the rocket effect, as the star-side edges are photoevaporated and eject material back towards to the star.

- The diffuse radiation field contributes to partially ionizing 'shadowed' regions, increasing the total mass that would be ionized relative to a stellar-radiation only model.

- The FUV radiation field around sink particles varies with time in a complex manner. Variations of orders of magnitude can occur over Myr time scales.

I have also produced synthetic observations of the low-mass cloud, in order to test observational diagnostics. These were computed using the ionization states and temperatures that were calculated in the RHD model itself, not through any post-processing. This includes:

- line emission such as Hα, which becomes optically thin as gas is removed from the line of sight.

- Free-free continuum emission at 20 cm has been used to infer the production rate of ionizing photons. The observational technique underestimates the actual value at all times; as gas and ionizing photons are removed from the field of view, the

estimate gets worse, even though the radio flux always traces photoionization balance accurately.

- Dust thermal emission at 450 and 850 µm is used to retrieve dust temperatures, which provides correct values in dense locations such as filaments, but not in areas of low column density or high temperature dispersion, such as the H II region cavity.

Radiation pressure is mostly negligible in the models I present here. It is expected to play a more significant role in higher density clouds and higher luminosity clusters (Fall et al. 2010). Now that the radiative transfer can be computed efficiently, the parameter space of GMCs can be explored more thoroughly, beyond the two clouds I have modelled. In the following sections, I suggest ways this can be done, including proposals to track star formation self-consistently, and to investigate the role of other feedback mechanisms.

6.2 Proposed future work

6.2.1 Cloud parameter space and sink particles

The model in chapter 4 is analogous in terms of mass to a region such as the Orion Nebula Cluster, but this is only a part of the larger Orion Molecular Cloud. These GMCs can reach masses of $10^6\,M_\odot$; in addition to the cloud mass, however, the scatter in the observed properties of GMCs (see Solomon et al. 1987; Heyer et al. 2009) necessitates an exploration of cloud radii, surface densities, and boundness as well. With such a large parameter space to explore, subgrid models are required to calculate a full suite of simulations – not all of the physical processes can be computed self-consistently.

TORUS uses sink particles to represent stars (Harries 2015; Federrath et al. 2010). This was used by Harries et al. (2017) to model the formation of a single massive star in a 0.1 pc core. However, on a cluster scale, a finer spatial resolution is required to track star formation self-consistently, and this would come with a cost of a longer simulation runtime – the smaller minimum cell size will produce smaller Courant time-steps (equation 3.4).

At large GMC scales the problem can be mitigated by making each sink particle represent an entire cluster. I propose adding a subgrid model such that once a density threshold is reached, a cluster-sink particle is formed, containing a population of stars drawn from a Chabrier (2003) IMF as it accretes material. Similar steps have been taken by e.g. Howard et al. (2014). In the MCRT step, the sink would emit radiation from a combined SED constructed from its stellar population. The 10^3 and $10^4\,M_\odot$ models could be used to inform some of these input parameters, since only a certain fraction of the radiation should escape from the cluster, and that fraction can be taken from the already calculated models. Furthermore, they provide mass fluxes which could be injected from the cluster particles into the high-mass models.

The models in chapters 4 and 5 use a uniform 256^3 grid. Including sink formation would also require adaptively refining the mesh, such that higher resolution is acquired where dense cores are collapsing, and lower resolution is used in quiescent regions. TORUS does have AMR capabilities, and indeed this was used in Harries et al. (2017). However, that calculation had a simpler requirement, as only one star was being formed, and it was fixed in place; a cluster of moving stars is a more demanding scenario. The self-gravity module in TORUS would also need improving for this level of complexity. A compromise may then have to be made in the radiative transfer in order to achieve a tractable simulation run-time. For example, the thermal balance calculation could be simplified by using the parameterisation with ionization fraction discussed in section 4.6.2.

Once star formation is enabled in the simulations, this will provide a way to compare how the star formation rate and efficiency are affected by feedback. The computed SFRs could then be compared with simulated observational diagnostics (reviewed by Kennicutt 1998), such as Hα lines, thermal dust continuum, and free-free continuum, which are already calculable in TORUS.

6.2.2 Modelling stellar winds and supernovae

The combined effects of photoionization, radiation pressure, and stellar winds will produce the condition into which SNe explode. A $34\,M_\odot$ star will undergo a SN after ~ 5 Myr, which would be less than the dispersal timescale for the high-mass GMCs proposed in section 6.2.1. This could be implemented as an injection of mass and energy from sink particles into the gas around some radius. The Schaller et al. (1992) evolutionary tracks, which sink particles in TORUS already follow, provide a mass-loss rate that can be taken to be the mass injection rate for winds. As outlined in section 1.2.4, the wind terminal velocity can be given as $\sim 1000\,\mathrm{km\,s^{-1}}$ and the gas heated to 10^6 K. For SNe, an explosion of 10^{51} erg of thermal energy can be injected similar to Rogers & Pittard (2013); alternatively some fraction could go into kinetic energy and the rest into thermal as per Dobbs (2015) or Fierlinger et al. (2016). Once a cell is heated by winds or SNe, it should be made exempt from the thermal balance routines computed from photoionization processes – instead, temperatures and ionization states (from collisional ionization) would follow pre-tabulated cooling functions and ionization fractions (from e.g. Sutherland & Dopita 1993). Once gas cools down to $\sim 10^4$ K, the cells should then be re-included in the photoionization balance calculations.

6.2.3 Photodissociation of molecules

The models presented in this thesis are comprised entirely of atomic species, but real molecular clouds have molecules in them. They will be dissociated by the FUV flux from massive stars, and this could impact star formation in the ways described in section 1.2.6. The aim is to apply this physics in 3D cluster-scale simulations to investigate its effects on star formation, in tandem with photoionization and radiation pressure. Although some work is already being done in this area (Butler et al. 2017; Peters et al. 2017) it is still a relatively unexplored problem. Furthermore, it is also necessary to characterise the interplay with dust grains, which absorb (F)UV photons, re-emitting in the infrared, thus

reducing the amount going into the gas. The treatment of dust in TORUS is accurate enough to investigate this interaction thoroughly.

6.2.4 Disk photoevaporation

The values of G_0 calculated over the course of the two simulations will be used by Tom Haworth to study the external photoevaporation of viscous disks around solar-like stars. The disk host stars will use the stellar masses of the sink particles in my simulations, with disks initially being a tenth of the stellar mass with radius 200 AU. These models will feed in the full time-varying fluxes which arose from evolving sources of FUV opacity between each disk and the rest of the cluster. This essentially can be thought of as zooming in to the region inside each sink particle, and following its AU-scale evolution. This novel approach will build up a realistic picture of disk dispersal within a stellar cluster containing massive stars, such as the Orion Nebula.

Bibliography

Acreman D. M., Harries T. J., Rundle D. A., 2010, MNRAS, 403, 1143

Adams F. C., Hollenbach D., Laughlin G., Gorti U., 2004, ApJ, 611, 360

Agertz O., Kravtsov A. V., Leitner S. N., Gnedin N. Y., 2013, ApJ, 770, 25

Ali A., Harries T. J., Douglas T. A., 2018, MNRAS, 477, 5422

Allison R. J., Goodwin S. P., Parker R. J., de Grijs R., Portegies Zwart S. F., Kouwenhoven M. B. N., 2009, ApJ, 700, L99

Altenhoff W. J., Mezger P. G., Wendker H., Westerhout G., 1960, Veröff. Sternwärte, Bonn, 59, 48

Alves J., Lombardi M., Lada C. J., 2007, A&A, 462, L17

Anderson K. R., Adams F. C., Calvet N., 2013, ApJ, 774, 9

André P., et al., 2010, A&A, 518, L102

Arthur S. J., Henney W. J., Mellema G., de Colle F., Vázquez-Semadeni E., 2011, MNRAS, 414, 1747

Baczynski C., Glover S. C. O., Klessen R. S., 2015, MNRAS, 454, 380

Bastian N., Covey K. R., Meyer M. R., 2010, ARA&A, 48, 339

Bate M. R., 2009, MNRAS, 392, 1363

Bate M. R., 2012, MNRAS, 419, 3115

Bate M. R., 2014, MNRAS, 442, 285

Bate M. R., Bonnell I. A., Bromm V., 2002, MNRAS, 332, L65

Bate M. R., Bonnell I. A., Bromm V., 2003, MNRAS, 339, 577

Benz W., 1990, in Buchler J. R., ed., Numerical Modelling of Nonlinear Stellar Pulsations

Problems and Prospects. p. 269

Bertoldi F., 1989, ApJ, 346, 735

Bertoldi F., McKee C. F., 1990, ApJ, 354, 529

Bisbas T. G., Wünsch R., Whitworth A. P., Hubber D. A., Walch S., 2011, ApJ, 736, 142

Bisbas T. G., Haworth T. J., Barlow M. J., Viti S., Harries T. J., Bell T., Yates J. A., 2015, MNRAS, 454, 2828

Bodenheimer P., Tenorio-Tagle G., Yorke H. W., 1979, ApJ, 233, 85

Bonnell I. A., Bate M. R., Clarke C. J., Pringle J. E., 1997, MNRAS, 285, 201

Bonnell I. A., Bate M. R., Clarke C. J., Pringle J. E., 2001, MNRAS, 323, 785

Bonnell I. A., Vine S. G., Bate M. R., 2004, MNRAS, 349, 735

Bruderer S., van Dishoeck E. F., Doty S. D., Herczeg G. J., 2012, A&A, 541, A91

Bryan G. L., et al., 2014, ApJS, 211, 19

Butler M. J., Tan J. C., Teyssier R., Rosdahl J., Van Loo S., Nickerson S., 2017, ApJ, 841, 82

Castor J. I., Abbott D. C., Klein R. I., 1975a, ApJ, 195, 157

Castor J., McCray R., Weaver R., 1975b, ApJ, 200, L107

Chabrier G., 2003, PASP, 115, 763

Chakraborty A., Anandarao B. G., 1997, AJ, 114, 1576

Chandrasekhar S., 1960, Radiative Transfer. Dover Books on Intermediate and Advanced Mathematics, Dover Publications

Clarke D. A., 1996, ApJ, 457, 291

Clarke D. A., 2010, ApJS, 187, 119

Colín P., Vázquez-Semadeni E., Gómez G. C., 2013, MNRAS, 435, 1701

Dale J. E., 2015, New A Rev., 68, 1

Dale J. E., 2017, MNRAS, 467, 1067

Dale J. E., Bonnell I. A., 2008, MNRAS, 391, 2

Dale J. E., Bonnell I., 2011, MNRAS, 414, 321

Dale J. E., Bonnell I. A., 2012, MNRAS, 422, 1352

Dale J. E., Bonnell I. A., Clarke C. J., Bate M. R., 2005, MNRAS, 358, 291

Dale J. E., Bonnell I. A., Whitworth A. P., 2007a, MNRAS, 375, 1291

Dale J. E., Clark P. C., Bonnell I. A., 2007b, MNRAS, 377, 535

Dale J. E., Ercolano B., Clarke C. J., 2007c, MNRAS, 382, 1759

Dale J. E., Ercolano B., Bonnell I. A., 2012, MNRAS, 424, 377

Dale J. E., Ercolano B., Bonnell I. A., 2013a, MNRAS, 430, 234

Dale J. E., Ngoumou J., Ercolano B., Bonnell I. A., 2013b, MNRAS, 436, 3430

Dale J. E., Ngoumou J., Ercolano B., Bonnell I. A., 2014, MNRAS, 442, 694

Dobbs C. L., 2015, MNRAS, 447, 3390

Dobbs C. L., Burkert A., Pringle J. E., 2011, MNRAS, 417, 1318

Draine B. T., 1978, ApJS, 36, 595

Draine B. T., 2011, ApJ, 732, 100

Draine B. T., Lee H. M., 1984, ApJ, 285, 89

Dullemond C. P., 2012, Radiative Transfer in Astrophysics, lecture notes. Universität Heidelberg

Dullemond C. P., Dominik C., 2004, A&A, 417, 159

Dullemond C. P., Wang H. H., 2009, Numerical Fluid Dynamics, lecture notes. Universität Heidelberg

Dyson J. E., Williams D. A., 1980, Physics of the Interstellar Medium. Manchester University Press

Elmegreen B. G., Lada C. J., 1977, ApJ, 214, 725

Elmegreen B. G., Kimura T., Tosa M., 1995, ApJ, 451, 675

Ercolano B., Barlow M. J., Storey P. J., Liu X.-W., 2003, MNRAS, 340, 1136

Facchini S., Clarke C. J., Bisbas T. G., 2016, MNRAS, 457, 3593

Fall S. M., Krumholz M. R., Matzner C. D., 2010, ApJ, 710, L142

Federrath C., Banerjee R., Clark P. C., Klessen R. S., 2010, ApJ, 713, 269

Ferland G., 1995, in Williams R., Livio M., eds, The Analysis of Emission Lines: A Meeting in Honor of the 70th Birthdays of D. E. Osterbrock and M. J. Seaton. p. 83

Ferland G. J., et al., 2013, Rev. Mexicana Astron. Astrofis., 49, 137

Fierlinger K. M., Burkert A., Diehl R., Dobbs C., Hartmann D. H., Krause M., Ntormousi E., Voss R., 2012, in Capuzzo-Dolcetta R., Limongi M., Tornambè A., eds, Astronomical Society of the Pacific Conference Series Vol. 453, Advances in Computational Astrophysics: Methods, Tools, and Outcome. p. 25

Fierlinger K. M., Burkert A., Ntormousi E., Fierlinger P., Schartmann M., Ballone A., Krause M. G. H., Diehl R., 2016, MNRAS, 456, 710

Figueira M., et al., 2017, A&A, 600, A93

Forgan D., Rice K., 2010, MNRAS, 406, 2549

Franco J., Tenorio-Tagle G., Bodenheimer P., 1990, ApJ, 349, 126

Fryxell B., et al., 2000, ApJS, 131, 273

Gatto A., et al., 2017, MNRAS, 466, 1903

Geen S., Hennebelle P., Tremblin P., Rosdahl J., 2015, MNRAS, 454, 4484

Geen S., Hennebelle P., Tremblin P., Rosdahl J., 2016, MNRAS, 463, 3129

Geen S., Soler J. D., Hennebelle P., 2017, MNRAS, 471, 4844

Girichidis P., et al., 2016, MNRAS, 456, 3432

Glover S. C. O., Federrath C., Mac Low M.-M., Klessen R. S., 2010, MNRAS, 404, 2

Gritschneder M., Naab T., Walch S., Burkert A., Heitsch F., 2009, ApJ, 694, L26

Habing H. J., 1968, Bull. Astron. Inst. Netherlands, 19, 421

Haikala L. K., Gahm G. F., Grenman T., Mäkelä M. M., Persson C. M., 2017, A&A, 602, A61

Haisch Jr. K. E., Lada E. A., Lada C. J., 2001, ApJ, 553, L153

Harries T. J., 2000, MNRAS, 315, 722

Harries T. J., 2015, MNRAS, 448, 3156

Harries T. J., Howarth I. D., 1997, A&AS, 121

Harries T. J., Monnier J. D., Symington N. H., Kurosawa R., 2004, MNRAS, 350, 565

Harries T. J., Douglas T. A., Ali A., 2017, MNRAS, 471, 4111

Haworth T. J., Harries T. J., 2012, MNRAS, 420, 562

Haworth T. J., Harries T. J., Acreman D. M., 2012, MNRAS, 426, 203

Haworth T. J., Harries T. J., Acreman D. M., Bisbas T. G., 2015, MNRAS, 453, 2277

Haworth T. J., Boubert D., Facchini S., Bisbas T. G., Clarke C. J., 2016, MNRAS, 463, 3616

Henney W. J., Arthur S. J., García-Díaz M. T., 2005, ApJ, 627, 813

Henney W. J., Arthur S. J., de Colle F., Mellema G., 2009, MNRAS, 398, 157

Heyer M., Krawczyk C., Duval J., Jackson J. M., 2009, ApJ, 699, 1092

Hillenbrand L. A., Hartmann L. W., 1998, ApJ, 492, 540

Hollenbach D., McKee C. F., 1979, ApJS, 41, 555

Hopkins P. F., 2015, MNRAS, 450, 53

Hopkins P. F., Quataert E., Murray N., 2012, MNRAS, 421, 3488

Hosokawa T., Inutsuka S.-i., 2005, ApJ, 623, 917

Hosokawa T., Inutsuka S.-i., 2006a, ApJ, 646, 240

Hosokawa T., Inutsuka S.-i., 2006b, ApJ, 648, L131

Howard C. S., Pudritz R. E., Harris W. E., 2014, MNRAS, 438, 1305

Howard C. S., Pudritz R. E., Harris W. E., 2016, MNRAS, 461, 2953

Howarth I., 2010, Astrophysical Processes:Nebulae to Stars, lecture notes. University College London

Hubber D. A., Batty C. P., McLeod A., Whitworth A. P., 2011, A&A, 529, A27

Hubber D. A., Ercolano B., Dale J., 2016, MNRAS, 456, 756

Iffrig O., Hennebelle P., 2015, A&A, 576, A95

Immer K., Cyganowski C., Reid M. J., Menten K. M., 2014, A&A, 563, A39

Inoue A. K., 2002, ApJ, 570, 688

Jeans J. H., 1902, Philosophical Transactions of the Royal Society of London Series A, 199, 1

Johnstone D., Hollenbach D., Bally J., 1998, ApJ, 499, 758

Kahn F. D., 1954, Bull. Astron. Inst. Netherlands, 12, 187

Kahn F. D., 1974, A&A, 37, 149

Katz N., Weinberg D. H., Hernquist L., 1996, ApJS, 105, 19

Kennicutt Jr. R. C., 1998, ARA&A, 36, 189

Kessel-Deynet O., Burkert A., 2003, MNRAS, 338, 545

Kim J.-h., Krumholz M. R., Wise J. H., Turk M. J., Goldbaum N. J., Abel T., 2013, ApJ, 775, 109

Kim J. S., Clarke C. J., Fang M., Facchini S., 2016, ApJ, 826, L15

Kim W.-J., Wyrowski F., Urquhart J. S., Menten K. M., Csengeri T., 2017a, A&A, 602, A37

Kim J.-G., Kim W.-T., Ostriker E. C., Skinner M. A., 2017b, ApJ, 851, 93

Kim J.-G., Kim W.-T., Ostriker E. C., 2018, ApJ, 859, 68

Klassen M., Pudritz R. E., Kuiper R., Peters T., Banerjee R., 2016, ApJ, 823, 28

Klein R. I., 1999, Journal of Computational and Applied Mathematics, 109, 123

Klessen R. S., Glover S. C. O., 2016, Physical Processes in the Interstellar Medium. Star Formation in Galaxy Evolution: Connecting Numerical Models to Reality, Saas-Fee Advanced Course Vol. 43, Springer-Verlag Berlin Heidelberg, doi:10.1007/978-3-662-47890-5_2

Klessen R. S., Burkert A., Bate M. R., 1998, ApJ, 501, L205

Koepferl C. M., Robitaille T. P., 2017, ApJ, 849, 3

Koepferl C. M., Robitaille T. P., Dale J. E., Biscani F., 2017a, ApJS, 233, 1

Koepferl C. M., Robitaille T. P., Dale J. E., 2017b, ApJ, 849, 1

Koepferl C. M., Robitaille T. P., Dale J. E., 2017c, ApJ, 849, 2

Könyves V., et al., 2010, A&A, 518, L106

Krause M., Fierlinger K., Diehl R., Burkert A., Voss R., Ziegler U., 2013, A&A, 550, A49

Kroupa P., Tout C. A., Gilmore G., 1993, MNRAS, 262, 545

Krumholz M. R., 2006, ApJ, 641, L45

Krumholz M. R., 2015, in Vink J. S., ed., Astrophysics and Space Science Library Vol. 412, Very Massive Stars in the Local Universe. p. 43, doi:10.1007/978-3-319-09596-7_3

Krumholz M. R., Matzner C. D., 2009, ApJ, 703, 1352

Krumholz M. R., Thompson T. A., 2012, ApJ, 760, 155

Krumholz M. R., Klein R. I., McKee C. F., 2007, ApJ, 665, 478

Krumholz M. R., Klein R. I., McKee C. F., Offner S. S. R., Cunningham A. J., 2009, Science, 323, 754

Krumholz M. R., Klein R. I., McKee C. F., 2011, ApJ, 740, 74

Krumholz M. R., Klein R. I., McKee C. F., 2012, ApJ, 754, 71

Kuiper G. P., 1938, ApJ, 88, 472

Kuiper R., Klahr H., Dullemond C., Kley W., Henning T., 2010a, A&A, 511, A81

Kuiper R., Klahr H., Beuther H., Henning T., 2010b, ApJ, 722, 1556

Kuiper R., Klahr H., Beuther H., Henning T., 2011, ApJ, 732, 20

Kurosawa R., Harries T. J., Bate M. R., Symington N. H., 2004, MNRAS, 351, 1134

Kurucz R. L., 1991, in Crivellari L., Hubeny I., Hummer D. G., eds, NATO Advanced Science Institutes (ASI) Series C Vol. 341, NATO Advanced Science Institutes (ASI) Series C. p. 441

Lada C. J., Lada E. A., 2003, ARA&A, 41, 57

Lada C. J., Margulis M., Dearborn D., 1984, ApJ, 285, 141

Lanz T., Hubeny I., 2003, ApJS, 146, 417

Larson R. B., 1981, MNRAS, 194, 809

Larson R. B., Starrfield S., 1971, A&A, 13, 190

Ledoux P., 1941, ApJ, 94, 537

Lefloch B., Lazareff B., Castets A., 1997, A&A, 324, 249

Lomax O., Whitworth A. P., 2016, MNRAS, 461, 3542

Lopez L. A., Krumholz M. R., Bolatto A. D., Prochaska J. X., Ramirez-Ruiz E., 2011, ApJ, 731, 91

Lopez L. A., Krumholz M. R., Bolatto A. D., Prochaska J. X., Ramirez-Ruiz E., Castro D., 2014, ApJ, 795, 121

Lucy L. B., 1999, A&A, 344, 282

Mamajek E. E., 2009, in Usuda T., Tamura M., Ishii M., eds, American Institute of Physics

Conference Series Vol. 1158, American Institute of Physics Conference Series. pp 3–10 (arXiv:0906.5011), doi:10.1063/1.3215910

Mathews W. G., 1967, ApJ, 147, 965

Mathis J. S., Rumpl W., Nordsieck K. H., 1977, ApJ, 217, 425

Matzner C. D., 2002, ApJ, 566, 302

McKee C. F., Tan J. C., 2003, ApJ, 585, 850

McMillan S. L. W., Vesperini E., Portegies Zwart S. F., 2007, ApJ, 655, L45

Medina S.-N. X., Arthur S. J., Henney W. J., Mellema G., Gazol A., 2014, MNRAS, 445, 1797

Mellema G., Raga A. C., Canto J., Lundqvist P., Balick B., Steffen W., Noriega-Crespo A., 1998, A&A, 331, 335

Mellema G., Iliev I. T., Alvarez M. A., Shapiro P. R., 2006a, New A, 11, 374

Mellema G., Arthur S. J., Henney W. J., Iliev I. T., Shapiro P. R., 2006b, ApJ, 647, 397

Meyer D. M.-A., Kuiper R., Kley W., Johnston K. G., Vorobyov E., 2018, MNRAS, 473, 3615

Mezger P. G., Henderson A. P., 1967, ApJ, 147, 471

Mihalas D., Weibel-Mihalas B., 1999, Foundations of Radiation Hydrodynamics. Dover Books on Physics, Dover

Moeckel N., Bonnell I. A., 2009, MNRAS, 400, 657

Monaghan J. J., 1992, ARA&A, 30, 543

Motte F., Andre P., Neri R., 1998, A&A, 336, 150

Ngoumou J., Hubber D., Dale J. E., Burkert A., 2015, ApJ, 798, 32

Nutter D., Ward-Thompson D., 2007, MNRAS, 374, 1413

O'Dell C. R., 2000, AJ, 119, 2311

O'Dell C. R., Henney W. J., Abel N. P., Ferland G. J., Arthur S. J., 2009, AJ, 137, 367

O'Dell C. R., Ferland G. J., Peimbert M., 2017, MNRAS, 464, 4835

O'dell C. R., 2001, ARA&A, 39, 99

O'dell C. R., Wen Z., Hu X., 1993, ApJ, 410, 696

Offner S. S. R., Klein R. I., McKee C. F., Krumholz M. R., 2009, ApJ, 703, 131

Offner S. S. R., Clark P. C., Hennebelle P., Bastian N., Bate M. R., Hopkins P. F., Moraux E., Whitworth A. P., 2014, Protostars and Planets VI, pp 53–75

Osterbrock D., Ferland G., 2006, Astrophysics of Gaseous Nebulae and Active Galactic Nuclei, 2nd edn. University Science Books

Pang X., Grebel E. K., Allison R. J., Goodwin S. P., Altmann M., Harbeck D., Moffat A. F. J., Drissen L., 2013, ApJ, 764, 73

Parker R. J., Dale J. E., 2017, MNRAS, 470, 390

Peimbert M., Peimbert A., Delgado-Inglada G., 2017, PASP, 129, 082001

Pellegrini E. W., Baldwin J. A., Ferland G. J., 2011, ApJ, 738, 34

Pelupessy F. I., Portegies Zwart S., 2012, MNRAS, 420, 1503

Peters T., Banerjee R., Klessen R. S., Mac Low M.-M., Galván-Madrid R., Keto E. R., 2010, ApJ, 711, 1017

Peters T., et al., 2017, MNRAS, 466, 3293

Pinte C., Ménard F., Duchêne G., Bastien P., 2006, A&A, 459, 797

Price D. J., et al., 2017, preprint, (arXiv:1702.03930)

Raskutti S., Ostriker E. C., Skinner M. A., 2016, ApJ, 829, 130

Reid M. A., Wilson C. D., 2005, ApJ, 625, 891

Rey-Raposo R., Dobbs C., Duarte-Cabral A., 2015, MNRAS, 446, L46

Rey-Raposo R., Dobbs C., Agertz O., Alig C., 2017, MNRAS, 464, 3536

Reynolds R. J., 1984, ApJ, 282, 191

Richling S., Yorke H. W., 2000, ApJ, 539, 258

Robitaille T. P., 2011, A&A, 536, A79

Roe P. L., 1986, Annual Review of Fluid Mechanics, 18, 337

Rogers H., Pittard J. M., 2013, MNRAS, 431, 1337

Rosdahl J., Blaizot J., Aubert D., Stranex T., Teyssier R., 2013, MNRAS, 436, 2188

Rosen A. L., Krumholz M. R., McKee C. F., Klein R. I., 2016, MNRAS, 463, 2553

Rosen A. L., Krumholz M. R., Oishi J. S., Lee A. T., Klein R. I., 2017, Journal of

Computational Physics, 330, 924

Rubin R. H., 1968, ApJ, 154, 391

Rumble D., et al., 2015, MNRAS, 448, 1551

Rybicki G. B., Lightman A. P., 1979, Radiative Processes in Astrophysics. Wiley

Sadavoy S. I., et al., 2012, A&A, 540, A10

Salpeter E. E., 1955, ApJ, 121, 161

Schaller G., Schaerer D., Meynet G., Maeder A., 1992, A&AS, 96, 269

Schwarzschild M., Härm R., 1959, ApJ, 129, 637

Seifried D., et al., 2017, MNRAS, 472, 4797

Shu F. H., Adams F. C., Lizano S., 1987, ARA&A, 25, 23

Skinner M. A., Ostriker E. C., 2015, ApJ, 809, 187

Smith R. J., Clark P. C., Bonnell I. A., 2009, MNRAS, 396, 830

Solomon P. M., Rivolo A. R., Barrett J., Yahil A., 1987, ApJ, 319, 730

Spitzer L., 1978, Physical Processes in the Interstellar Medium. Wiley-Interscience, New York, doi:10.1002/9783527617722

Springel V., 2010, MNRAS, 401, 791

Springel V., Yoshida N., White S. D. M., 2001, New A, 6, 79

Springel V., Di Matteo T., Hernquist L., 2005, MNRAS, 361, 776

Stecher T. P., Williams D. A., 1967, ApJ, 149, L29

Stone J. M., Gardiner T. A., Teuben P., Hawley J. F., Simon J. B., 2008, ApJS, 178, 137

Strömgren B., 1939, ApJ, 89, 526

Sutherland R. S., Dopita M. A., 1993, ApJS, 88, 253

Symington N. H., Harries T. J., Kurosawa R., 2005, MNRAS, 356, 1489

Tan J. C., Beltran M. T., Caselli P., Fontani F., Fuente A., Krumholz M. R., McKee C. F., Stolte A., 2014, Protostars and Planets VI, pp 149–172

Tenorio-Tagle G., 1979, A&A, 71, 59

Teyssier R., 2002, A&A, 385, 337

Traficante A., et al., 2018, MNRAS, 477, 2220

Tremblin P., et al., 2013, A&A, 560, A19

Truelove J. K., Klein R. I., McKee C. F., Holliman II J. H., Howell L. H., Greenough J. A., 1997, ApJ, 489, L179

Vandenbroucke B., Wood K., 2018, Astronomy and Computing, 23, 40

Walch S., Naab T., 2015, MNRAS, 451, 2757

Walch S. K., Whitworth A. P., Bisbas T., Wünsch R., Hubber D., 2012, MNRAS, 427, 625

Walch S., Whitworth A. P., Bisbas T. G., Wünsch R., Hubber D. A., 2013, MNRAS, 435, 917

Walch S., et al., 2015, MNRAS, 454, 238

Weaver R., McCray R., Castor J., Shapiro P., Moore R., 1977, ApJ, 218, 377

Whitworth A., 1979, MNRAS, 186, 59

Whitworth A. P., Bhattal A. S., Chapman S. J., Disney M. J., Turner J. A., 1994, A&A, 290, 421

Williams R. J. R., Bisbas T. G., Haworth T. J., Mackey J., 2018, MNRAS, 479, 2016

Winter A. J., Clarke C. J., Rosotti G., Ih J., Facchini S., Haworth T. J., 2018, MNRAS, 478, 2700

Wise J. H., Abel T., Turk M. J., Norman M. L., Smith B. D., 2012, MNRAS, 427, 311

Wolfire M. G., Cassinelli J. P., 1987, ApJ, 319, 850

Wood K., 2016, Monte Carlo Radiation Transport Techniques, lecture notes. University of St. Andrews

Wood K., Mathis J. S., Ercolano B., 2004, MNRAS, 348, 1337

Wünsch R., Tenorio-Tagle G., Palouš J., Silich S., 2008, ApJ, 683, 683

Yorke H. W., Sonnhalter C., 2002, ApJ, 569, 846

Yorke H. W., Tenorio-Tagle G., Bodenheimer P., 1983, A&A, 127, 313

Yorke H. W., Tenorio-Tagle G., Bodenheimer P., Rozyczka M., 1989, A&A, 216, 207

Young A. K., Bate M. R., Mowat C. F., Hatchell J., Harries T. J., 2018, MNRAS, 474, 800

Yusef-Zadeh F., Morris M., White R. L., 1984, ApJ, 278, 186

Zinnecker H., 1982, Annals of the New York Academy of Sciences, 395, 226

Zinnecker H., Yorke H. W., 2007, ARA&A, 45, 481

de Grijs R., Gilmore G. F., Johnson R. A., Mackey A. D., 2002, MNRAS, 331, 245

von Neumann J., Richtmyer R. D., 1950, Journal of Applied Physics, 21, 232